The core-halo structure in the fuzzy dark matter model

(ファジーダークマターモデルにおけるコアーハロー構造)

Hei Yin Jowett Chan

Ph.D Thesis

Supervisor:

Prof. Masashi Chiba
Astronomical Institute
Tohoku University

Acknowledgements

First and foremost, I need to thank Prof. Masashi Chiba, who has been my supervisor for 5 years. He provided me a lot of freedom to conduct my research, guided me through academic and non-academic struggles, and introduced me to other important researchers, such as Hayashi Kohei, who shared his observational knowledge with me. The completion of this research will not be possible without any of the above.

I also need to thank Elisa Ferreira, who inspired me to study the Ultralight Dark Matter model and, despite the large time difference, discussed the project with me through countless valuable online meeting. She also introduced me Simon May, another important collaborator of mine who helped me overcome the numerical difficulties. The simulation code will not be able to complete without both of them.

I must thank Okamoto san, the secretary, and the IGPAS Office, who helped me complete countless exhausting administrative work in Japan for me. I would like to thank the rebellious international staff member Jose and students Klod, Chang, Dafa, Janek, Smaranika, Mao, Ronaldo, for the lively discussions during lunchtime, evening gatherings, and coffee breaks.

I would like to thank my family, most importantly, my wife Ting who gave me a life outside of work. I want to thank my son Shu for crying endlessly at night so I could truly appreciate the silence in the student office.

I would like to thank Hsi-Yu Schive for providing the data from his simulations. This work was supported in part by the Japanese Government MEXT Scholarship. Numerical computations were (in part) carried out on Cray XC50 at the Center for Computational Astrophysics, National Astronomical Observatory of Japan.

Contents

Abstract

The nature of dark matter is still mostly unknown to us, which poses problems not only to astrophysics, and cosmology but also to the particle physics. To address the issues of dark matter, such as the wide range of viable dark matter particle masses and the small scale problem in the observable local Universe, this thesis focuses on a particular dark matter model, the Fuzzy Dark Matter (FDM), which assumes a particle mass $mc^2 \geq 10^{-22}$ eV.

For such low mass, we expect the model to behave as a wave, instead of particle like the traditional Cold Dark Matter model, which introduces rich wave phenomenology on an astrophysical scale. The non-linear evolution of the FDM model follows the coupled Schrödinger-Poisson equation and one of the consequences is the formation of a core within each halo which is closely related to the core-cusp problem and diversity problem. However, previous simulations by different groups have already shown disagreements in the core mass-halo mass relation. Since the relation is always adopted for observational tests against dwarf galaxies, the uncertainty in the relation automatically translates to the uncertainty of all those constraints made on the FDM particle mass by dwarf galaxies, especially for Jeans analysis.

To further our understanding of the relation between core mass and halo mass, we developed a cosmological FDM simulation code by solving the Schrödinger-Poisson system with the pseudo-spectral method and performed simulations with various setups. We obtained a large population of haloes, where each of them is indeed a core-halo structure. We found that there exists a sizable scatter in the core-halo mass relation, which can explain the disagreement between different simulation groups. A one-to-one relation between the core and halo mass is always assumed, but in fact, the simulation data suggest that a certain halo mass can coexist with a core of a different mass. We will in the end shortly discuss how the diversity in the core-halo structure could solve the diversity problem and further suggestions for improving the numerical simulation of the FDM model.

Chapter 1

The big picture

The success of the Lambda Cold Dark Matter (ΛCDM) model in explaining the temperature fluctuation of the Cosmic Microwave Background and the flat galactic rotation curve is an indisputable fact. Meanwhile, the cosmological N-body simulation of the ΛCDM model matured, and the community can now achieve higher mass resolution and larger box sizes (Vogelsberger et al., 2020). The large volume of published data further allows us to test the ΛCDM model against non-linear structure in the observable Universe. Nevertheless, the ΛCDM model is a scientific theory, so it is a falsifiable theory. The Missing Satellite problem and the core-cusp problem, which is now transitioned into the diversity problem of the dwarf galaxies, are solid challenges attempting to falsify the ΛCDM model. Since these small-scale problems of the ΛCDM model arise on the galactic scale, one of the proposed solutions is to consider the effect of baryonic feedbacks (Bullock & Boylan-Kolchin, 2017), which, at the same time, introduces complications due to the incomplete knowledge of the galaxy formation theory. Moreover, the ΛCDM with the baryonic feedback model is also a falsifiable theory. For instance, the Ultrafaint dwarf galaxies (UFDs), which are dark matter dominated galaxies with negligible baryonic mass, are the best laboratory to test the ΛCDM model. The above strategy, making use of the local Universe as a laboratory for dark matter research, is often described as the near-field cosmology.

On the other side, the small-scale challenges could also be alleviated by alternative dark matter models, such as Warm Dark Matter (WDM), Self-Interacting Dark Matter (SIDM), Fuzzy Dark Matter, or Modified gravity theory. They are all as equally falsifiable as CDM and can recover the large scale structure of the CDM model, but are overshadowed by the partial success of the CDM model. In comparison to CDM, there are less research effort being invested in studying the structure formation of alternative models, due to the additional numerical difficulties of their own. We will start with a review of the evidence and theory of CDM, then present the big picture, a macroscopic view of the current issues and the status of Dark Matter can be summarized into three main points:

- the disagreements between the ΛCDM model and observations in the local Universe
- the huge range of viable dark matter candidates in particle mass
- the numerical difficulties of simulating alternative dark matter model

1.1 Evidence for Cold Dark Matter

The very first evidence for Dark Matter was proposed by Zwicky in 1933, who studied the kinematics of Coma cluster and concluded that the total mass is ~ 400 times larger than the mass of the baryonic luminous component. One of the strongest pieces of evidence now is the flat rotation curves of spiral galaxies (Persic et al., 1996). By assuming the stars in the disk plane are on circular orbits, we can estimate the rotational velocity of the stars from the center of the galaxy simply as

$$V_{\rm rot}(R) = \sqrt{\frac{GM(R)}{R}} \tag{1.1}$$

As the luminous disks fade away gradually from center to edge of the galaxy, the stellar density decreases, so the rotation curve is expected to decrease at the outskirt of the disk. Observationally, it is however confirmed that the rotation curves do not decrease, but instead stay constant, or flat, far beyond the visible disk. Since the rotational curve is a direct measure of the total enclosed mass content within the radii, the flat rotation curves imply there is much more mass in the galaxy than the visible component. As a result, an invisible component was proposed to be responsible for the flat curve, which is now referred to as Dark Matter.

The standard cosmological model today is the Λ-Cold Dark Matter (ΛCDM), which assumes dark matter with the following properties.

1.1.1 Coldness

The Large-Scale Structure (LSS) of the observable Universe is a direct consequence of the coldness of the dark matter. The LSS is a tracer of the underlying density distribution of dark matter in the Universe, which depends on the initial condition and the time evolution of the density perturbation. If the initial density of a region is slightly higher than the mean, it will attract the surrounding matter more strongly than the average. In the end, these regions become overdense and grow exponentially to be even more overdense. These regions are referred to as the sheet, filament, or cluster. In contrast, the underdense regions will become more underdense, because the matter moves away from it. This region is referred to as the void. Fig.1.1 shows a snapshot from a cosmological N-body simulation to demonstrate the structure formation of cold dark matter.

These gravitational process, which is called gravitational instability, amplifies the density perturbation and acts as a fundamental role in the theory of structure formation. In theory, the gravitational structure are separated into two regimes: the linear ($\delta < 1$) and non-linear regime ($\delta > 1$), where $\delta = (\rho - \bar{\rho})/\bar{\rho}$ is called the density contrast. The early Universe has density perturbation that is still in the linear regime. The evolution of the dark matter density distribution in this regime can be predicted by the linear perturbation theory. In practice, the dark matter component is coupled with the other matter component gravitationally, so we need to solve a system of Einstein-Boltzmann equations, in order to predict the evolution of the dark matter perturbation in the linear regime. Based on an initial condition determined by inflation theory, we often quantified the perturbation statis-

tically through the power spectrum $P(k)$, so the theory predicts the time evolution of the linear dark matter power spectrum.

Now the coldness plays an important role in shaping the linear power spectrum. In the early Universe, every particle species are in thermal equilibrium, or a hot and dense bath in the Universe. Dark matter, same as other particles, is expected to decouple at a certain redshift, and are produced. If the Dark Matter particle mass is large enough, they are expected to be non-relativistic after being produced. For example, the WIMP particle has a particle mass of $\sim$ GeV are thermally produced to be non-relativistic. We called these particles thermal relics, in particular, cold relics for WIMP. However, if relativistic particles are produced, those hot, or warm relics can erase density perturbation by the free streaming effect, leading to the suppression in the power spectrum, and producing less structure in the Universe. Therefore, the coldness of the dark matter can be tested against the structure formation, or the LSS, in the observable Universe. For example, Tegmark et al. (2004) collected $\sim 200,000$ galaxies redshifts from the Sloan Digital Sky Survey (SDSS), and measured the observed three-dimensional power spectrum. They found that the linear matter power spectrum predicted by CDM matches well the observed. By combining it with other measurements on other scales made by CMB, weak lensing and Lyman-α forrest, we can probe the power spectrum up to $k \sim 1$ h/kpc. As we will see later, observables on a scale below $k \sim 1$ h/kpc are considered linear observables. The match between linear theory and observable is then considered as the large-scale success of the ΛCDM model.

1.1.2 Collisionlessness

The additional matter inferred by the flat rotation curve emphasizes that the matter is not detected by telescopes at any wavelength. The invisibility, or in other words, its very weak interaction with the electromagnetic force, is the reason for calling it the Dark Matter. Although it may not interact with photons, there are questions regarding if it interacts with other baryons through elastic or inelastic collisions. To answer such a question, we must look into dense regions where the collision rate between the particles is expected to be high, but at the same time, those dense regions are in the non-linear regime. Galaxy clusters are very massive gravitationally bound objects with mass $\sim 10^{14} - 10^{15}\ M_{\odot}$, which contain hot gas emitting a significant amount of X-ray that can be detected by X-ray telescopes. In fact, the collision of two galaxy clusters, although it is rare, provides us with an important probe of the collision rate between dark matter particles and baryons. Clowe et al. (2006) presented an X-ray image of a colliding galaxy cluster, 1E 0657-558, or namely the Bullet Cluster, and measured the weak-lensing signals by it. The X-ray emission represented the distribution of hot baryonic plasma, whereas the weak lensing observation could infer the gravitational potential of the Bullet Cluster. Their results showed an offset between the center of a plasma cloud and the potential. The segregation again suggested that galaxies are not only composed of the luminous component but the dark component. More importantly, in contrast to the plasma which can be slowed by collisional effects such as ram pressure, the offset suggested that dark matter are passing by each other as if collisionless particles.

More colliding galaxy clusters are now observed, such as Abell 2744, DLSCL J0916.2+2951, and MACS J0025.4-1222, where all confirm the "collisionless" property of dark matter. If we relax the collisionless condition, these systems nowadays have been used to test the upper

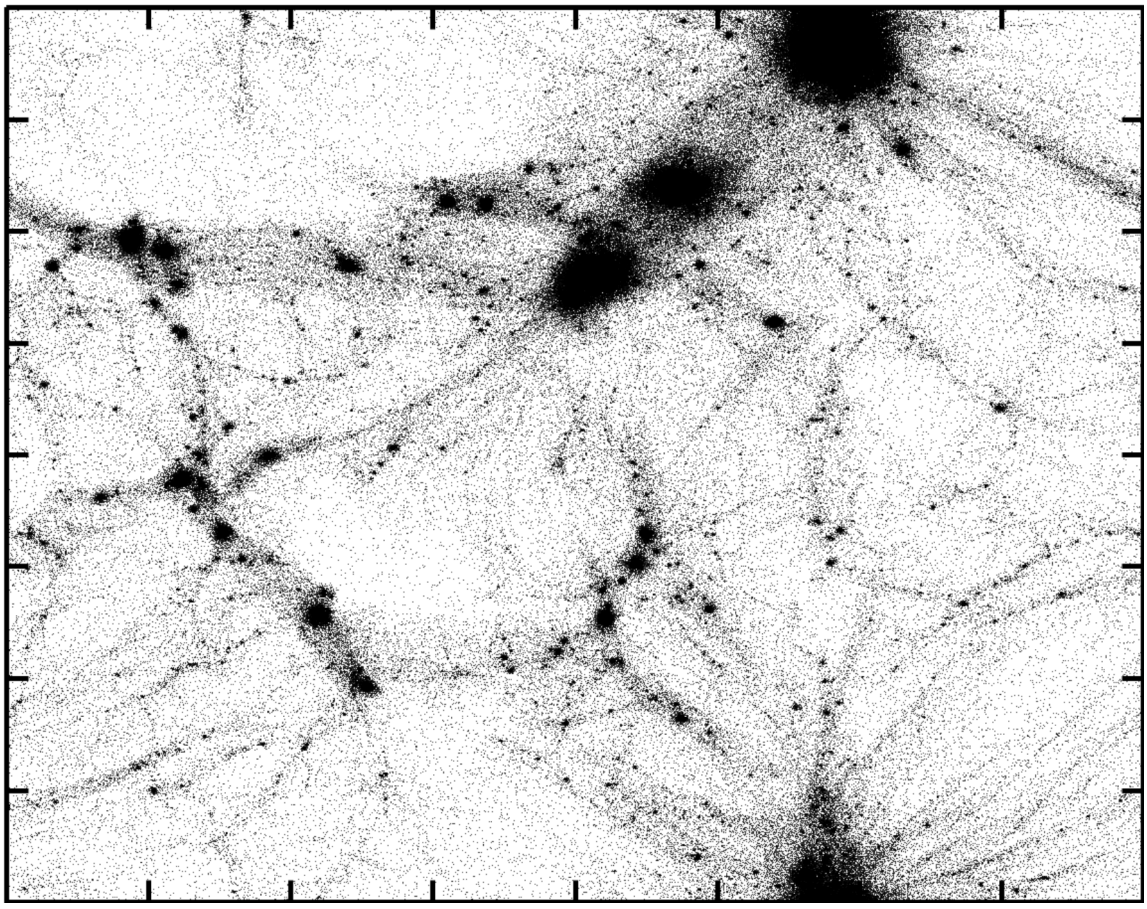

Fig. 1.1. Structure formation of CDM model in cosmological N-body simulation. The boxsize of the snapshot is 8 h^{-1}Mpc. Although LSS are on the scales of > 10 h^{-1}Mpc, the overdense region, the haloes and filaments, and the underdense regions, the voids, are also formed in the simulation. The figure is taken from (Jowett Chan et al., 2019).

bound on the cross section σ/m of dark matter. For instance, the Bullet Cluster gives an upper bound $\sigma/m < 5$ cm^{2}g^{-1}. The constraints are important bounds for the self-interacting type of dark matter.

1.1.3 Mass fraction

The mass fraction of dark matter within galaxies is expected to be $\sim 80\%$, so it dominates the matter content of galaxies. The dark matter fraction in comparison to other energy content in the Universe, however, could be predicted through the temperature fluctuation of the cosmic microwave background (CMB). The CMB has a spectrum that is consistent with a blackbody spectrum with a temperature of $T \sim 2.728$ K. The fluctuation of the temperature map provides rich information on the structure and evolution of the Universe. For instance, we statistically quantify the temperature fluctuation with angular power spectrum. The peaks in the power spectrum increase or decrease depending on the total matter density of the Universe. Therefore, modeling the CMB fluctuation can provide constraints, not only on

the fraction of dark matter but also on other cosmological parameters in the ΛCDM model. As such, CMB observation is considered a cosmological probe.

Planck Collaboration et al. (2020), as the most recent probe of the cosmological parameters using a combination of CMB temperature, polarization maps, and anisotropies, gave a dark matter density $\Omega_{dm} = 0.264$, a baryonic density $\Omega_b = 0.049$ and the remaining belong to the dark energy density. We can see that dark matter constitutes $\sim 80\%$ of the total matter content in the Universe. Such a result from the cosmological probe is surprisingly very close to the dark matter fraction in galaxies with flat rotation curves.

1.2 Dark Matter Halo

The cold dark matter model supported by the above observations assumes dark matter to be cold, collisionless, and the dominant matter content in the Universe, at least on scales larger than a galaxy. Here we discuss a gravitationally bound system in the non-linear regime based on solely the cold dark matter model, namely the halo. Although different dark matter models will have different consequences on the structure of the halo, they all must eventually form a halo due to gravity, so the discussion here is applicable to the later section of the thesis.

A halo is a virialized system that has relaxed into an equilibrium state. The definition of the halo is often obtained from the spherical collapse theory, which states that any gravitational system with a density of $\Delta\rho_{\rm m}$ will collapse to form a structure in a steady state. From the definition, we can calculate the corresponding halo mass and radius $M_{\rm h} = \Delta\rho_{\rm m} 4\pi r_{\rm h}^3/3$. Depending on the cosmology and assumption of the symmetry, different Δ could be obtained. Spherical symmetry without the consideration of the expansion gives $\Delta = 200$, whereas the latter, which is the adopted definition in this work, gives $\Delta = 350(180)$ for $z = 0(> 1)$ (Bryan & Norman, 1998). Both of them are common choices to define halo mass, so we must take care of the consistency with the definition throughout the analysis.

The physics behind the steady state of the halo requires understanding on the relaxation mechanism of the collisionlesss gravitational system. Intuitively, the steady state is reached due to the balance between the velocity dispersion and gravity of the dark matter. Mathematically, we must study the collisionless Bolzmann equation,

$$\frac{{\rm d}f}{{\rm d}t} = \frac{\partial f}{\partial t} + \sum_i \frac{\partial f}{\partial x_i} + \sum_i \frac{\partial \Phi}{\partial x_i}\frac{\partial f}{\partial v_i} = 0. \tag{1.2}$$

Since ${\rm d}f/{\rm d}t = 0$, the equation describes the equilibrium state of the distribution in phase space. In general, there is no analytical solution to the six dimensions partial differential equation, but with some assumptions, we can derive useful equations with physical results. For instance, we can derive the virial theorem for a static system

$$W = -2K, \tag{1.3}$$

where K is the kinetic energy, W is the potential energy, and the total energy is $E = K + W$ The theorem confirms the idea that the velocity of the particles balances the gravity, but additionally it quantitatively provides the required kinetic energy to counteract the gravitational potential.

The mechanism of reaching such a steady state is called the relaxation mechanism. Such theory is not studied in the spherical collapsed model, because the analysis often assumes spherical symmetry, so a system following a spherical collapse forms an oscillating system as an end state. However, we can estimate the time scale when a collisionless system is relaxed. By assuming a collisionless gravitational system with N bodies of radius r, we define the crossing time $t_{\rm cross} = r/v$ as the average time for a particle to go across the system. For typical stars in galaxy, they have $v \sim 200$ kms^{-1} and $r \sim 10$ kpc, so $t_{\rm cross} \sim 10^{10}$ yrs, which is smaller than Hubble time $t_{\rm H}$. The bodies in such a system only interact through gravity, and the two-body relaxation time, as the typical time scale to approximate the relaxation of a compact stellar system like a globular cluster, is

$$t_{\rm relax} = \frac{N}{10 \ln N} t_{\rm cross} \tag{1.4}$$

Unfortunately, for systems such as galaxies and dark matter halo with large N, the two-body relaxation time is much larger than Hubble time. Although the two-body relaxation is an intuitive relaxation mechanism, which simply averages the interaction between two bodies, it does not explain how a dark matter halo can relax within the age of the Universe. However, through studying the Boltzmann equation and N-body simulations, we found that several other mechanisms help relax collisionless systems more rapidly to the steady state, such as phase mixing and violent relaxation.

1.3 Density profile

The end state of the relaxation is the halo and its inner structure is an important prediction to be tested against observations. Such non-linear objects are only accurately predicted through high resolution N-body simulation of structure formation based on the CDM cosmology. Navarro et al. (1996) has shown that the inner structure, or more quantitatively the density profile, are self-similar. In other words, all density profiles, regardless of the size of the halo, have a steep rising logarithmic slope scaling with r^{-3} in the outer part and transition to a shallower slope scaling with r^{-1} in the inner part. Navarro et al. (1996) found an empirical equation to describe such a profile

$$\rho_{\rm nfw}(r) = \frac{\rho_0}{(r/r_{\rm s})(1 + r/r_{\rm s})^2}, \tag{1.5}$$

where $r_{\rm s}$ is the scale radius, and ρ_0 is a characteristic overdensity. It is easy to see that the profile has a -2 logarithmic slope at $r = r_{\rm s}$. The profile is now broadly referred to as the Navarro, Frenk, and White (NFW) profile. There are two free parameters $r_{\rm s}$ and ρ_0. The latter is related to the enclosed mass of the NFW profile

$$M(r) = 4\pi\Omega_{\rm m}\rho_0 r_{\rm s}^3 \left[\ln(1 + cx) - \frac{cx}{1 - cx}\right], \tag{1.6}$$

where $x = r/r_{\rm h}$ and $c \equiv r_{\rm h}/r_{\rm s}$ is the concentration parameter. In principle, the NFW profile can be characterized fully by the halo mass $M_{\rm h}$ and the concentration parameter. The former is often chosen, and the latter, however, is a more difficult parameter to obtain. Many high

resolution has provided an empirical relation between halo mass and the concentration, and found that the relation $c(M_{\rm h}, z)$ depends on redshift as well. We again emphasize that the NFW profile is an Universal profile defining the self-similar halos in CDM cosmology, but we remind that there exists an intrinsic scatter in the concentration-Mass relation.

For demonstration, Fig.1.2 shows the density profiles of several halo masses. All profiles show a transition from r^{-1} to r^{-3}, and for smaller halo mass, the transition occurs earlier. It implies that smaller NFW haloes are more concentrated than more massive haloes. We also show the circular velocity of those NFW haloes in Fig.1.3 based on Eq.1.1. Although halo can be defined by the virial radius $R_{\rm h}$, as shown in Fig.1.3, it can also be defined by the radius of maximum velocity $R_{\rm max}$. Since $R_{\rm max}$ is smaller than $R_{\rm h}$, it is more observationally possible to detect $R_{\rm max}$ than $R_{\rm h}$, for example in the rotational curve of galaxies.

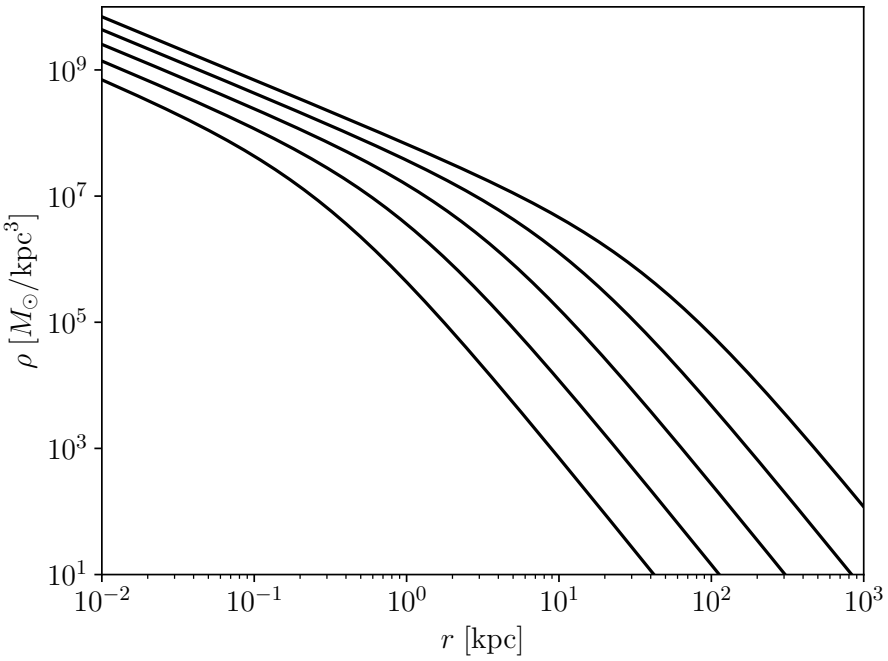

Fig. 1.2. The NFW density profile of halos with mass of 10^8,10^9,10^{10},10^{11} and 10^{12}. The halo is defined with $\Delta = 350$ at $z = 0$. We have adopted the concentration-mass relation provided by Ishiyama et al. (2021). We can clearly see how the profiles transition from a logarithmic slope of -1 to -3.

1.4 Challenges to the ΛCDM

The large scale success of the cosmological paradigm based on the CDM model is undeniably true, due to the confirmation by multiple observations mentioned in the previous section. However, the model is far from perfect. As the resolution of the cosmological N-body simulations become higher, we begin to robustly resolve the smaller structure and, more importantly, the substructure within each host haloes. We soon recognize that the

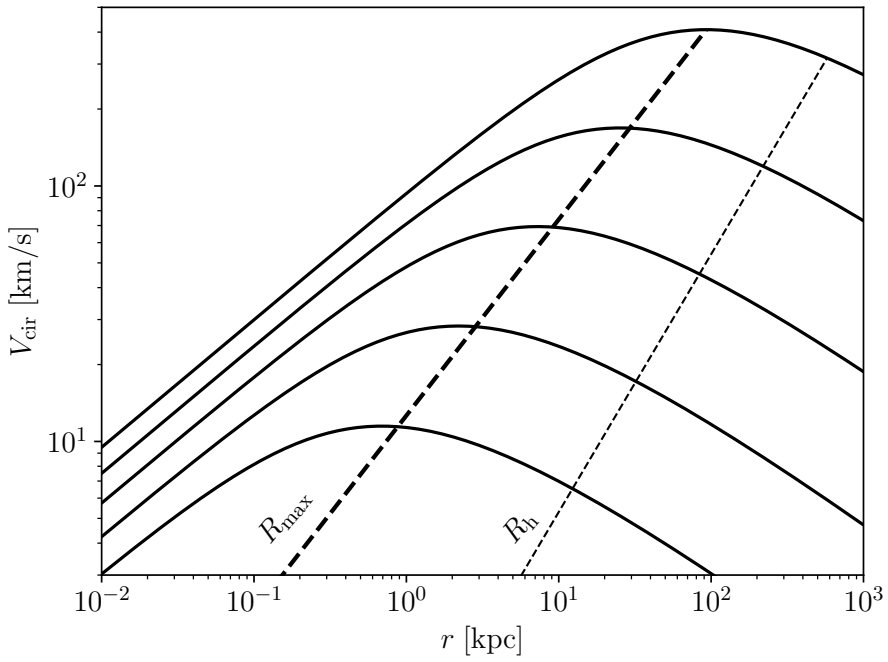

Fig. 1.3. The circular velocity of NFW profiles with halo mass of 10^8,10^9,10^{10},10^{11} and 10^{12}. The thin dash line shows the virial radius and the corresponding circular velocity of the haloes. The thick dash line shows the relation between maximum velocity and their corresponding radius $R_{\rm max}$. It is evident that $R_{\rm max}$ is smaller than the virial radius $R_{\rm h}$.

inner structure and the statistics of these substructures pose devastating problems to the ΛCDM model.

1.4.1 CDM-only simulation

Many high-resolution N-body simulations of the internal structure of MW-sized haloes have shown a large number of sub-haloes within it. These sub-haloes are virialzed objects within another larger virialized object. Moore et al. (1999) and Klypin et al. (1999) have pointed out one of the major issues of the CDM model: we expect ~ 1000 subhaloes in a MW-sized halo in the CDM only simulations, but we only observed $\sim 50-60$ dwarf galaxies within the MW. This is the so-called **Missing Satellite Problem**.

One of the reasons behind the problem is related to the observational limitation: the catalogs of dwarf satellites are still incomplete. There are limits in the survey depth and area which prevent us from detecting all the satellites. These limitations will result in the underestimation of the number of satellites. However, the situation has improved and more massive imaging surveys are now available. The Pan-StARRS 1 (PS1) survey (Chambers et al., 2016), the Dark Energy Survey (DES) (Dark Energy Survey Collaboration et al., 2016) and the Sloan Digital Sky Survey (SDSS) (York et al., 2000) have all discovered new ultra-faint dwarf galaxies with V-band absolute magnitude fainter than ~ -8 mag. For instance, Homma et al. (2019) has recently discovered a new ultra-faint dwarf, the Boötes IV based on the Hyper Suprime-Cam Subaru Strategic Problem (HSC-SSP). Unfortunately, even with

the newly discovered satellites, the number of dwarf galaxies is still far from reaching ~ 1000. Another possibility is the non-centrally concentrated radially distribution of satellites, which will be discussed later.

As mentioned previously, the inner structure of haloes, and also sub-haloes, follow the NFW density profile. The inner slope of a NFW profile scales as r^{-1}, which we called a cuspy profile. The next problem here is the disagreement between the inner slope of the observed satellite profiles and the cuspy NFW profile. Such a problem is demonstrated in the rotation curve of the dwarf galaxies. As shown in Fig.1.4, the inferred inner dark matter profile slopes from rotation curves of 26 dwarf galaxies prefer a cored profile, which has a logarithmic slope of 0, over the NFW profile. The problem is often referred to as the **core-cusp problem**.

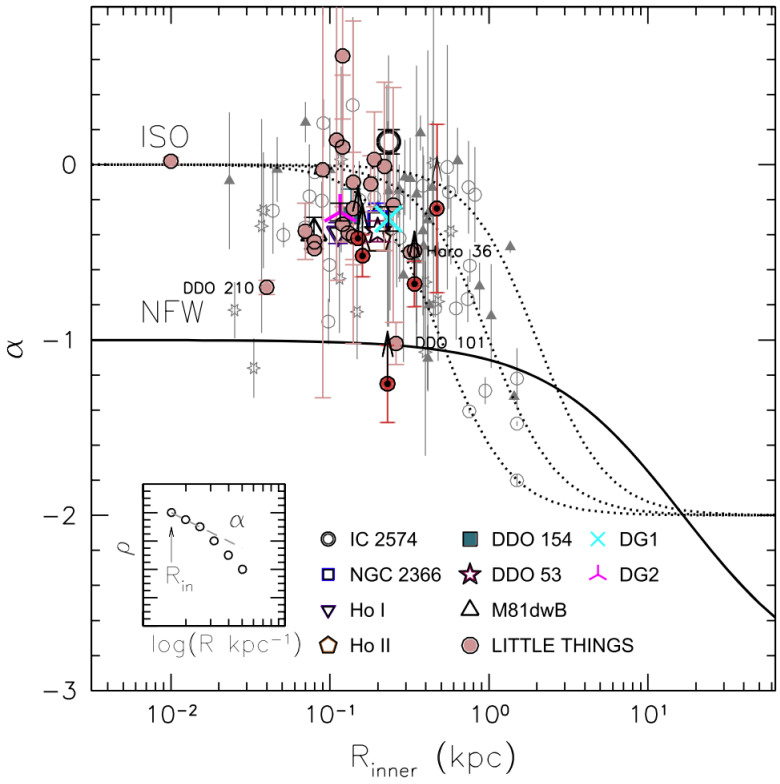

Fig. 1.4. The core-cusp problem demonstrated by the dwarf galaxies in the LITTLE THINGS and THINGS survey. α is the inner dark matter density slope at the innermost point $R_{\rm inner}$, where 0 and -1 correspond to a cored and cuspy profile respectively. A CDM dark matter halo follows the NFW profile, and it is evident that most data points deviate from the prediction by the NFW profile. The figure is borrowed from Oh et al. (2015).

Observationally, we can always improve the samples of stars within each satellite, but the core-cusp problem could also be related to the modeling method. For instance, Jeans analysis is one of those modeling techniques to estimate the dark matter density profile from the line-of-sight velocity of dwarf galaxies. However, it always assumes spherical symmetry and suffers from the mass-anisotropy degeneracy. Breaking degeneracy requires extra data on the proper motion of the stellar samples. There exist literature, that attempted to employ the non-spherical Jeans model Hayashi et al. (2020), and other modeling techniques

(see review Boldrini (2021)). Moreover, stars are very likely to be on non-circular orbits, especially for dwarf galaxies since they are not rotation-supported but dispersion-supported systems, so the dark matter profile of dwarfs inferred from the rotation curve may be prone to be inaccurate.

The previous two problems focus on the least massive subhaloes/satellites. The last well-known challenge to the ΛCDM model is the **Too-Big-To-Fail problem**, which focused on the most massive subhaloes in the simulations. Boylan-Kolchin et al. (2012) compared the circular velocity of subhaloes in simulation with the observed circular velocity at the half-light radii. They found that there exist some very massive subhaloes in the simulation that do not have an observational counterpart, but since the subhaloes are massive, we expect them to form stars and be detected easily. The Too-Big-To-Fail problem was initially identified using the satellites in the MW, but other groups subsequentially identify the same problem using dwarfs in Andromeda (Tollerud et al., 2008), and field dwarfs in the Local group (Kirby et al., 2014).

1.5 Hydrodynamic simulations

Well-known problems that challenge the ΛCDM model include the Missing Satellite Problem, the core-cusp problem (see Fig.1.4), and the Too-Big-To-Fail problem. These problems arose from comparing the CDM-only simulation with observation in the local Universe, and such a comparative study is indeed unfair because simulations were disregarding the influence of the baryonic component. It accounts for only a few percent of the energy content of the Universe, but we expect it to produce a feedback mechanism that can drastically change the inner structure of halos. Therefore, the community has developed several cosmological simulation codes that include hydrodynamics and baryonic feedback physics, allowing realistic simulation of galaxy formation. Due to the suppression of the small-scale structure by the supernovae feedback, the Missing Satellite Problem seems to be resolved (Sawala et al., 2016). The feedback mechanism also redistributes and reduces the inner density of the dark matter halo, creating cored density profile; thus, solving the core-cusp problem. The reionization reduces the circular velocity of the simulated dwarf galaxies, which end up being less massive than their dark matter only counterparts, and so, solving the Too-Big-To-Fail problem. The above evidence seem to suggest that ΛCDM is currently facing no serious problem, or at least the tension with observations is now greatly relaxed.

However, new challenges to the ΛCDM emerged in the past few years, and we will briefly summarize some of them here. Observations suggest that some dwarf galaxies have cuspy density profiles, such as Segue I, while some have an obviously cored density profile, like Fornax. The diverse structure of dwarf is not only presented in the density profile (see Fig.1.5) (Hayashi et al., 2020), but also in the rotation curves using the SPARC data set (Oman et al., 2015). Clearly, the core-cusp problem is now transitioned into **the diversity problem**. Although the diverse rotation curves are claimed to be solved by considering the non-circular motion of the gaseous disk, it remains an open issue.

Then, the Missing Satellite Problem is now transitioned to the opposite of it, the **Too Many Satellites Problem**. As the name tells, the additional baryonic component, especially the disk of the Milky Way galaxy, disrupts too many dwarf galaxies in the simulations,

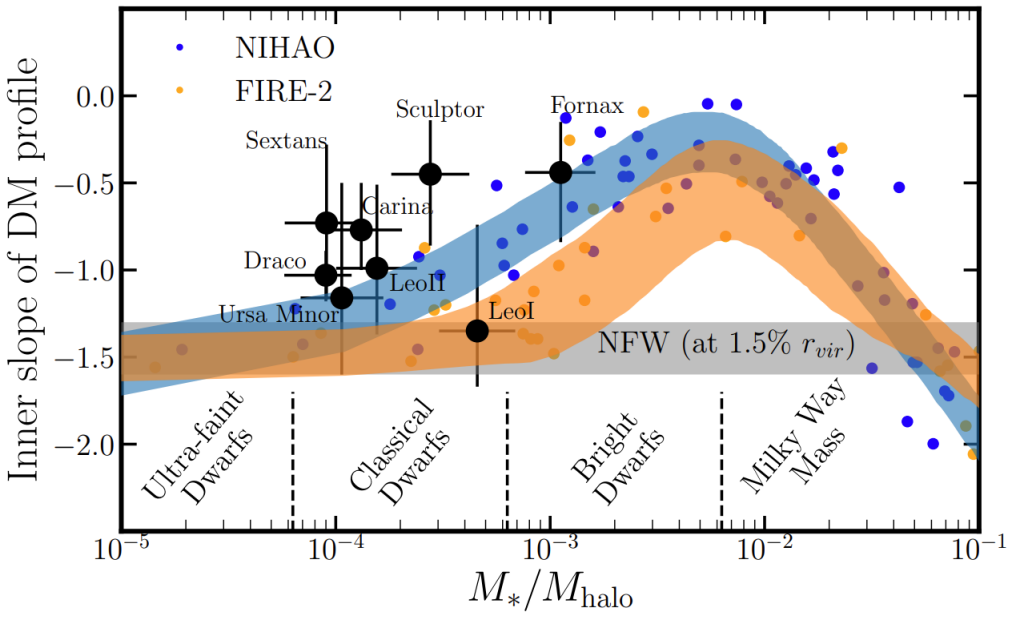

Fig. 1.5. A comparison between simulated and observed inner profiles of dwarf galaxies. The inner dark matter density slope at 1.5% of the virial radius of a dark halo as a function of the ratio between stellar and dark-halo masses $M_*/M_{\rm halo}$, of the dwarf galaxies. The blue and orange data are from hydrodynamical simulation NIHAO (Tollet et al., 2016) and FIRE-2. Black dots are observed inner slope of classical dwarf galaxies using Jeans analysis.The figure is obtained from Hayashi et al. (2020) with permission.

leading to much fewer satellites than observed. As shown in Kelley et al. (2019), in order to match the observed abundance of dwarfs, we need to populate sub-haloes with $V_{\rm peak} > 7$ km/s with galaxies, which is well below the hydrogen cooling limit $V_{\rm peak} \sim 16$ km/s (see Fig/1.6). Lastly, there is a feature of UFD galaxies that is not able to be explained by ΛCDM model. For instance, the survival of star cluster within Eridanus II suggests a large central core. The large core and the low velocity dispersion at the half-light radius of Crater I and Antlia II also cannot be explained by the tidal stripping effect. Again, UFD galaxies are gas-poor so baryonic feedback is very inefficient, and thus, cannot explain the core formation in these galaxies (Errani et al., 2022; Borukhovetskaya et al., 2022).

Homma et al. (2019) with their newly discovered ultra-faint dwarf, Boötes IV, found that the observed luminosity function shows an overprediction of the number of satellites. As shown in Fig.1.7, we expected around $1-2$ satellites with absolute magnitude $M_{\rm V} < 0$, but we observed 6 satellites instead. Homma et al. (2019) is, therefore, another independent study that is suggesting the Too-Many-Satellite-Problem to the ΛCDM model.

1.6 Dark Matter particle mass

Above are astrophysical challenges that ΛCDM are facing. To resolve them, we either improve our understanding of galaxy formation theory or/and dark matter physics. Much

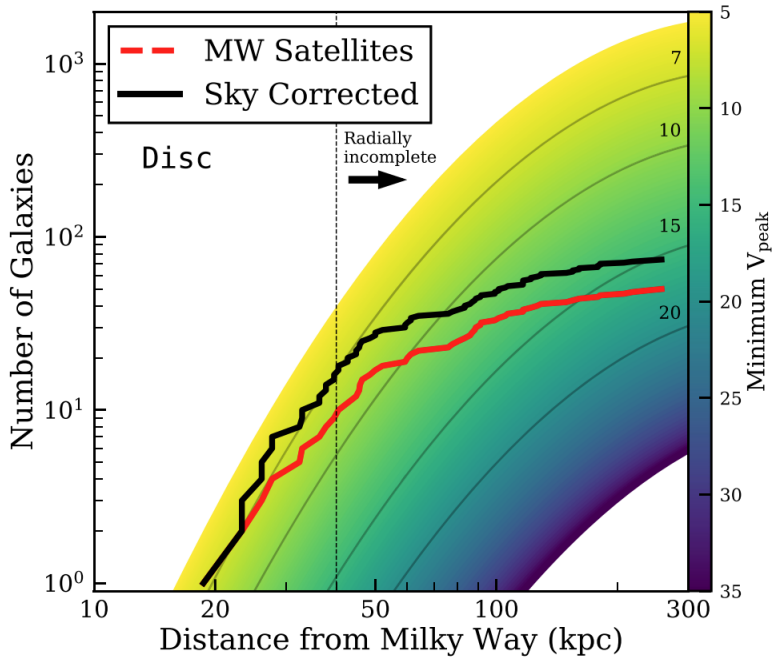

Fig. 1.6. Cumulative number of subhaloes in simulation compared with observed counts of satellites within the Milky Way. The grey lines are the cumulative number of simulated sub-haloes with peak velocity $V_{\rm peak}$ larger than 7, 10, 15 and 20 km s^{-1}. The simulations are performed only with dark matter but included an additional disk potential because the disk potential is the major baryonic component that disrupts sub-haloes. Peak velocity is the maximum velocity of the sub-haloes over their history. The black and red thick lines are the corrected and uncorrected counts of satellites respectively. To reproduce black line within 40 kpc, haloes with $V_{\rm peak} \sim 7$ km s^{-1} must form galaxies, which is contradicting because it is smaller than the hydrogen cooling limit(~ 16 km s^{-1}). The figure is obtained from Kelley et al. (2019) with permission.

effort has been made to model realistic galaxy formation physics on top of the N-body simulations (see review Vogelsberger et al. (2020)), but dark matter physics is far from being a complete theory. We can see this through the incredibly huge range of viable dark matter particle mass, which does not only present a problem to the astrophysics community because a different mass scale leads to different astrophysical consequences, but also a problem to the field of particle physics. Below shows a list of particle mass of viable dark matter models.

- Ultralight Dark Matter ($m > 10^{-22}$ eV)
- QCD axion ($10^{-5} - 10^{-6}$ eV)
- Warm Dark Matter ($10^{5} - 10^{9}$ eV)
- Weakly Interacting Massive Particle ($10^{9} - 10^{12}$ eV)
- Primordial Blackhole ($\sim M_{\odot}$)

As a brief review, Weakly-Interacting Massive Particle (WIMP) is the traditional preferred dark matter candidate of the CDM model, because its thermal relic abundance cor-

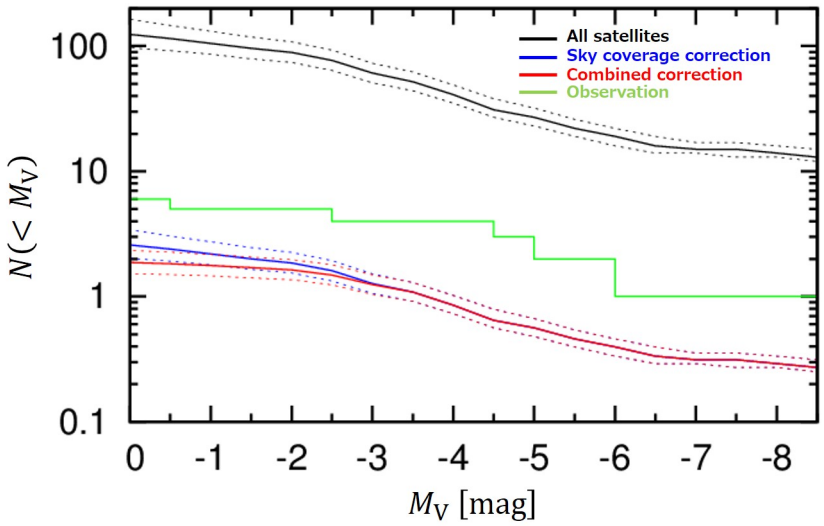

Fig. 1.7. The black line shows the total MW satellite galaxy luminosity function within 300 kpc predicted by Newton et al. (2018). The blue(red) lines shows the correction by sky coverage(associated with HSC-SSP survey). The green line is the observed luminosity function that consists of Sextans, Leo IV, Pegasus III, Cetus III, Virgo I, and Bootes IV.

responds precisely to the observed dark matter abundance in our Universe. This is also referred to as the WIMP miracle. While null detection was reported, detection of WIMP is still an ongoing research (Roszkowski et al., 2018). A slightly lighter mass than WIMP would be considered as the WDM model, where sterile neutrino is a promising candidate of it. The WDM particles are expected to decouple while relativistic, resulting in a suppression of smaller mass haloes. It has a motivation in the field of astrophysics because it can solve the Missing Satellite Problem without introducing baryonic feedback. For the lowest mass scale, we refer to it as the Ultralight Dark Matter (ULDM) model. A more detailed description will be postponed to a later chapter, but in short, the model is expected to solve both Missing Satellite and core-cusp problem at the same time. We refer the reader to Di Luzio et al. (2020) and Carr & Kühnel (2020); Villanueva-Domingo et al. (2021) for more details on QCP Axion and primordial black holes as dark matter models.

These dark matter models are all capable of reproducing the success of CDM on large scale, and therefore, we emphasize that *instead of distinguishing between CDM and non-CDM, we should focus on the following question: what is the mass of dark matter particle.* Direct detection with future experiments may give us some hints, but we can also make use of the observation in the local Universe again, such as the low-mass dwarf galaxies, to constraint the dark matter particle mass.

1.7 Numerical challenges

To compare with the observed substructure of the Milky Way, such as the dwarf galaxies and stellar streams, it requires an accurate understanding of the dark matter structure formation from numerical simulation. In fact, the falsifiability and success of the CDM

model are partly due to the well-developed technique for performing efficient N-body simulations. When starting the N-body simulations with a realistic initial condition predicted by CMB, we can predict the structure formation in the non-linear regime very well, such as the Navarro–Frenk–White (NFW) profile, the halo mass function, non-linear power spectrum, and the sub-haloes as the substructure of haloes. Mentioned above are verified by observations, and some of them are falsified, leading to the Missing Satellite and core-cusp problem. The efficient N-body method is now always implemented in cosmological hydrodynamic simulations because dark matter distribution is the backbone of galaxy formation.

So a well-developed and efficient numerical technique for performing dark matter simulation is essential, but the current studied technique in the field of dark matter physics only focuses on the simulation of the CDM model, whereas other models are much less studied. More importantly, they are known to face more numerical difficulties than the CDM model.

The WDM model assumes a type of dark matter particle that decouple while relativistic. The initial power spectrum is suppressed on scales smaller than the free streaming scale, leading to suppressed dark matter structure on those scales. Therefore, the simulation of WDM develops the same N-body method but starts with a modified initial condition. The resulting structure at lower redshift will be similar to CDM on large scale, whereas small-scale structures are suppressed. Unfortunately, it is known that there are equally spaced "spurious" haloes formed along the filaments, and these numerical artifacts need to be removed, in order to produce a realistic halo catalog. The method of eliminating the spurious haloes is the main difficulty in simulating the WDM model. Although several methods are proposed, such as glass simulation, and phase-space based halo finders, it still remains questionable whether removing structure in the simulation is physical. Moreover, hydrodynamics simulations could be influenced by these spurious haloes (Paduroiu, 2022).

Another example can be seen in the simulation of the ULDM model, as well as the focused model of this thesis the FDM model. Due to the low particle mass, the model has wave-like behavior on astrophysical scales. The equation of motion of this model is the Schrödinger-Poisson equation, instead of Newton's equation which is the equation for particle-like dark matter. The numerical technique of simulating ULDM is different and still in its infancy, but the difficulty in simulating it can be seen by the fact that no group can successfully simulate a MW-sized halo self-consistently, whereas N-body simulation has already achieved it as early as 30 years ago.

Again, these alternative models are still viable, because they could reproduce the large-scale structure of CDM. To distinguish them, thus, require a detailed understanding of the structure formation on galactic scales from simulation.

1.8 Main Motivation

In this thesis, we decide to focus on the Fuzzy Dark Matter model, which can address all of the issues above. The FDM model has been receiving a lot of attention recently given that it could naturally produce core in a halo and suppress structure formation on small scales while recovering the success of CDM on large scale. Schive et al. (2014b) successfully confirmed the above with realistic cosmological simulation, and, in addition, discover a relationship between the core and halo structure, making observational tests against dwarf galaxies possible. Here,

we again performed a simulation of the FDM model by numerically solving the Schrödinger-Poisson equation. The result of this thesis improved our understanding of the core structure, as one of the unique features of the FDM halo, by discovering diversity in the core-halo structure. Such diversity can explain the inconsistency in the core mass-halo mass relation among different groups. The observational connection of the discovered diversity with near-field cosmology is also discussed in the thesis.

Chapter 2

FDM cosmology and structure formation

FDM is a subclass of the ULDM, which assumes dark matter as ultra-light bosonic particles. A good starting point is to approximate the viable particle mass range of ULDM using the definition of the de Broglie wavelength

$$\lambda = \frac{h}{mv} \tag{2.1}$$

The upper bound on the mass comes from the fact that the largest de Broglie wavelength is of the order of the size of MW halo, $\lambda \sim R_{MW}$. The lower bound refers to the allowed smallest de Broglie wavelength, which is of order to the inter-particle distance between each boson. Since we know the matter density in the solar neighborhood ~ 0.4 GeVcm^{-3} (Bovy & Tremaine, 2012), the approximated bounds are

$$10^{-25}\ \text{eV} \leq mc^2 \leq 30\ \text{eV} \tag{2.2}$$

Roughly speaking, we can classify $mc^2 > 30$ eV as particle-like dark matter, and $mc^2 \leq 30$ eV as wave-like dark matter. For $mc^2 \ll 30$ eV , which is the case of FDM, the de Broglie wavelength is much larger than the inter-particle distance. The wave function of each boson overlaps leading to superposition, which, in the end, forms a macroscopic wave function describing the entire system. The time evolution of the FDM distribution is therefore described by only a single macroscopic wave function. We remind that this phenomenon is not new, but borrowed from condensed matter physics, where Bose-Einstein condensation and superfluity can form with the same quantum mechanism.

Since the FDM model is the focus of this thesis, here we show the de Broglie wavelength normalized with relevant units

$$\lambda = 0.2 \left(\frac{10^{-22}\ \text{eV}}{mc^2}\right) \left(\frac{v_{\text{MW}}}{v}\right) \text{kpc} \tag{2.3}$$

By assuming the typical FDM mass, $mc^2 \approx 10^{-22}$ eV, a MW-sized halo will correspond to $\lambda \sim 0.2$ kpc, whereas a dwarf galaxy with virial velocity ~ 10 km/s will have a wavelength of the order of their halo size. Therefore, the astrophysical size of the de Broglie wavelength must lead to observable astrophysical consequences, which we will discuss further in the next chapter.

2.1 Particle physics motivation

The particle candidate of FDM is an axion-like particle (ALP). We remind that axion has a particle mass $\sim 10^{-5}$ eV and an attractive interaction, whereas FDM assumes no interaction. The ALP for FDM is described by an action based on scalar field theory

$$S = \int d^4x\sqrt{-g}\left[\frac{1}{2}g^{\mu\nu}\partial_\mu\phi\partial_\nu\phi - V(\phi)\right], \tag{2.4}$$

where the integrand is called the Lagrangian density for scalar field. By assuming a homogeneous Friedman-Robertson-Walker background, and potential $V(\phi) = \frac{1}{2}m^2\phi^2$, we obtain the equation of motion for the homogeneous ALP. The details of the derivation is shown in Appendix A.1.

$$\ddot{\phi} + 3H\dot{\phi} + m^2\phi = 0 \tag{2.5}$$

This is the equation of harmonic oscillator, and the solution of it describes the cosmic evolution of the homogeneous scalar field. We can predict the relic density of ALP today using the equation, which is

$$\Omega_{\rm ALP} \sim 0.1\left(\frac{f}{10^{17}\ {\rm GeV}}\right)^2\left(\frac{mc^2}{10^{-22}\ {\rm eV}}\right)^{1/2} \tag{2.6}$$

The constant f refers to as axion decay constant (Hui et al., 2017), or the spontaneous breaking scale, that depends on the initial field value ϕ_i. Prediction from string theory leads to $f \sim 10^{17}$ GeV, which, by coincident, gives $\Omega_{\rm ALP} \sim 0.1$ if $mc^2 = 10^{-22}$ eV, similar to the observed matter density today $\Omega_m \sim 0.27$. We emphasize that WIMP particle is a strong candidate of the CDM model because of the WIMP miracle: the computed relic density of WIMP is of the same order of the observed matter density today. So the above relic calculation for the case of ALP demonstrates that *ALP is as equally competitive as WIMP*, because it can produce observed matter density today as well.

2.2 Perturbation Theory

So far, we are desribing scalar field as a homogeneous component. By applying perturbation theory, we can study Jeans instability and the initial power spectrum of the FDM model. The perturbed equation of motion for the density constrast $\delta = \delta\rho/\rho$ is

$$\ddot{\delta} + 2H\dot{\delta} + \left(\frac{k^2}{a^2}c_{\rm s}^2 - 4\pi G\rho\right)\delta = 0, \tag{2.7}$$

which is again an equation for harmonic oscillator with time dependent friction term $2H$, and mass term $(k^2c_{\rm s}^2/a^2 - 4\pi G\rho)$. The latter describes the competition between gravity and pressure. The effective sound speed depends on the perturbed fluid quantity $c_{\rm s}^2 \approx k^2/(4m^2a^2)$ (Hwang & Noh, 2009). On large scale, the gravity term dominates and leads to **Jeans instability**. The perturbation evolves in either growth mode $\delta \propto a$ or decaying mode $\delta \propto a^{-3/2}$, which is exactly same as the perturbed equation for CDM model. The difference

appears on small scale, where the pressure term dominates, and the perturbation oscillates without growth. We can compute the critical scale when the two competing term are equal $4\pi G\rho = k^2 c_{\rm s}^2/a^2$, which is know as the **axion Jeans scale**

$$k_{\rm J} = 66.5 a^{1/4} \left(\frac{\Omega h^2}{0.12}\right)^{1/4} \left(\frac{mc^2}{10^{-22}\ {\rm eV}}\right)^{1/2}\ {\rm Mpc}^{-1}. \tag{2.8}$$

We remind that density depends of scale factor $\rho \propto a^{-3}$. For small k mode $k < k_{\rm J}$, the gravitational instability means structure can form. For large k mode $k > k_{\rm J}$, oscillating perturbation means suppresion of structure formatioon, which is one of the major difference between CDM and FDM model. Alternatively, we could also compute the **Jeans length** $\lambda_{\rm J} = \frac{2\pi}{k_{\rm J}}$ and **Jeans Mass** $M_{\rm J} = \frac{4\pi}{3}\rho\left(\frac{\lambda_{\rm J}}{2}\right)$

$$\lambda_{\rm J} = 94 a^{-1/4} \left(\frac{10^{-22}\ {\rm eV}}{m}\right)^{1/2} \left(\frac{0.265}{\Omega_m}\right)^{1/4}\ {\rm kpc} \tag{2.9}$$

$$M_{\rm J} = 1.47\times 10^7 a^{-3/4} \left(\frac{0.265}{\Omega_{\rm m}}\right)^{3/4} \left(\frac{10^{-22}\ {\rm eV}}{mc^2}\right)^{3/2}\ M_\odot \tag{2.10}$$

Again, only structure with $\lambda > \lambda_{\rm J}$ or $M > M_{\rm J}$ can experience gravitational instability, leading to structure formation, so the Jeans mass approximates the minimum mass of halo forms in the FDM cosmology. In comparison to the CDM, which allows formation of halo down to $\sim 10^{-6}\ M_\odot$, FDM model with $mc^2 \sim 10^{-22}$ eV cna suppress formation of structure with mass $\leq 10^7\ M_\odot$, which is directly addressing the well-known Missing Satellite Problem without consideration of baryonic physics.

Based on linear theory ($\delta \sim 1$), the perturbation of FDM density on all scales is described by the power spectrum. The full calculation of the matter power spectrum requires solving the equation of motion of the perturbed dark matter Eq.(2.7) but also coupled with all the other perturbed components in the Universe (photon, baryons, neutrinos...) through gravity. Such numerical calculation, for the case of FDM model, are encoded in a publicly available program *AxionCAMB* (Hlozek et al., 2015). In short, the lienar perturbation tells that the powre spectrum of FDM model can be approxiamted by a modification relative to the ΛCDM model

$$P(k,z) = T^2(k,z) P_{\Lambda{\rm CDM}}(k,z) \tag{2.11}$$

where $P_{\Lambda{\rm CDM}}$ is the linear power spectrum of the CDM model, and the transfer function has the following form

$$T(k) = \frac{\cos x_{\rm J}^3}{1+x_{\rm J}^8}, \tag{2.12}$$

where $x_{\rm j} = 1.61(mc^2/10^{-22})^{1/18}(k/k_{\rm k,eq})$ and $k_{\rm k,eq} = 9(mc^2/10^{-22}{\rm eV})^{1/2}\ {\rm Mpc}^{-1}$ is the Jeans length at matter-radiation equality. Note that the redshift dependence on the Jeans length $k_{\rm J} \propto a^{1/4}$ is mild. Using *AxionCAMB*, we computed the linear power spectrum at z=0 depending on difference FDM mass shown in Fig.2.1. Note that Fig.2.1 is actually showing the dimensionless power spectrum $\Delta^2 \equiv k^3 P/(2\pi^2)$ because we can divide between linear and non-linear scale at $\Delta^2 \sim 1$. Although Jeans scale provides us an approximated scale when structure are suppressed, we see that from Fig.2.1, the suppression begins on scale

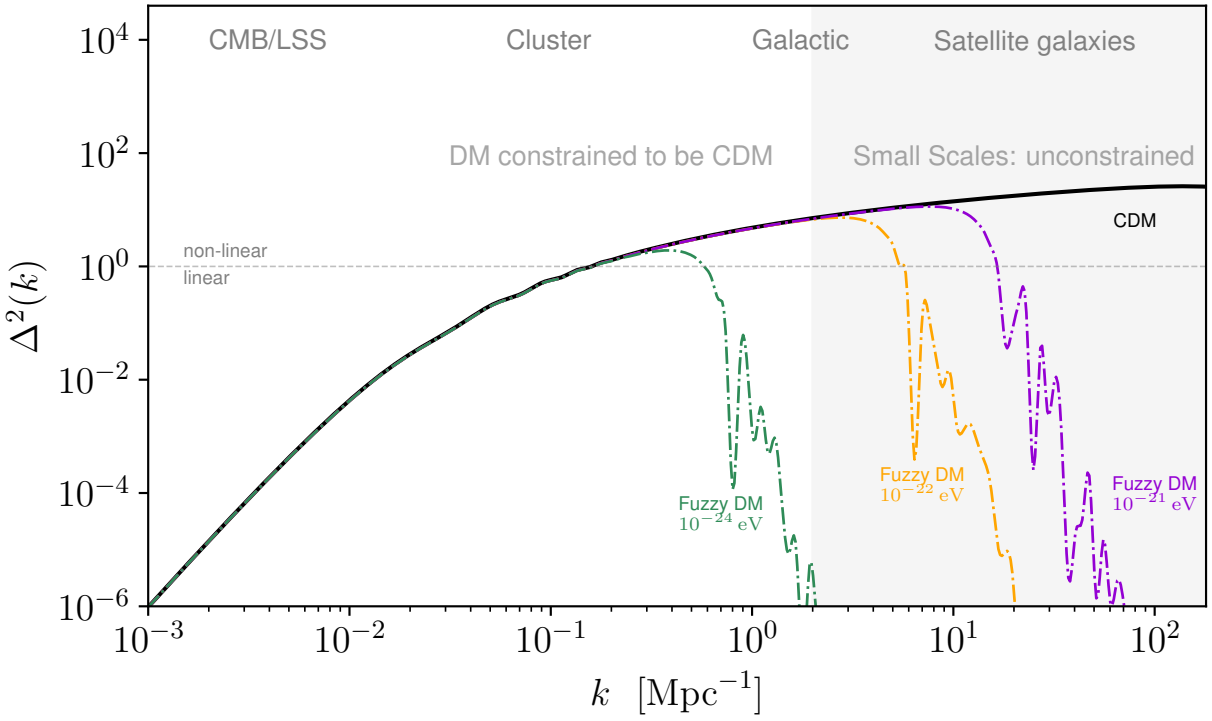

Fig. 2.1. Figure is modified from the original Ferreira (2020). The figure shows the dimensionless power sepctrum which can be probed by many observables from linear to non-linear scales. The solid black shows the prediction by ΛCDM model, whereas the colored lines shows the prediction by FDM cosmology with particle mass $mc^2 = 10^{-24}, 10^{-23}, 10^{-22}$ (green, yellow, purple). The power spectrums are genereated by AxionCAMB Hlozek et al. (2015).

smaller than Jeans scale $k < k_{\rm J}$. We can precislty define a scale as the the half mode $k_{1/2}$ where occurs at $T(k_{1/2}) = 0.5$

$$k_{1/2} = 5.1 \left(\frac{mc^2}{10^{-22}\ \mathrm{eV}} \right)^{4/9}\ \mathrm{Mpc}^{-1} \tag{2.13}$$

It is evident that we can test the FDM model with $mc^2 \sim 10^{-24}$ eV using linear observables such as CMB and LSS, whereas FDM with $mc^2 \geq 10^{-22}$ eV is not distinguishable from the CDM model on those scales, and can only be tested using non-linear observables. Non-linear structure formation, however, requires numerical simulation of the Schrödinger-Poisson system in order to predict physics accurately.

2.3 Non-linear theory

The non-relativistic and non-linear evolution of FDM is described by a different set of equations of motion in the above chapter, which assumes either homogeneous background or linear theory. The derivation is illustrated in more details in Appendix A.2 and , which lead to the equation of motion of FDM - **the Schrödinger-Poisson equation**

$$i\hbar \frac{\partial \psi}{\partial t} = -\frac{\hbar^2}{2ma^2}\nabla^2\psi + \frac{m\Phi}{a}\psi \tag{2.14}$$

$$\nabla^2\Phi = 4\pi G m(|\psi|^2 - \langle|\psi|^2\rangle), \tag{2.15}$$

The effect of the cosmological expansion is included in the scale factor $a = 1/(1+z)$, and all quantities are in comoving coordinate. In contrast to particle-like dark matter, which follows the Newton equations, $\dot{v} = \nabla\Phi$ and $\dot{x} = v$, it is evident that FDM model has wave-like behaviour desribed by the Schrödinger wave equation. The fluid quantity, density ρ and velocity v, are encoded in the wave function ψ which can be re-written in polar coordinate

$$\psi = \sqrt{\frac{\rho}{m}} \mathrm{e}^{i\theta}. \tag{2.16}$$

The amplitude depends on density, and the phase depends on the velocity

$$\rho = m|\phi|^2 \qquad v = \frac{\hbar}{am}\boldsymbol{\nabla}\theta \tag{2.17}$$

In Appendix A.6, we illustrate how to convert from velocity to phase which is an essential numerical technique to obtain cosmological initial condition from initial particle distribution. We emphasize that the Schrödinger-Poisson system is invariant under certain scaling symmetry

$$\{x, t, \rho, m, \psi\} \rightarrow \{\alpha x, \beta t, \beta^{-2}\rho, \alpha^{-2}\beta m, \alpha\beta^{-3/2}\psi\}. \tag{2.18}$$

Numerically, simulated structure formation is essentially the same, but with different physical quantities, when we apply the scaling relation above. This is helpful for us to observe how the structure change in different FDM mass m, without performing another

simulation. Beside the wave equation, we can convert Eq.2.14 into a fluid description - **the Madelung equations**. The full derivation, also called the Madelung transformation, is illustrated in Appendix A.4.

$$\frac{\partial n}{\partial t} + \frac{\hbar}{m}\nabla \cdot (n\boldsymbol{v}) = 0 \tag{2.19}$$

$$\frac{\partial \boldsymbol{v}}{\partial t} + \frac{1}{a^2}(\boldsymbol{v} \cdot \boldsymbol{\nabla})\boldsymbol{v} = \frac{1}{a}\frac{\hbar^2}{2m^2}\nabla\left(\frac{\nabla^2\sqrt{n}}{\sqrt{n}}\right) - \frac{1}{a^2}\nabla\Phi. \tag{2.20}$$

We can see that these equations resemble the continuity equation and Euler equation, but the latter contains an extra repulsive **quantum pressure** term $\nabla^2\sqrt{n}/\sqrt{n}$ that counteracts with gravity.

2.4 Wave phenomenology

The wave-like behavior of FDM presents rich phenomenology on small scale, that distinguishes itself from the traditional CDM or any other particle-like dark matter. We here review one of the most important features: the core formation in the FDM model.

From the modified Euler equation Eq.2.20, we can predict a structure in hydrostatic equilibrium that is balanced by gravity and quantum pressure. We call it the core, which is also referred to as the **soliton**. We assumed the left-hand side of the Euler equation to be 0. Then, we have

$$\frac{\hbar^2}{2m^2}\boldsymbol{\nabla}\left(\frac{\nabla^2\sqrt{\rho}}{\sqrt{\rho}}\right) = \boldsymbol{\nabla}\Phi. \tag{2.21}$$

It will be useful to make some quick prediction. If we assume spherical symmetry, approximate $\boldsymbol{\nabla} \sim R^{-1}$, and the gravitational force to be GM/R, we obtain

$$\frac{GM}{R} \sim \frac{1}{m^2R^2} \tag{2.22}$$

We can see that the size of the soliton is inversely proportional to its total mass, and also the square of the FDM mass. After normalizing it to relevant units,

$$R \sim 100\ \frac{10^9 M_\odot}{M}\left(\frac{10^{-22}\text{eV}}{mc^2}\right)^2\ \text{pc}, \tag{2.23}$$

a FDM mass of $mc^2 \sim 10^{-22}$ eV can form a sizable soliton within a dwarf-sized galaxy. A lighter FDM mass, will form a larger soliton which could, thererfore, be easily test against dwarf galaxies.

2.5 The Core

We remind that one of the important predictions by the CDM model is the mass distribution within the halo following the NFW profile, and such prediction allows CDM to test

against galaxies. CDM halo itself is balanced by velocity dispersion and gravity, whereas soliton is balanced by quantum pressure and gravity, so we do not expect the soliton to follow the NFW profile. We can gain more insight from the hydrostatic equilibrium Eq.2.21.

By applying divergence on both sides and the Poisson equation to the right hand side.

$$\frac{\hbar^2}{2m^2}\nabla^2\left(\frac{\nabla^2\sqrt{\rho}}{\sqrt{\rho}}\right) = 4\pi G\rho. \tag{2.24}$$

The solution can only be solved numerically and is called the soliton or also the Boson star. Note this is also the solution for Bose-Einstein condensate (BEC), a quantum bosonic structure in the ground state. The numerical details are shown in Appendix B.1, and Fig.2.2 shows the numerical solition as black line where density is normalized by core density, and radius is normalized by core radius defined as $\rho(r_{\rm s}) = \rho_0/2$. Since it is more convenient to have an empirical formula to predict the soliton profile, several groups provided an empirical equation that attempts to approximate the numerical solution (Chavanis & Delfini, 2011). Among them, the profile provided by Schive et al. (2014a), shown as a purple line in Fig.2.2, is the most frequently adopted in the observational analysis.

$$\rho_{\rm core}(r) = 1.9\times10^9 a^{-1}\left(\frac{10^{-23}{\rm eV}}{mc^2}\right)^2\left(\frac{\rm kpc}{r_{\rm c}}\right)^4\left(1+0.091\left(\frac{r}{r_{\rm c}}\right)^2\right)^{-8} \tag{2.25}$$

The empirical equation agrees well with the numerical solution up to $\sim 4r_{\rm c}$, and also agree with simulated core structure up to $\sim 3r_{\rm c}$ (Schive et al., 2014a). We remind that the core profile of the soliton is the essential feature that can solve the core-cusp problem. Another advantage of using Eq.2.25 is that it gives an analytical equation of the enclosed mass within the soliton depending on the radius

$$\begin{aligned} M_{\rm c}(r) = {} & \frac{4.2\times10^9 M_\odot}{mc^2/10^{-23}{\rm eV}(r_{\rm c}/{\rm pc})}\frac{1}{(a^2+1)^7}(3465a^{13}+23100a^{11}+65373a^9 \\ & +101376a^7+92323a^5+48580a^3-3465a+3465(a^2+1)^7){\rm arctan(a)}, \end{aligned} \tag{2.26}$$

where $a = (2^{1/8}-1)^{1/2}(r/r_{\rm c})$.

Besides the soliton profile, the soliton follows a tight core radius-core mass relation, such as Eq.2.23. A more accurate, and relevant radius-mass relation can be obtained from the hydrostatic assumption, but again we often adopt that came from simulation

$$a^{1/2}M_{\rm c} = \frac{5.5\times10^9}{(mc^2/10^{-23}\ {\rm eV})^2(a^{1/2}r_{\rm c}/{\rm kpc})}M_\odot. \tag{2.27}$$

From Fig.2.3, we show the core density profile with varying core mass. It is evident that a more massive core mass will lead to a smaller core radius following Eq.5.1. Since halo mass is proportional to core mass, as we will see in the next section, it also means increasing halo mass will result in a smaller core radius in FDM cosmology.

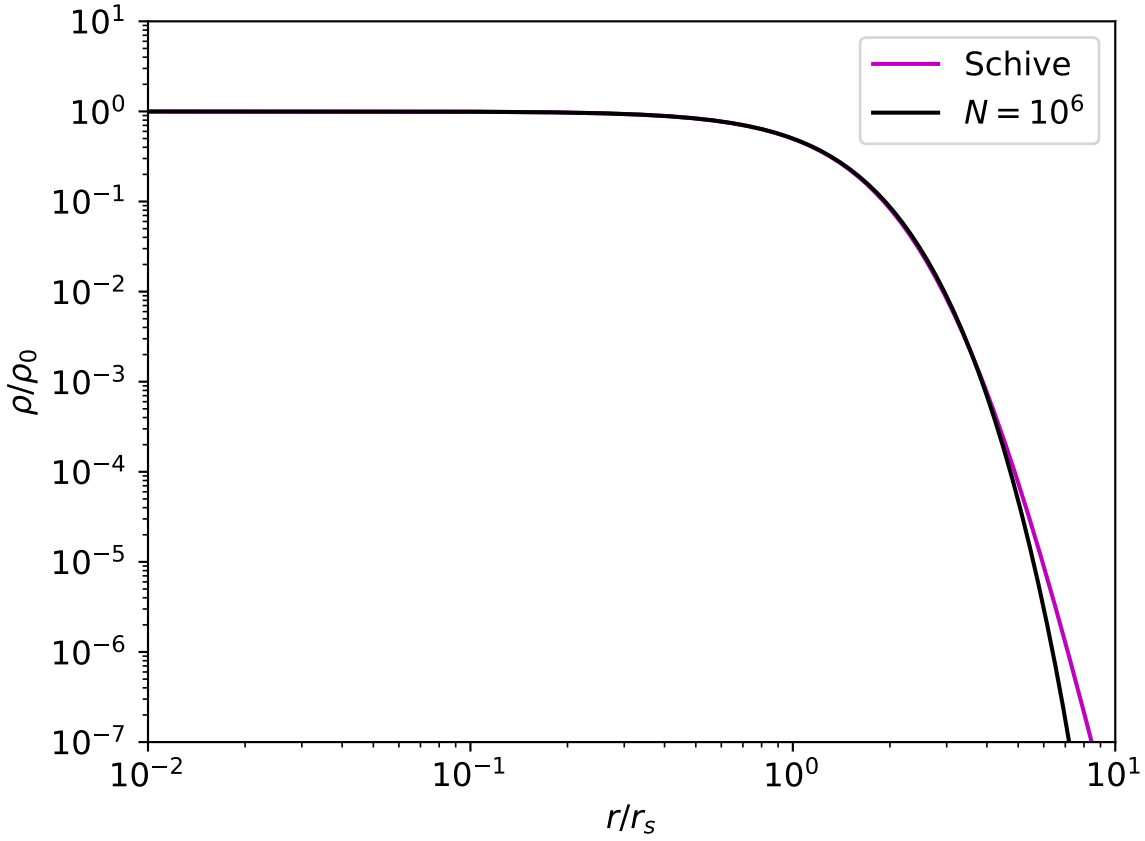

Fig. 2.2. Numerical solution to the soliton problem compared with the empirical function by Schive et al. (2014a). Density and radius are noramlized with core radius and density respectively.

2.6 The Core-halo structure

The above section has assumed that gravitating system is in hydrostatic equilibrium, but in general, a self-gravitating system of FDM is not always a soliton. The velocity term in the Euler equation, the left-hand side of Eq.2.20 can still play a role, where the velocity dispersion can counteract gravity. This mechanism is indeed the virialization mechanism of the dark matter halo. In the language of condensed matter physics, the soliton corresponds to the ground state of the bosonic system, so the non-vanishing velocity term is similar to the excited state of the system. Schive et al. (2014a) has performed a cosmological simulation of the FDM model and confirmed that all self-gravitating systems are indeed composed of two layers: the inner core formed by the balance between quantum pressure and gravity, and the outer envelope of the soliton, which is full of wave interference, formed by the balance between velocity dispersion and gravity. We always refer to this system as the core-halo

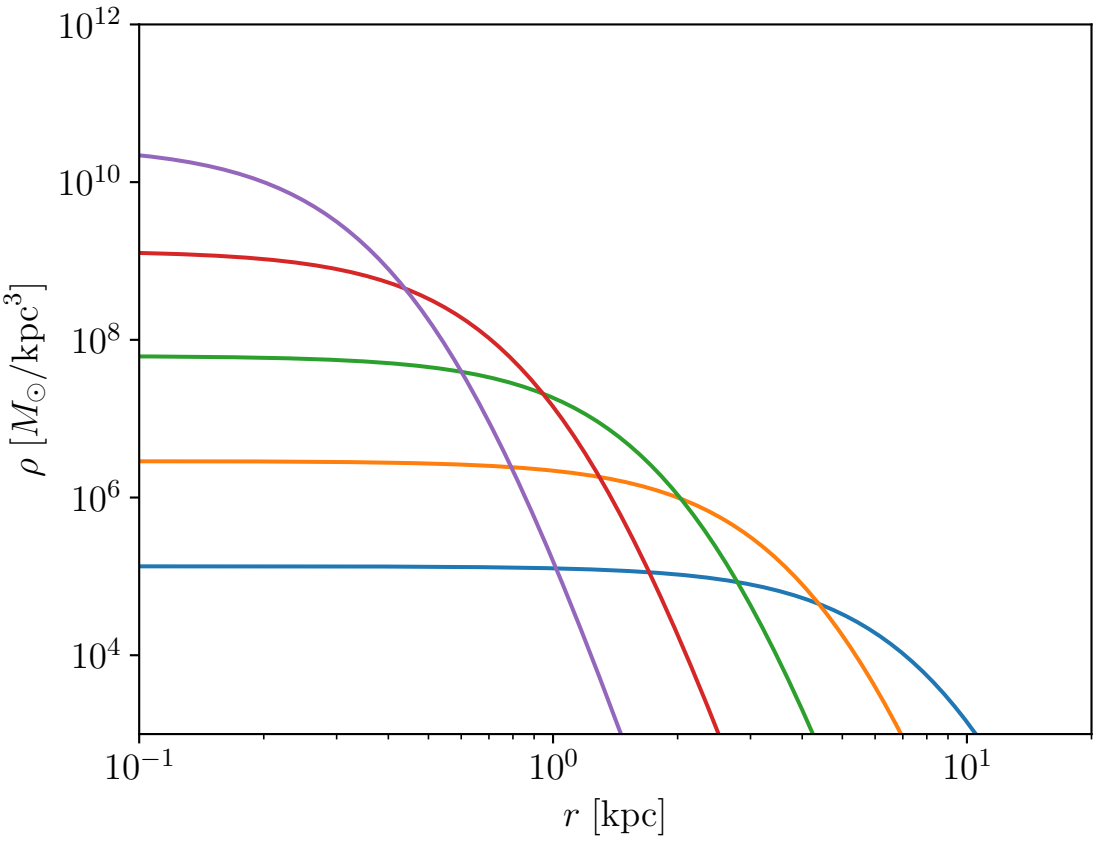

Fig. 2.3. Core density profile based on Eq.2.25 at $a = 1$. The corresponding core masses of the profiles are $10^{7.2}$(blue), $10^{7.5}$(orange), $10^{7.9}$(green), $10^{8.2}$(red) and $10^{8.5}$(purple) $M_\odot$, whereas the corresponding halo mass, according to Eq.2.31, are 10^8, 10^9, 10^{10}, 10^{11} and $10^{12} M_\odot$.

structure. The density profile can be described by the cored-NFW profile

$$\rho(r) = \begin{cases} \rho_c \left[1 + 0.091 \left(\frac{r}{r_c}\right)^2\right]^{-8} & , \text{for } r < r_t \\ \rho_s \left[\frac{r}{r_s}\right]^{-1} \left[1 + \left(\frac{r}{r_s}\right)\right]^{-2} & , \text{for } r \geq r_t \end{cases} \tag{2.28}$$

where the core profile is same as Eq.2.25. To ensure continuity between the cored and NFW profile, we must impose the condition that depends on the scale density ρ_s

$$\frac{\rho_s}{\rho_c} = \left[1 + 0.091 \left(\frac{r_t}{r_c}\right)^2\right]^{-8} \left[\frac{r_t}{r_s}\right] \left[1 + \left(\frac{r_t}{r_s}\right)\right]^2 . \tag{2.29}$$

The profile of core-halo structure has at least four free parameters (r_c, r_t, r_s, m), which denote as the core, transition, scale radius, and the FDM mass respectively. Previous simulations by Schive et al. (2014b) showed that the core structure is well fitted by the core profile Eq.2.25 with maximum error 2 % up to the transition radius $r_t \sim 3r_c$. For the outer region $r > r_t$, the profile follows the NFW profile.

We remind that this model, Eq.2.28 with Eq.2.29, does not guarantee a smooth transition because we only imposed continuity of the density. To do so, an extra continuity condition in the first derivative of the density must be imposed in addition to Eq.2.29 for the model to be both continuous and smooth. However, the resulting transition radius for a smooth transition is $r_{\rm t} < 3r_{\rm c}$, as was shown analytically in (Bernal et al., 2018), which is in disagreement with previous results from simulations (Schive et al., 2014b; Mocz et al., 2017). To be general, we allow $r_{\rm t}$ to vary.

Observational constraints on the FDM mass using the profile always require modeling of the core-halo structure. In other words, since the profile depends on 4 parameters, what is the allowed range for $(r_{\rm c}, r_{\rm t}, r_{\rm s})$? Are the parameters dependent on each other? By answering these questions will certainly help us to reduce the degree of freedom, and model a more physical FDM halo. Fortunately, Schive et al. (2014b) has found at least two external conditions to form a core-halo structure through numerical simulations:

$$r_{\rm t} \sim 3r_{\rm r} \qquad M_{\rm c} \propto M_{\rm h}^{1/3} \tag{2.30}$$

The first condition allows us to model the transition radius easily if the core radius is known in advance. We remind again that the core profile Eq.2.25 predicted by Schive et al. (2014a) also begin to deviate from the numerical soliton solution at $3r_{\rm r}$.

The second condition is more interesting, and controversial. It is called the **core-halo mass relation**. As the name tells, it means there is a relationship between the halo mass and the core mass. We remind that there the mass quantity can be easily converted in to radius using Eq.5.1 for $r_{\rm c}$, and halo definition[1] for $r_{\rm h}$. In principle, to derive a relation between them requires knowledge of how the wave interference, the outer envelope, interacts with the core at the center of the halo. Unfortunately, the exact physics of the interaction is not well known (but also see Chavanis (2019)). So an empirical relation between the core and halo mass is very helpful in the context of modeling the profile.

Unfortunately, the core-halo mass relation proposed by Schive et al. (2014b)

$$M_{\rm c} = \frac{1}{4\sqrt{a}} \left[\left(\frac{\zeta(z)}{\zeta(0)} \right)^{1/2} \frac{M_{\rm h}}{M_{\rm min,0}} \right]^{1/3} M_{\rm min,0}\,, \tag{2.31}$$

is under controversial debate, because *no other simulation group has successfully confirmed their relation.* In short, Schive et al. (2014b) obtain a slope of 1/3 in the relation, but others failed to do so. Here is a list of disagreements:

- Schwabe et al. (2016) performed idealised soliton merger simulations and were unable to reproduce $M_{\rm c} \propto M_{\rm h}^{1/3}$
- Mocz et al. (2017) used a larger halo sample with simulations of a similar setup and obtained a slope of $\alpha = 5/9$, disagreeing with $M_{\rm c} \propto M_{\rm h}^{1/3}$.
- Mina et al. (2020) found the same slope of 5/9 using cosmological simulations with a box size of 2.5Mpc/h.
- Nori & Baldi (2021) performed zoom-in simulations by including an external quantum pressure term in an N-body code, and obtained a relation with yet another value of the

[1] $M_{\rm h} = (4\pi r_{\rm h}^3/3)\zeta(z)\rho_{\rm m0}$

slope, $\alpha = 0.6$.

Such disagreements between multiple different studies indicate that there is still a fundamental lack of understanding of the core–halo structure in the FDM model, and also generates uncertainty in any constraints on the FDM mass which were obtained using $M_{\rm c} \propto M_{\rm h}^{1/3}$ or similar relations. The problem will be addressed as the main motivation of this thesis.

2.7 Relaxation time

Haloes are virialized systems assumed to be at a steady state, and here we discuss the mechanism and timescale for FDM halo to reach such a steady state. If we consider the case of CDM halo, we know that the two-body relaxation time for a collisionless system is several orders of magnitude larger than Hubble time, so the two-body relaxation must not be the main relaxation mechanism for the CDM halo. In fact, CDM halo relaxes through multiple physics, such as phase mixing, chaotic mixing and violent relaxation. The mechanism also must follow the collisionless Boltzmann equation. In the case of the core of the FDM halo, the time scale for the condensation of the core is studied by solving the Landau kinetic equation (Levkov et al., 2018). The time scale is

$$t_{\rm relax} \sim 10^6 {\rm yr} \left(\frac{mc^2}{10^{-22}\ {\rm eV}}\right)^3 \left(\frac{v}{30\ {\rm km/s}}\right)^6 \left(\frac{0.1 M_\odot}{\rho}\right)^2 \tag{2.32}$$

The resulting estimation has a time scale much shorter than the Hubble time, which agrees with a simulation where soliton condenses quickly with the halo. It also suggests that heavier FDM mass will lead to inefficient condensation of the soliton. This however remains to be confirmed with future simulations.

The relaxation mechanism of FDM haloe is called "gravitational cooling" where density waves are ejected to settle down the system into a steady state (Guzmán & Ureña-López, 2006). The waves can be easily seen in the formation of the FDM halo.

The end state is a virialized system that must follow the quantum virial theorem $Q/|W| \leq 1/2$. Derivation is shown in Appendix A.6. The total energy of the system can be derived from $E = \int \langle\psi|H|\psi\rangle\, d\mathbf{r}$,

$$E = \int \frac{\hbar^2}{2m^2}(\nabla\sqrt{\rho})^2 d\mathbf{r} + \int \frac{\rho v^2}{2} d\mathbf{r} + \int \frac{\rho V}{2} d\mathbf{r} \tag{2.33}$$

$$= Q + K + W \tag{2.34}$$

where Q, K and W are quantum energy, kinetic energy and gravitational potential energy. The quantum energy term signifies the difference between CDM and FDM gravitational system. For comparison, the virial theorem for CDM halo is $-2K = W$.

2.8 Theory exploration

On the non-linear regime, the core formation is not the only feature of the FDM halo that is different from the CDM halo. There also exists fluctuating **granules** surrounding the

core. Such substructures are inference patterns that were still not well studied. For instance, literature often assumed Gaussian distribution but what is the distribution of the granules in simulations? Does the size of the granules change with distance toward the center of the host halo? The interference contains regions with complete deconstructive interference, where density vanishes. Such regions are known as the **quantum vortices** which are ring-like structures swimming within the outer part of FDM halo (Hui, 2021). Although FDM simulations are expected to consist of quantum vortices, a robust characterization method of them remains to be studied in the future.

Chapter 3

Constraints on FDM mass

We have discussed the theories of the FDM model on the cosmological scale, linear and non-linear scale. Using the observables on different scales, we can test the theory and put constraints on the only free parameter of the FDM model, the FDM particle mass m. Fig.3.1 shows some of the most relevant constraints using various observations. Most of them are excluded bounds, while some constraints are obtained from dwarfs galaxies. This chapter will provide more details on each of these constraints, and also on those that are not included in Fig.3.1.

3.1 CMB and Large-scale structure

Hlozek et al. (2015) modified an existing self-consistent Boltzmann code, including the perturbed equation of motion for the scalar field in synchronous gauge (we remind that Eq.2.7 is in Newtonian gauge), to compute the CMB anisotropies and the matter power spectrum. They compare the prediction with a combination of CMB data from the Atacama Cosmology Telescope, the Wilkinson Microwave Anisotropy Probe (WMAP), the Planck satellite, and the South Pole Telescope with the LSS data from the WiggleZ galaxy-redshift survey. Their main results provide constraints on both the FDM mass m and the contribution to the cosmic energy density. They found that for $mc^2 \geq 10^{-24}$ eV, the model is indistinguishable from the CDM model, suggesting that such a mass range can reproduce the success of CDM on the cosmological scale. Intuitively, one can also see Fig.2.1 which agrees that $mc^2 \sim 10^{-24}$eV can be easily tested by CMB.

3.2 Lyman α forrest

At a high redshift in the range $2 \leq z \leq 6$, the low density fluctuation in the intergalactic medium (ISM) is still linear ($\delta \sim 1$). The neutral hydrogen gas, which is expected to trace the underlying dark matter fluctuation, manifests as absorption lines in the high redshift quasar spectra. Such absorption lines are called the Lyman-α forest. From that, we can measure the flux power spectrum, and use it to test the linear matter power spectrum predicted

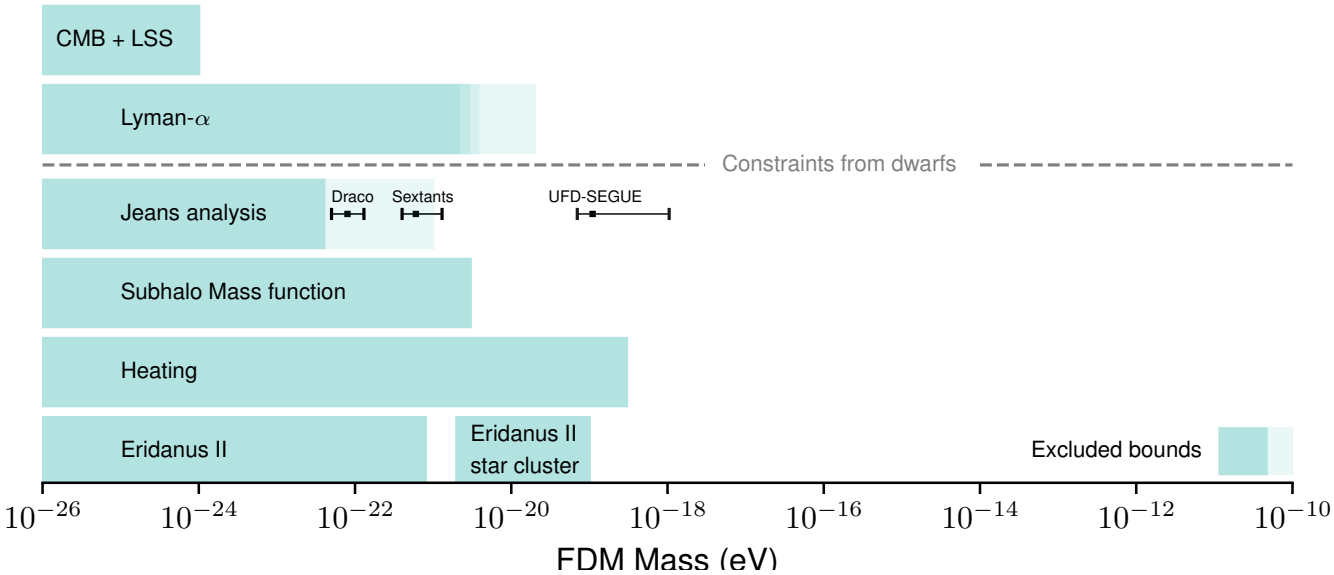

Fig. 3.1. A summary of the FDM mass constraints that are relevant to the theme of this thesis. The figure is inspired from Hayashi et al. (2021). Colored regions are excluded bounds, where a few data points with error bars are constraints. Excluded bound by cosmological observation of the CMB and LSS comes from Hlozek et al. (2015). The Lyman-α excluded bound is based on multiple studies (Nori et al., 2019; Iršič et al., 2017; Rogers & Peiris, 2021). Bounds and constraints made by Jeans analysis are based on a combination of studies (Schive et al., 2014a; Chen et al., 2017; González-Morales et al., 2017; Hayashi et al., 2020; Safarzadeh & Spergel, 2020). The strongest constraint is obtained by Hayashi et al. (2021) using data of Segue 1. A recent study found that granule heating of the stellar orbits in the Segue 1 and 2 also give similarly strong excluded bounds (Dalal & Kravtsov, 2022). Nadler et al. (2021) with his DES team used the abundance of MW satellites to test the predicted subhalo mass function of the FDM model and put a lower bound to the FDM mass. The constraint made by the survival of the star cluster in Eridanus II is directly related to soliton heating (Marsh & Niemeyer, 2019), however, Chiang et al. (2021) claimed that the tidal stripping effect can reduce the heating effect.

by any dark matter model. As we have discussed previously in Section 2.2, the quantum pressure of the FDM model suppresses the linear power spectrum on the scale smaller than $k_{1/2} \propto (mc^2)^{4/9}$. Since the cutoff scale depends on FDM mass, the effectiveness of Lyman-α forest depends on its resolution: the higher the resolution of the spectra can constrain heavier FDM mass. In practice, Lyman-α forest indeed can probe scales in between CMB and galactic scale, so they act as a powerful independent probe of the FDM mass.

The linear power spectrum only provides a crude estimation. We need to perform a full set of hydrodynamic simulations to model the distribution of the hydrogen gas in the ISM. This approach suffers from two disadvantages. Firstly, there is a degeneracy between IGM modeling parameters and the FDM mass. Moreover, although hydrodynamic simulation of

ΛCDM is possible, that of the FDM model is still difficult to perform. Studies therefore mostly used the N-body solvers with a modified initial condition, instead of solving the Schrödinger equation, which fails to capture the effect of quantum pressure in the non-linear structure formation.

Regardless of the limitations, the Lyman-α forest has provided some of the strongest bound to the FDM mass. Iršič et al. (2017) used a combination of the XQ-100 and HIRES/MIKE quasar spectra data set put a lower bound on the FDM mass $mc^2 > 2 \times 10^{-21}$eV. A more recent study by Rogers & Peiris (2021) adopted an emulator modeling technique to further push the lower bound to heavier mass $mc^2 \geq 2 \times 10^{-20}$ eV. We note that both studies still did not consider the effect of quantum pressure in their studies, but Nori et al. (2019) recently confirmed that the inclusion of the quantum pressure does not have a significant impact on the resulting bounds. These bounds posed issues to the FDM model because it seems to be in tension with bounds made by dwarf galaxies.

3.3 Halo mass function

We remind that the Missing Satellite problem stems from the observed abundance of satellite galaxies, so we could see that the abundance can constrain the fundamental properties of dark matter in general. Since the FDM model suppresses the formation of low-mass haloes, the observed abundance of the MW satellite galaxies can provide a constraint on the FDM mass. Nadler et al. (2021) with his Dark Energy Survey (DES) collaboration collected a set of MW satellite data from the DES and Pan-STARRS1. They modeled the suppression of the sub-halo mass function of the FDM model with a modified transfer function. They adopted an additional galaxy-halo connection modeling in their analysis to populate subhalos with satellite galaxies. They also consider the inhomogeneities in the spatial distribution of the MW satellites in the analysis. Their main result put a lower bound $mc^2 \leq 3 \times 10^{-21}$ eV.

Similar work was done by Schive et al. (2016), but instead of using the abundance of MW satellites, their observational data are from the population of high-z galaxies at $4 \leq z \leq 10$, which is manifested as a high-z luminosity function. Again, the FDM model suppresses the formation of galaxies at high redshift as well. They performed a N-body simulation with GADGET-2 with a modified initial condition, measured the high-z halo mass function, and converted it to UV luminosity functions. By comparing the observed luminosity function with the prediction, they obtained a lower bound on FDM mass $mc^2 \geq 10^{-22}$ eV.

The first study predicted subhalo mass function from the modified power spectrum, whereas the second study predicted halo mass function from N-body simulation. We stress that the halo is a non-linear structure, so prediction from simulation, not from N-body but Schrödinger solver, gives the most realistic halo mass function. May & Springel (2021) performed a large volume cosmological FDM simulation and provided a FDM halo mass function. Kulkarni & Ostriker (2022) although did not perform simulations, used Extended Press-Schechter formalism with a sharp k filter to predict the halo mass function analytically. They found that the $m \sim 2 \times 10^{-22}$ eV has a peak mass around $10^{10} M_{\odot}$, agreeing with Schive et al. (2016).

3.4 Circular velocity of field dwarfs

The circular velocity of dwarf galaxies is closely tied to the Too-Big-To-Fail problem, meaning that FDM mass can be probed by the observed velocity data. However, it is still difficult to measure the full velocity curves up to virial radius for faint galaxies with $M \sim 10^9 - 10^{10}\ M_\odot$, so we often use instead the circular velocity at half-light radius for each dwarf galaxies. At the same time, the structure of dwarf galaxies could be affected due to the tidal stripping effect from the host galaxies. To have a fair comparison, we should only consider data from field dwarf galaxies. Robles et al. (2019) collected half-light velocity of field dwarf galaxies and compare them with their FDM velocity curve models. They found that a particle mass $mc^2 \sim 10^{-22}$ eV can explain the observed velocities, therefore, the FDM model can address the Too-Big-To-Fail problem directly. However, they further found that their FDM velocity models are difficult to reproduce the galaxy rotation curves from the SPARC database. The reason is that the SPARC data contain data of ultra-diffuse galaxies, which are known to pose problems to the FDM model. We will postpone the discussion of the tension between ultra-diffuse galaxies and the FDM model to a later section. We stress that data from both field dwarfs and SPARC show a wide diversity in the rotation curves, which are closely related to the result of this work.

3.5 Jeans analysis

Besides the abundance of dwarf galaxies, their inner structure of them, or more specifically their density profile, is a very useful probe of the properties of dark matter. For instance, the core-cusp problem stems from the analysis of the inner structure of dwarf galaxies. Since the FDM halo generates a soliton core at the center, unlike the CDM halo which has a cusp, the size of the core in the dwarf galaxies must put strong constraints on the FDM mass. Indeed, there is already a large amount of literature that applies Jeans analysis to study the core size of dwarf galaxies. Here we describe shortly Jeans analysis.

Observed dwarf galaxies are composed on stars, which are tracers of the gravitational potential dominated by the dark matter. The spherical Jeans equation describes the stellar phase-space distribution depending on the provided dark matter halo mass distribution.

$$\frac{\partial[\nu(r)\sigma_r^2(r)]}{\partial r} + \frac{2\nu(r)\beta_{\rm ani}(r)\sigma_r^2(r)}{r} = -\nu(r)\frac{GM(r)}{r^2}\,, \tag{3.1}$$

where $\nu(r)$, $\sigma_r(r)$, and $\beta_{\rm ani}(r)$ are the stellar number density, radial velocity dispersion and orbital anisotropy, respectively. M(r) is the enclosed mass of the dark matter. Assuming that the stellar system is in dynamical equilibrium, which is not always true because dwarf can experience tidal stripping effect, we can fit the Jeans equation with the observed kinematic data to obtain information such as slope of the density profile, and the FDM mass. Depending on the model, the Jeans equation can have $3-10$ free parameters, and in practice, we need to apply Markov chain Monte Carlo algorithm (MCMC) to constrain the parameters. Here we summarize studies that adopted the Jeans analysis:

• Chen et al. (2017) found a particle mass of $mc^2 \sim 10^{-22}$ eV by analysing 8 dwarf spheroidal

galaxies

• González-Morales et al. (2017) made a different conclusion $mc^2 \leq 4 \times 10^{-21}$ eV using dwarf spheroidal galaxies Fornax and Sculptor.

• Calabrese & Spergel (2016) performed Jeans analysis on two UFDs, Draca II and Triangulum II, and found $mc^2 \sim 4 \times 10^{-22}$ eV.

• Safarzadeh & Spergel (2020) gathered data from both dwarf spheroidals and UFDs concluded that the data are incompatible within the theory of FDM model.

• Hayashi et al. (2020, 2021) have studied the both UFDs and spheroidals with much larger data sets, but they obtained a strong constraint $mc^2 \sim 10^{-19}$ eV using Segue 1.

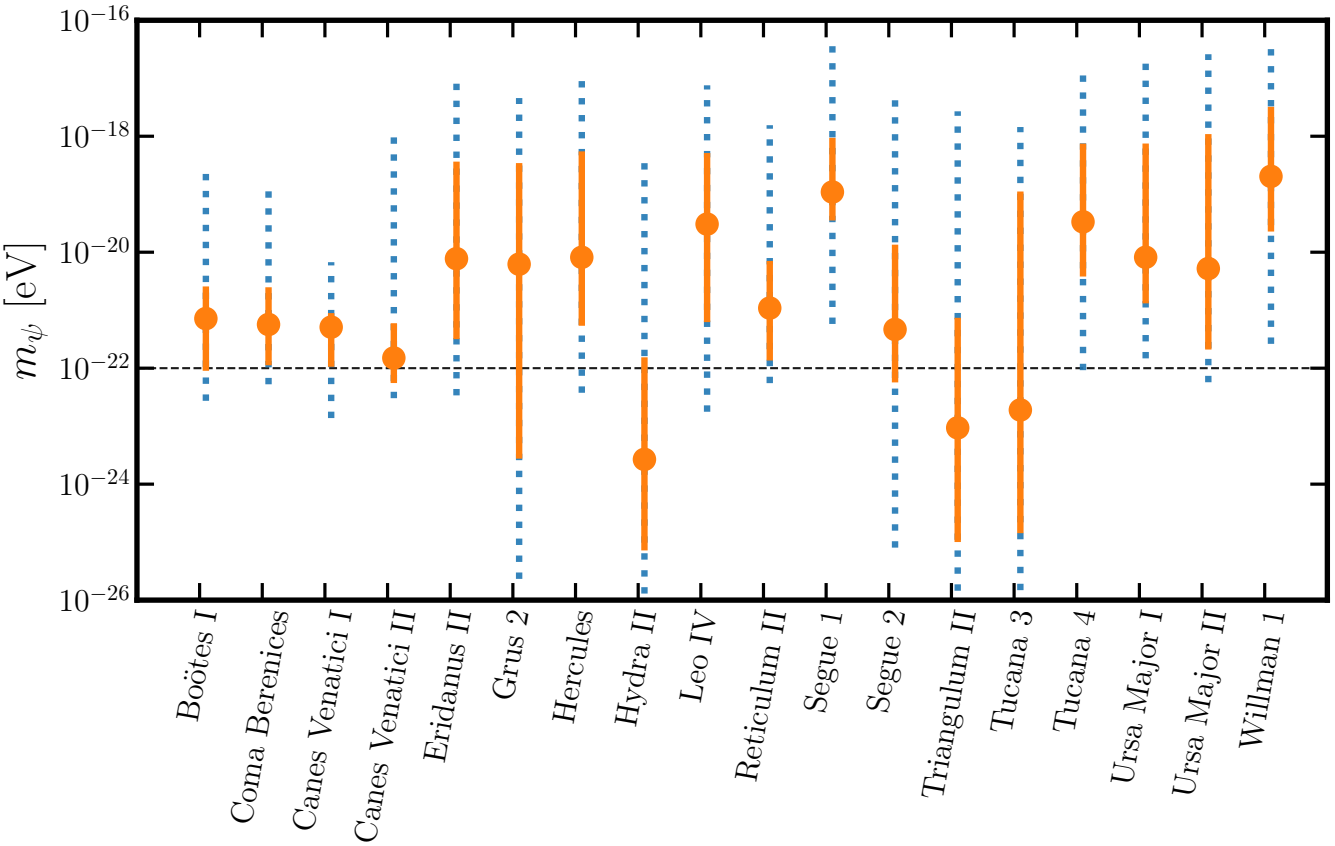

Fig. 3.2. The figure shows the estimated FDM particle masses, m_ψ, for 17 ultra-faint dwarfs. The orange points show the median values. The orange and blue dotted errors are $1-$ and $2-\sigma$ credible intervals. The horizontal dashed line corresponds to $m_\psi = 10^{-22}$ eV. Figure is borrowed from Hayashi et al. (2021).

Most of the bounds made by dwarf galaxies favor $mc^2 \geq 10^{-22}$ eV, except for Segue I. In fact, it is known that Segue I has a rather small core, which favors a heavier FDM

particle mass. Thus, it is evident that different dwarf galaxies predicted FDM mass between 10^{-22} eV $\leq mc^2 \leq 10^{-19}$ eV, so a certain FDM mass cannot seem to explain the profile of all dwarf galaxies at once, which is the argument of Safarzadeh & Spergel (2020). A similar argument could also be seen in Fig.3.2, which is borrowed from Hayashi et al. (2021). They estimated the FDM mass using 17 ultra-faint dwarfs and found that most of them, again, favors $mc^2 \geq 10^{-22}$ eV, but also show a variation of FDM mass. We emphasize this is simply another presentation of the diversity problem - dwarfs galaxies can have both core or cuspy inner profiles. We will discuss later that the main result of this thesis, the diversity of the core-halo structure of the FDM model, could address the diversity problem stated here.

3.6 Dynamical heating

The interference pattern, or in other words the granules, interacts with the soliton and causes the soliton the oscillates around the center of the halo. As a result, the oscillation of the soliton can heat the stars cluster and disrupt it in the end. Marsh & Niemeyer (2019) studied the survival of the star cluster in the UFD, Eridanus II, and found a strong constraint on the FDM mass $\sim 10^{-19}$ eV. However, the analysis ignores the fact the Eridanus II could be tidally stripped, where the oscillation will be drastically reduced (Chiang et al., 2021).

Another form of heating is generated by the fluctuation of the granules.Dalal & Kravtsov (2022) studied the size and the velocity dispersion of Segue I and II, and put a strong constraint $mc^2 \geq 3 \times 10^{-19}$ eV on the FDM model. The constraint is similar to the constraint made by Hayashi et al. (2021) using Segue 1. Again, Dalal & Kravtsov (2022) only applied their analysis to UFDs that have a small core. It will be interesting to see if a small FDM mass will be obtained using UFDs with large cores such as Crater I and Antlia II.

3.7 Future astrophysical probes

Above we summarized some of the linear and non-linear observables that were often used to constrain the FDM model. To close this section, we will lastly discuss some of the prospects of other observational probes.

Starting with something more familiar, improvements can still be made to modeling the kinematics of dwarf galaxies. Spherical Jeans analysis was always the adopted methodology, but it is known to suffer from a degeneracy between the mass and anisotropic parameter. There already exists literature that improves the Jeans analysis. Hayashi et al. (2020) applied non-spherical Jeans analysis to 8 spheroidal dwarf galaxies. Walker & Peñarrubia (2011) also proposed another method that can measure the inner slope by combining Jeans analysis with the chemo-dynamically distinct stellar sub-components of the dwarf galaxy. Although it is not related to the Jean analysis, the Schwarzchild dynamical model Schwarzschild (1979) is another promising method to realistically reproduce the full mass profile of a galaxy. Observational improvement on the kinematic data will be discussed in the later section, which is related to the upcoming spectroscopic survey by The Subaru Prime Focus Spectrograph.

Besides modeling the dwarf galaxy, we can also study the dynamical friction problem originating from the globular clusters of Fornax. Clearly, the core formation in the FDM

model could easily solve the problem, but further analysis or simulations are needed in order to understand the effects of the granules.

As mentioned, one of the most distinctive features of a FDM halo, besides the core, is the granular structure. These are interference substructures on the scales of the de Broglie wavelength. Such features could be signatures in at least two observables: stellar streams and gravitational lenses. For instance, Dalal et al. (2021) generated the effect of granules by evolving a realistic wavefunction in a static gravitational potential. They showed that it is possible to determine the FDM mass through the density perturbation in the streams. It is also expected to have improved stellar stream data of, for instance, GD-1 and Palomar 5, from further Gaia data releases in the future. Kawai et al. (2022) has attempted to constrain the FDM mass by modeling the fluctuation in the strong lensing system SDSS J0252 + 0039 with an analytical model. We expect future higher resolution observation, for instance by ALMA, can provide a stronger constraint on the FDM mass.

Chapter 4

Numerical Simulation of FDM

To test the FDM model against dwarf galaxies, we need an accurate prediction of the structure formation of it. To fully capture the non-linear structure formation of the FDM model, we must solve the time-dependent Schrödinger-Poisson equation given in Eq.2.14. There are numerous methods proposed to solve it, but in this work, we decided to adopt the **pseudo-spectral method**. Before we dive into the introduction of the pseudo-spectral method, we here state the factors to consider when choosing a numerical method:

- Order of accuracy in time and space
- The stability condition/Convergence condition
- Mass and energy conservation
- Computational cost

Lastly, based on the structure of the mesh or the spatial discretization method, a different conclusion will be made. In this work, we will assume uniform spatial mesh and finite difference methods since they are the easiest to implement from scratch. The best method must therefore be high order of accuracy in time and space, stable with large time steps, conserve mass and energy and have the least computational cost. For a more detailed description of other numerical Schrödinger solvers, we refer the reader to Appendix B.2. In Chapter.4.1, we discuss the tests we have performed to verify the convergence and stability of our numerical algorithms.

The time-dependent Schrödinger–Poisson (SP) given in 2.14 and 2.15 are discretized on a uniform spatial grid and evolved from timestep n to the next timestep using the Strang splitting pseudo-spectral method. Please refer to Appendix B.2 for more numerical details, but the main idea is to split the Schrödinger-Poisson equations into three steps:

$$i\hbar\frac{\partial\psi}{\partial t} = \frac{m\Phi}{a}\psi \qquad \text{(half step)} \tag{4.1}$$

$$i\hbar\frac{\partial\psi}{\partial t} = -\frac{\hbar^2}{2ma^2}\nabla^2\psi \qquad \text{(full step)} \tag{4.2}$$

$$i\hbar\frac{\partial\psi}{\partial t} = \frac{m\Phi}{a}\psi \qquad \text{(half step)} \tag{4.3}$$

$$\tag{4.4}$$

The problem is now simplified to solving the Schrödinger equation with only the diffusive term, which is just a diffusion equation but wave function is complex, and the potential term. The latter can be solved exactly by an **exponential integrator** $\psi^{n+1} = \mathrm{e}^{K\Delta}\psi^n$. The Schrödinger equation with only the diffusive term can be solved by spectral method. We first Fourier transform the equation, so the Laplace operator $\nabla^2 \to -k^2$ where $k^2 = k_x^2 + k_y^2 + k_z^2$, then the resulting transformed equation $\mathcal{F}[\psi^{n+1}] = \mathrm{e}^{D\Delta}\mathcal{F}[\psi^n]$ can be solve exactly again using exponential integrator. In summary, we can express the Strang spitting spectral method in one equation

$$\psi^{n+1} \approx \mathrm{e}^{K\Delta t}\mathcal{F}^{-1}\left[\mathrm{e}^{D\Delta t}\,\mathcal{F}\left[\mathrm{e}^{K\Delta t}\psi^n\right]\right] , \tag{4.5}$$

where $K = -\mathrm{i}m\Phi/(2\hbar a)$, $D = -\mathrm{i}\hbar k^2/(2ma^2)$, and $\mathcal{F}$ denotes the Fourier transform operator. This scheme is second-order accurate in time and exponentially accurate in space. Each full-time integration is divided into three steps, which is similar to the symplectic leapfrog, kick-drift-kick, integrator. Before applying the kick operator $\mathrm{e}^{K\Delta t}$, the potential Φ must be updated by solving the Poisson equation shown in 2.15.

There are two limitations to this method. Since the numerical method is explicit, the choice of time step must follow a Courant–Friedrichs–Lewy (CFL)-like condition. In this case, the phases of the exponential operators must be smaller than 2π:

$$\Delta t < \min\left\{\frac{4}{3\pi}\frac{m}{\hbar}\Delta x^2 a^2,\ 2\pi a\frac{\hbar}{m\,|\Phi_{\max}|}\right\} , \tag{4.6}$$

where $|\Phi_{\max}|$ is the maximum value of the potential. The scale factor for the next time step is approximated by $a_{\mathrm{next}} \approx a + Ha\Delta t$, which is later used to calculate the time steps for the kick and drift operators. At early times, the CFL condition is determined by the drift operator. As the gravitational potential becomes deeper at later times, the kick term begins to control the choice of time step. For example, $\sim 90\%$ of the computational time is controlled by the drift term in our simulations. The scheme restricts this work to simulations of less massive haloes, because the core radius–halo mass relation $r_{\mathrm{s}} \propto M_{\mathrm{h}}^{-\alpha}$ implies that a higher spatial resolution is required to resolve the small core radius of a massive halo, leading to smaller time steps based on the CFL condition $\Delta t \propto \Delta x^2$.

The second disadvantage of this scheme is that it is only applicable to uniform mesh because Fourier transform requires grids to be uniformly spaced. If one adopted the AMR scheme, the spectral method cannot be adopted. We must give up the spectral accuracy and return to the lower order method.

Previous core–halo relations are obtained from different types of simulations. The most general way is to perform a cosmological simulation, but these simulations are often restricted to end before redshift $z = 0$ and the number of well-resolved cores is limited due to computational difficulties. A cheaper approach is to perform non-cosmological simulations of soliton mergers. This approach allows more control of the resolution and the final halo mass but is at risk of simulating unrealistic haloes due to the idealized, non-cosmological initial conditions.

4.1 Qualitative Tests

We have performed several tests for our Schrödinger-Poisson solver:

- Propagation of a gaussian wave packet
- 1D Gaussian wave mergers
- 3D Cosmological simulation
- Comparison with other cosmological FDM code

We stress that there is no analytical solution for the Schrödinger-Poisson system, but there is an analytical solution for the Schrödinger equation without the potential term when the initial condition is a Gaussian wave. It is known as the Gaussian wave packet (Brandt et al., 1986). The evolution of a 1D wave packet follows $\psi_{\rm GWP}(x,t) = M(x,t)e^{i\theta(x,t)}$, where

$$M(x,t) = \frac{1}{(2\pi)^{1/4}\sigma_x^{1/2}} e^{-(x-x_0-v_{x0}t)^2/(4\sigma_x^2)}$$

$$\theta(x,t) = \frac{1}{\hbar}\left[mv_{x0} + \frac{\sigma_{px}^2}{\sigma_x^2}\frac{t}{2m}(x-x_0-v_{x0}t)\right](x-x_0-v_{x0}t) + \frac{v_{x0}^2 m}{2\hbar}t - \tan^{-1}\left(\frac{2\sigma_{px}^2 t}{\hbar m}\right)\frac{1}{2}$$

and $\sigma_x^2 = \frac{\hbar}{4\sigma_{px}^2}\left(1 + \frac{4\sigma_{px}^4 t^2}{\hbar^2 m^2}\right)$. The 3D solution is simply

$$\psi_{\rm GWP}(x,y,z,t) = M(x,t)M(y,t)M(z,t)e^{i[\theta(x,t)+\theta(y,t)+\theta(z,t)]}.$$

Since this is an analytical solution, we can rigorously test any Schrödinger solver with the wave packet solution. This is very important for comparison with different numerical methods, and even with AMR scheme.

We remind again, that the wave packet test does not include the gravitational potential, and there is no analytical solution to the coupled Schrödinger Poisson system. However, it is essential to test if our scheme can capture the interference pattern during merger events, because some solvers, such as the Madelung solver based on the hydrodynamic equations Eq.2.24, fail to simulate the regions with 0 density. The second test is to simulate a Gaussian wave merger in 1D. As shown in Fig.4.1, the pseudo-spectral code is stable while resolving the constructive and destructive interference pattern.

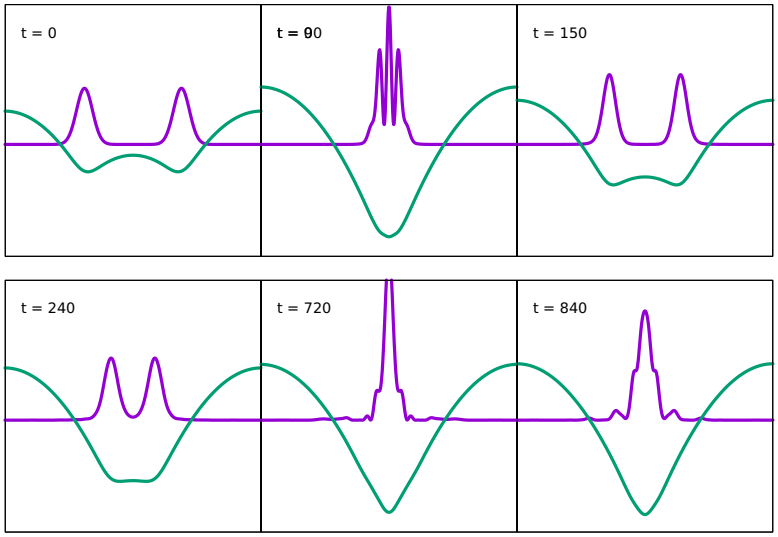

Fig. 4.1. Time evolution of two Gaussian wave merger in 1D by numerically solving the Schrödinger-Poisson Equations using pseudo-spectral method. Purple lines are density and green lines are gravitational potential in dimensionless unit. X-axis is dimensionless position. As the waves merge, interference pattern is created. In the end, the two waves merged into one, and the wave keeps oscillating.

After that, we fully extend our scheme into a 3D cosmological FDM solver. To include the expansion of the Universe in our calculation, we need to integrate the scale factor to obtain the size of the time step Δt while following the CFL condition. The initial condition is obtained through *MUSIC* where the initial redshift is at $z = 50$. We performed both cosmological simulations of FDM and CDM, where the latter is simulated through GADGET-2. Fig.4.2 shows a comparison between the evolution of structure formation of FDM with $mc^2 = 5 \times 10^{-24}$ eV and CDM. Although we expect different dark matter distributions between the models, the idea is to confirm if the structure converges at least on large scale, which is the case here. We can also clearly see how the FDM model indeed suppresses structure formation on a smaller scale due to quantum pressure. In fact, the adopted particle mass $mc^2 = 5 \times 10^{-24}$ eV in this test is already ruled out by CMB observation, so the result of this section does not provide any in-depth analysis of the FDM model, but to verify our implementation of the FDM solver, such as the cosmological units, the time integration of the scale factor, the cloud-in-cloud interpolation of the initial snapshot, etc.

The convergence between CDM and FDM simulation on large scale demonstrates the validity of our FDM solver, but the ultimate test is to compare our solver with existing FDM solver in the community. While we were developing the code, there was still no FDM solver available to the public, but we, fortunately, have a chance to perform a small code comparison project with May & Springel (2021). Our codes are independently developed, but adopted the same pseudo-spectral splitting method in a second order. Again, we adopted the same initial condition, and perform the simulation until $z = 0$. To quantify the simulated dark matter distribution in our snapshots, we measure and compare the power spectrum

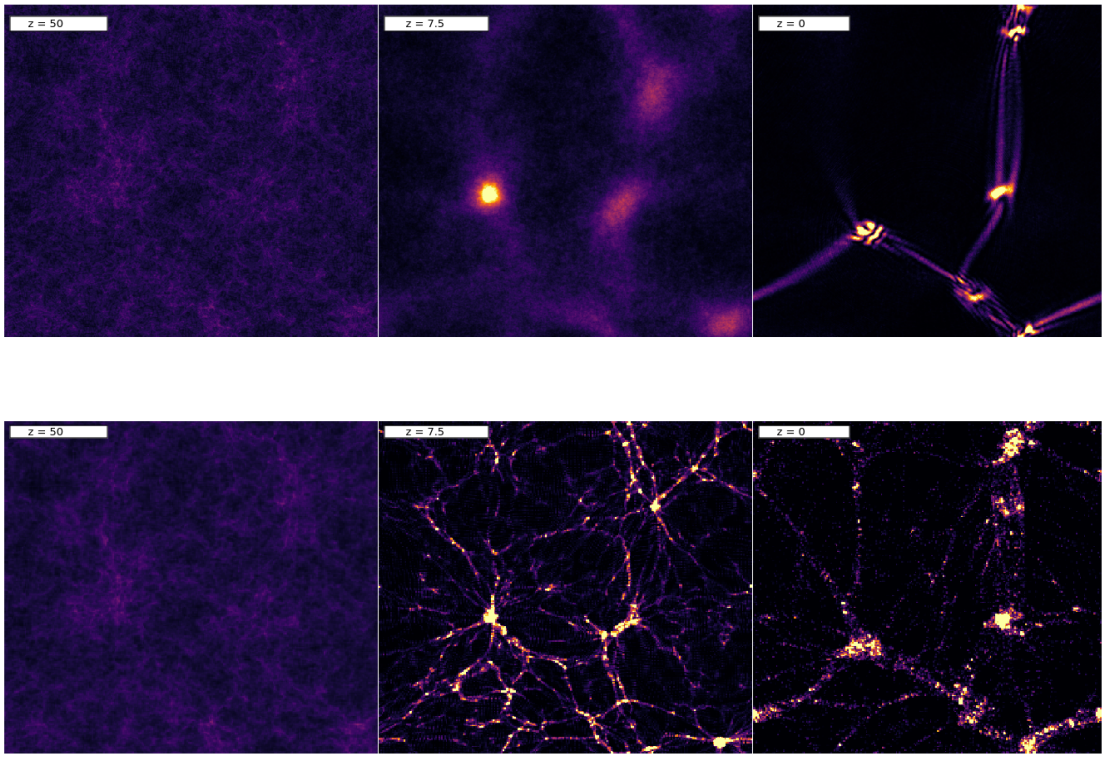

Fig. 4.2. Comparison of slices of cosmological simulations between FDM (top row) and CDM (bottom row) model at redshift $z = 50,\ 7.5$ and 0 with boxsize $L = 10$ Mpc/h. FDM simulation is performed with $mc^2 = 5 \times 10^{-24}$ eV.

$P(k) =< \delta_k^2 >$ as shown in Fig.4.3. It is remarkable how our power spectrum agrees with each other, and how the power spectrum approaches CDM on small k.

4.2 Convergence Tests

The pseudo-spectral solver guarantees the conservation of energy and mass of the wave function. Here we quantitatively shows the convergence of the adopted numerical method, and how energy and mass are conserved within several percent for $N^3 \geq 64^3$. We test the solver by performing soliton merger simulations with 6 solitons following Eq.2.25 with being distributed at $(d, 0, 0), (-d, 0, 0), (0, d, 0), (0, -d, 0), (0, 0, d)$ and $(0, 0, -d)$, where $d =$ 100 kpc. The boxsize is 800 kpc, and the assumed particle mass is $mc^2 = 10^{-23}$ eV. For this particular test, we performed simulations with $N^3 = 64^3$, 128^3, 256^3 and 512^3. The timestep is always chosen to be the largest possible step following the CFL-like condition Eq.4.6.

Fig.4.4 and 4.5 show the percent error for energy and mass respectively. The error becomes less with increasing spatial resolution, showing the convergence of the conservation for both energy and mass. It is interesting to point out that the numerical method does better in the conservation of energy than mass. The sudden rise of error for mass occurs

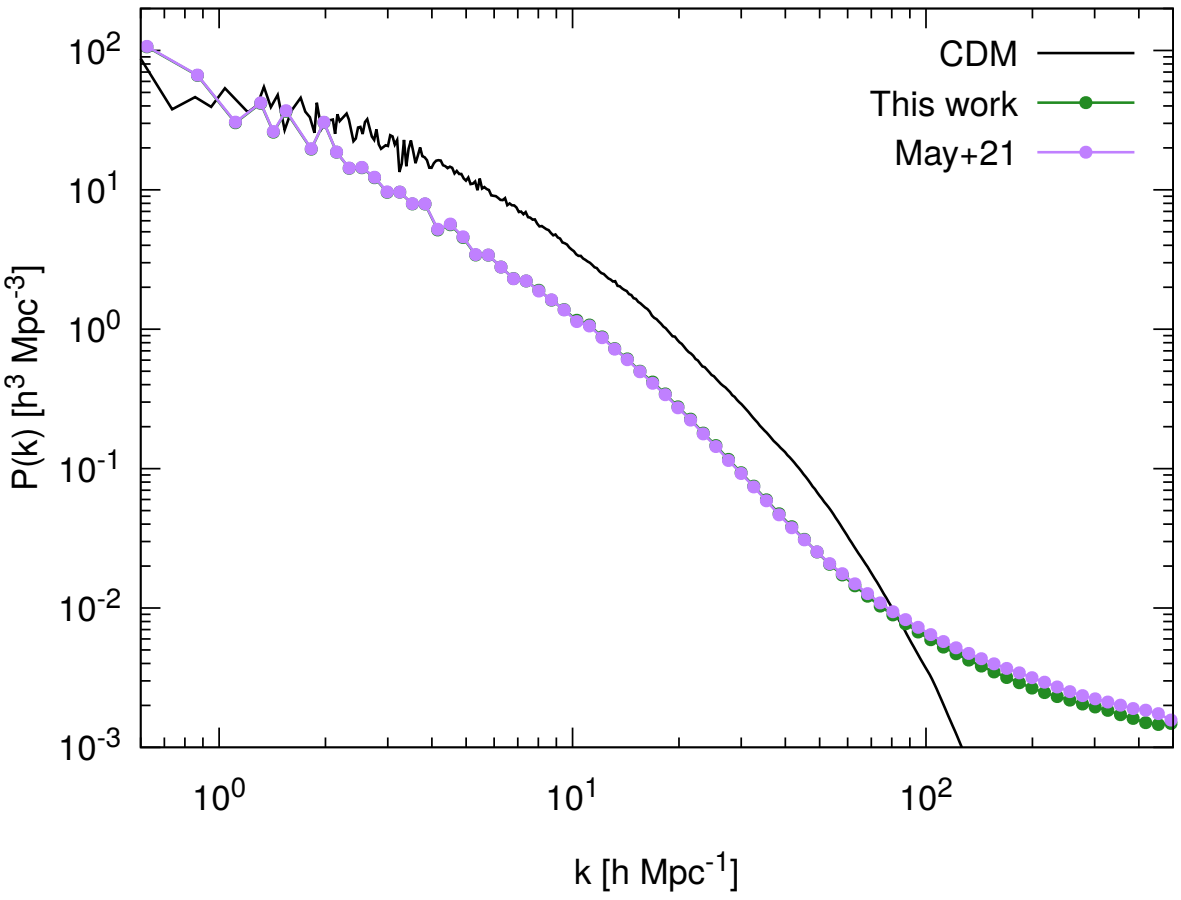

Fig. 4.3. Comparison of the power spectrum at $z = 0$ between the code used in this work and that of May & Springel (2021) for a cosmological test simulation.

during the merging event, but, nevertheless, the percent error for both stay below 3% for simulations with $N^3 \geq 64^3$.

Fig.4.6 shows the density profile of the merged soliton in the simulations. When the spatial resolution is low, it is clear that the core structure is not resolved, and shows a steep rising profile at the center. For this particular core/halo mass, the core structure is perfectly resolved only with $N^3 \geq 256^3$. Fig.4.6 demonstrates the numerical convergence of the density profile with more refined spatial resolution. We remind that if the core size is smaller for heavier core or halo mass, then the core profile will become less resolved.

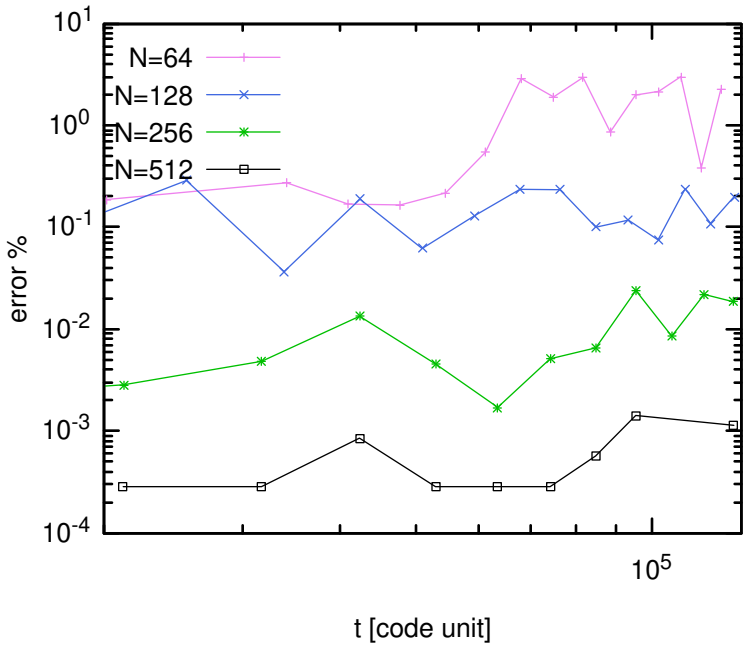

Fig. 4.4. Conservation of energy. Pink, blue, green and black lines are the percent error of the total energy of the snapshot simulated with spatial resolution $N^2 = 64^3$, 128^3 , 256^3 and 512^3 respectively.

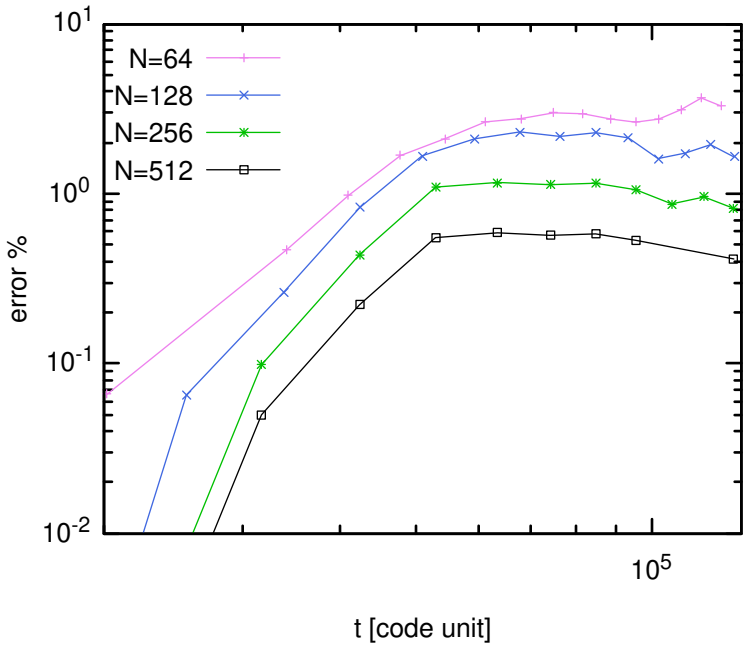

Fig. 4.5. Conservation of mass. Pink, blue, green and black lines are the percent error of the total mass of the snapshots simulated with spatial resolution $N^2 = 64^3$, 128^3 , 256^3 and 512^3 respectively.

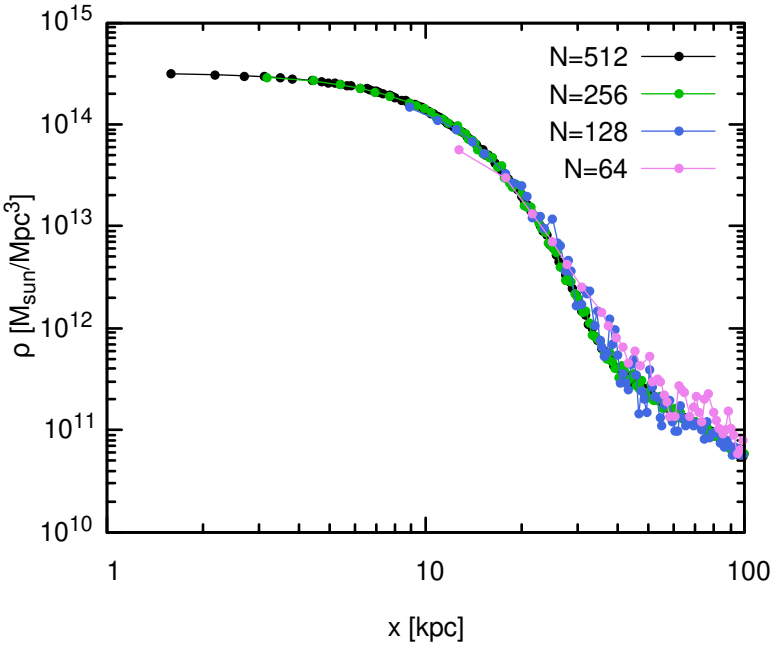

Fig. 4.6. The convergence of the core-halo density profile.

4.3 Current/Upcoming numerical schemes

We remind that Appendix.B.2 has shown a few introductory solvers for the Schrödinger-Poisson system. We will here close the section by reviewing some of the numerical schemes that are still being used in the community.

Starting with Schive et al. (2014b,a) who have adopted the splitting method again but solved the Schrödinger equation by expanding the exponential operator with Taylor expansion until the 3^{rd} order. Schwabe & Niemeyer (2022) developed Axionyx that can combine the efficiency of N-body simulation with the finite-difference solver for the Schrödinger equation on adaptively refined meshes. On the mesh level, they solve the Schödinger equation with a 4^{th} order Runge-Kutta method, and the coupled SP system is solved with a 6^{th} order splitting scheme. Their recent work Schwabe & Niemeyer (2022) claimed to successfully perform a zoom-in simulation to simulate a MW-size FDM halo. We remind, however, that Axionyx does not include the quantum pressure term in the N-body simulation. Another group, Hopkins (2019), made use of the GIZMO code and solved the FDM equations with the finite volume method. He tested the scheme not only on the Schrödinger-Poisson system but also on the Madelung equations and the combination of both. He found a stable way to simulate FDM with the finite volume method, and also made use of the adaptive scheme that was already implemented in GIZMO. Regardless of the method of spatial discretization, since all solvers mentioned above adopted an explicit time stepping scheme, they all suffered from the stringent time-step constraint that scales with the square of the spatial grid size (see Eq.4.6). It is essential to experiment with implicit methods, such as the Crank-Nicolson method, to explore if there is a net gain in the simulation speed. In short, the numerical scheme of FDM simulation is still a developing field, which is essential for studying the non-linear dynamics of the FDM model.

Chapter 5

Diversity of Core-halo structure

This section presents the result published in Chan et al. (2022), for which the author of this thesis was mainly responsible for. The paper was co-authored by Elisa G. M. Ferreira, who performed the statistical analysis and provided theoretical expertise, Simon May, who provided numerical data and support, Masashi Chiba ad Hayashi Kohei, who provided their expertise in a dwarf galaxy. We performed FDM simulations based on the numerical scheme and set up in the previous chapter, collected a large halo catalog. We found a scatter in our resulting core-halo mass relation, which manifests as a diversity in the core-halo structure of the FDM model.

5.1 Setup

In this work, we analyse the properties of haloes from three different sets of simulations:

1) soliton merger simulations
2) cosmological simulations in a small box and
3) a high-resolution large-scale cosmological simulation.

The first two sets of simulations are performed in this work, and the last was performed by May & Springel (2021). All of them used the same numerical scheme, but different initial conditions. We refer the reader to Appendix B.3 for numerical conversion between particle and wave quantity.

5.1.1 Soliton merger simulations

The soliton merger simulations are performed with a particle mass $mc^2 = 10^{-22}$eV, a box size $L = 300$kpc and at $z = 3$ on a grid with $N^3 = 512^3$ cells. The simulations are started with six randomly-placed solitons with mergers mostly occurring at $t \sim 0.1\, t_{\rm H}$, where $t_{\rm H}$ is the Hubble time. Since the simulations at $z = 3$ take 16 times longer than those at $z = 0$ due to the dependence of the time step on the scale factor as shown in 4.6, we stop the simulations at $0.5\ t_{\rm H}$. We have checked that haloes at $t \sim 0.5\, t_{\rm H}$ are relaxed, since they meet the virialisation criterion $|2(K + Q)/W| \approx 1$ (Hui et al., 2017; Mocz et al., 2017) (where K,

Q and W, are the kinetic, quantum and potential energies, respectively). However, we also included unrelaxed haloes in between $0.1\,t_{\rm H} < t < 0.5\,t_{\rm H}$ in our results. Alternative initial settings were tested, such as increasing the number of solitons with a larger range of masses, but the results do not change the main conclusion of this work.

5.1.2 Small-volume cosmological simulations

A series of cosmological simulations are performed using the same resolution, particle mass, and box size. They all begin from $z = 50$ and stop at $z = 0$. The initial conditions are generated using MUSIC (Hahn & Abel, 2011) with the CDM transfer function from Eisenstein & Hu (1998); Eisenstein & Hu (1999), and the following cosmological parameters: $\Omega_m = 0.276$, $\Omega_\Lambda = 0.724$, $h = 0.677$ and $\sigma_8 = 0.8$. Due to the difficulty of simultaneously resolving the large-scale structure and the inner non-linear evolution of haloes on a grid size of 512^3, we use initial conditions that correspond to zoom-in regions with $L = 300$kpc of a larger 1 Mpc box generated by MUSIC with different random seeds.

5.1.3 Large-volume cosmological simulation

A large-volume high-resolution cosmological simulation was performed by May & Springel (2021) with similar cosmological parameters, but larger box size $L = 10$ Mpc$/h$ and grid size $N^3 = 8640^3$, and slightly lighter particle mass $mc^2 = 7 \times 10^{-23}$eV. With such a box size and spatial resolution, this simulation contains a population of haloes with diverse formation histories, including tidally stripped, isolated, and merged haloes. Therefore, it provided us with a more realistic measurement of the core–halo mass relation in a fuzzy dark matter (FDM) universe. Fig.5.1 visually shows the time evolution of the density distribution in different simulations. It is clear that, whether a halo is formed through soliton mergers or gravitational collapse of large-scale structure, there always exists a stable core structure enveloped by interference fluctuations within its host halo, but we will see later that different box sizes can lead to different types of core–halo structure.

5.1.4 Initial power spectrum

As noted above, in this work (as well as May & Springel, 2021), we did not use the initial power spectrum of the FDM model, which presents a suppression of power on small scales, because the inner structure of haloes is insensitive to the initial conditions. Simulated haloes with comparable size of the soliton are rare if a more realistic power spectrum is applied, but should still exist and therefore be included in the resulting core–halo mass relation.

5.1.5 Spatial resolution

Our soliton merger simulations have a smaller box size, but the same number of grid cells (512^3) as our cosmological simulations, so the resolution $\Delta x = 0.644$ kpc is better than previous studies (Schwabe et al., 2016; Mocz et al., 2017). This allows us to resolve smaller cores, but the haloes may experience stripping effects from their own gravitational pull. On the other hand, although the large simulation is performed in high resolution, the

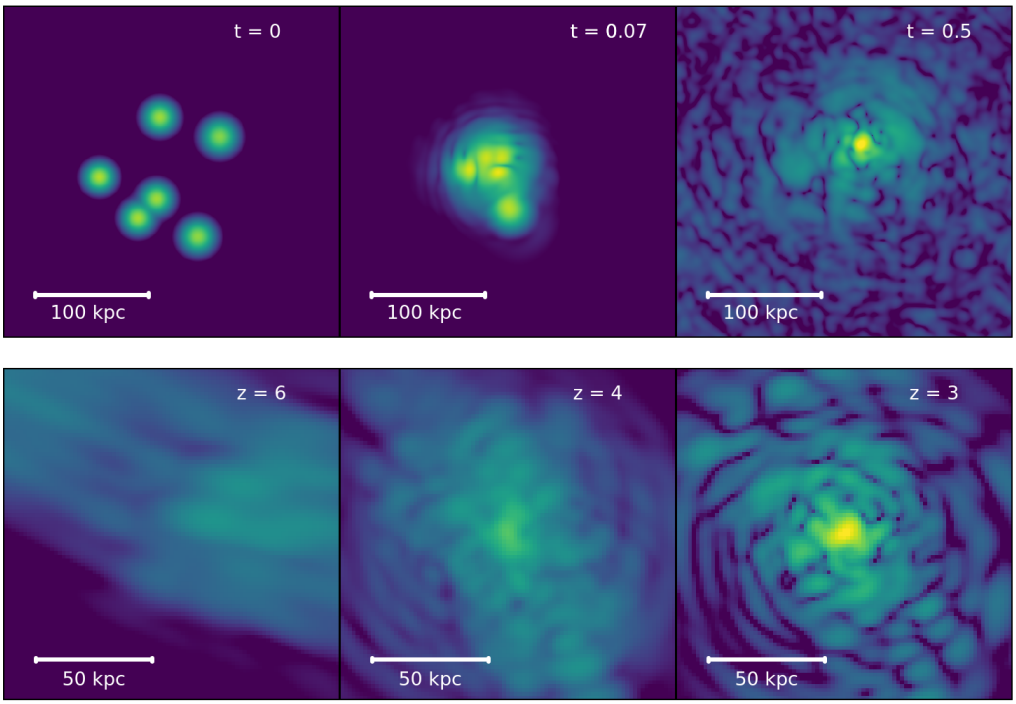

Fig. 5.1. Time evolution of core and halo. The top row shows an example of a soliton merger simulation at $z = 3$ in a box of size 300kpc with particle mass $mc^2 = 10^{-22}$eV. The bottom row shows a selected halo formation from the large-scale structure simulations by May & Springel (2021). A stable core–halo structure can always be found at the end of all simulations. For illustrative purposes, the first two columns are projected density, but the last column is a slice of the snapshot.

(re-scaled) grid resolution $\Delta x = 1.547$ kpc is still twice as large as that of the soliton merger simulations. The importance of resolving the core with fine enough grids is reflected in the core mass–radius relation. Fig.5.2 shows that simulated haloes have cores following a tight relation:

$$a^{1/2} M_{\rm c} = \frac{5.5 \times 10^9}{(mc^2/10^{-23}{\rm eV})^2 (a^{1/2} r_{\rm c}/\ kpc)} \,. \tag{5.1}$$

As the core becomes more massive, the core size decreases further. When the core size is resolved by less than two grid cell lengths, the relation becomes more dispersed and discretised.

5.2 Density profiles

The centres of the haloes from the simulations performed in this work are found by the minimum gravitational potential, and those from the cosmological simulation in May & Springel (2021) are determined by selecting the densest cells of haloes found by a grid-based

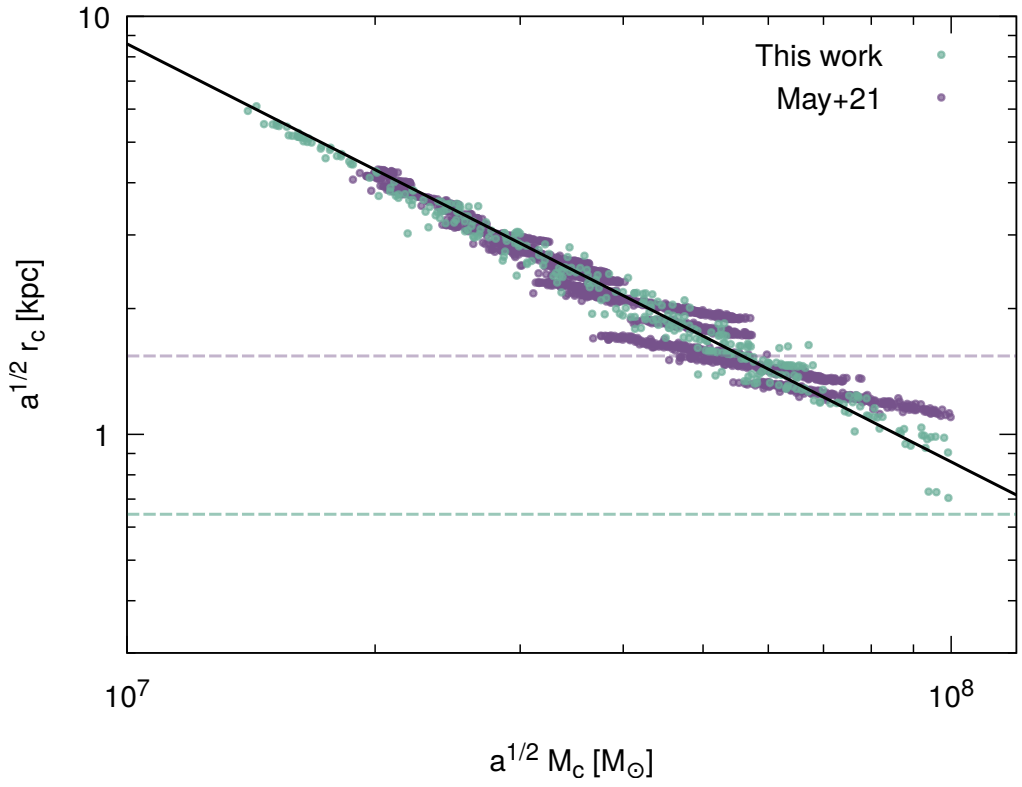

Fig. 5.2. Core mass–radius relation scaled to $mc^2 = 8 \times 10^{-23}$ eV via Eq.2.18. The black line is a fitting relation Eq.5.1 from Schive et al. (2014a). The dashed lines show $2\Delta x$ as a reference of the resolution limit for the simulations of this work and May & Springel (2021).

friends-of-friends-like halo finder. We measured the spherically averaged density profile and performed fitting to Eq.2.28 to extract r_c, r_t and r_s for all haloes. As shown in Fig.5.3, a flat cored structure is identified towards the center in all profiles. They are well fitted by the core density profile Eq.2.28 with a maximum error of 10% up to the core radius r_c. After the transition radius r_t, the profiles follow the Navarro–Frenk–White (NFW) profile. We also see that for some haloes, we have a direct transition from the core to the NFW profile, while others show a longer transition with an intermediate behavior linking the two regimes.

One interesting feature we observe is oscillations in these profiles in their outer regions that can only be modeled on average by the smooth NFW profile. A possible reason for the fluctuations is that they are caused by the interference granules in the NFW region. If this is true, it is possible that halo density profiles can be used to measure this unique interference pattern present in models like FDM. More tests are needed to confirm this hypothesis.

In previous simulations (Schive et al., 2014b; Mocz et al., 2017), the transition radius was found to be $r_t \geq 3r_c$, where the residual error between the data and the core profile is less than 2% for $r < r_t$. However, our measured r_t, purely from fitting to the cored NFW profile Eq.2.28, disagrees with these previous results. The error at $3r_c$ is greater than at least 10%, as shown in the bottom panel of Fig.5.3, meaning the actual r_t should be located at a radius smaller than $3r_c$. The range of values for the measured r_t in Fig.5.4 shows that most haloes do have $r_t \leq 3r_c$. Other recent work, such as Yavetz et al. (2021), also shows smaller transition radii, e. g. $r_t \approx 2r_c$. As mentioned before, from theory, to guarantee a continuous and smooth transition from the solitonic core to the NFW profile, continuity of both the density and of its first derivative would be necessary, which translates to the requirement $r_t \leq 3r_c$, which, therefore, agrees with our result. This implies that all the haloes in the simulations presented here have a continuous and smooth transition from the core to the NFW profile, with or without a transition period, and thus do not suffer from the apparent inconsistency present in previous simulations.

5.3 The core–halo mass relation

Fig.5.5 shows the core–halo mass relation obtained from the soliton merger and cosmological simulations. All data are scaled to $mc^2 = 8 \times 10^{-23}$eV using Eq.2.18 in order to enable a direct comparison with the data and fitting relation from Schive et al. (2014b). For reference, we also show the core–halo mass relation of a soliton-only profile, i.e. a pure core profile with $r_t \to \infty$ in Eq.2.28, represented by the solid black line. This curve indicates the minimum halo mass for a certain core mass, and any haloes located to the right of the soliton-only core–halo relation must have the usual cored NFW structure. For haloes in the soliton merger simulations with mass $\gtrsim 10^8 M_\odot$, the relation has a steeper slope than $\alpha = 1/3$, confirming the results from Mocz et al. (2017). However, haloes from the large-scale cosmological simulation predict a core–halo relation with a large enough dispersion that can cover a range of data produced by both the soliton merger simulations and Schive et al. (2014b). The range of the dispersion can span as large as one order of magnitude in halo mass for $M_c \sim 5 \times 10^7 M_\odot$. This dispersion, which fills in the space in between the soliton-only line and the relation from Schive et al. (2014b), indicates the diversity of the cored NFW structure in the FDM simulations. For example, Fig.5.3 highlights two profiles of

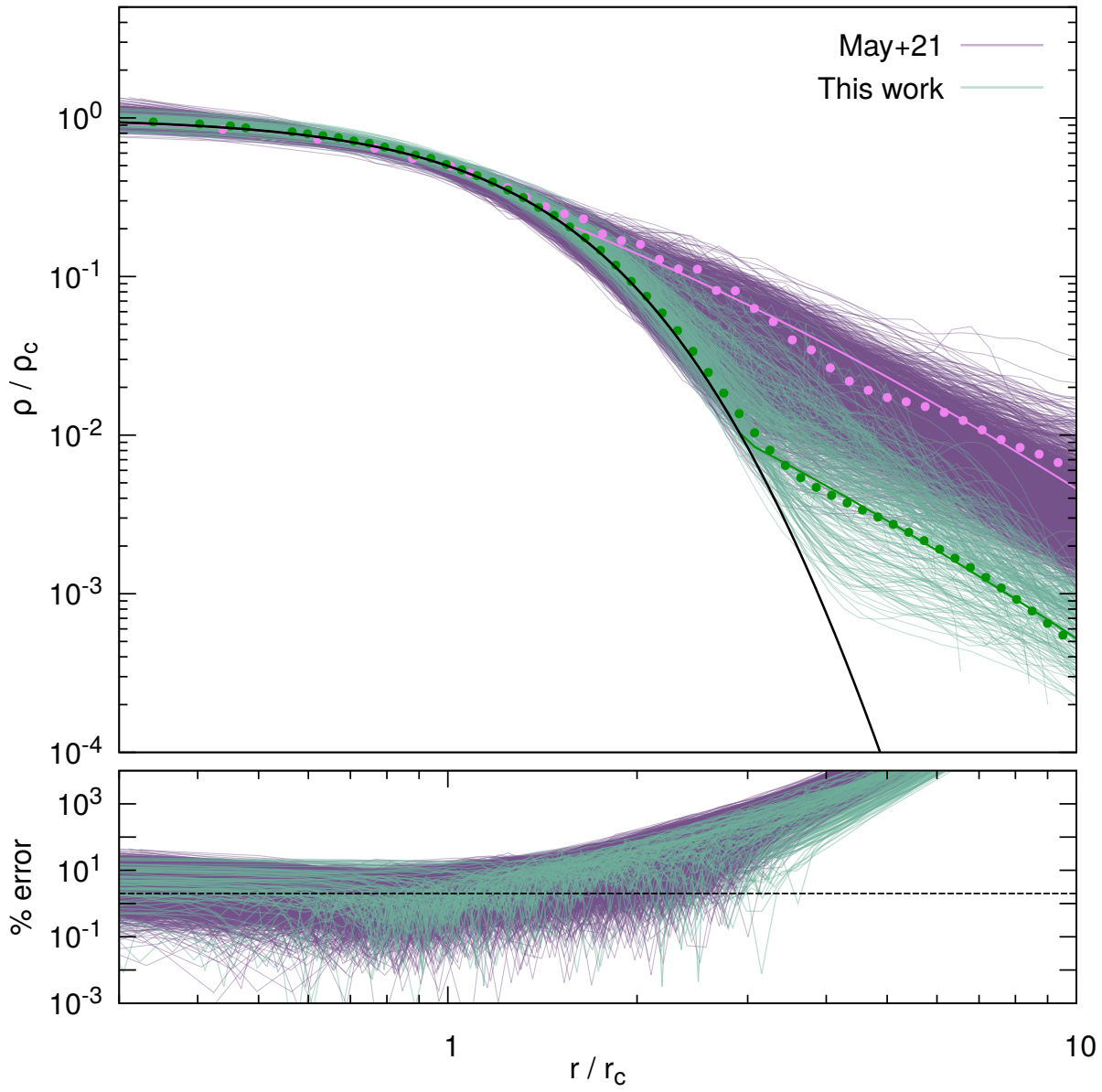

Fig. 5.3. Scaled density profile of haloes obtained from simulations of this work and May & Springel (2021). The scaled core profile is shown as black line. We highlight two haloes with pink and dark green and their best-fit cored NFW profile. They have similar core mass, but an order of magnitude difference in the halo mass. The bottom sub-panel shows the percentage error between data and core profile. The dashed line denotes an error of 2%.

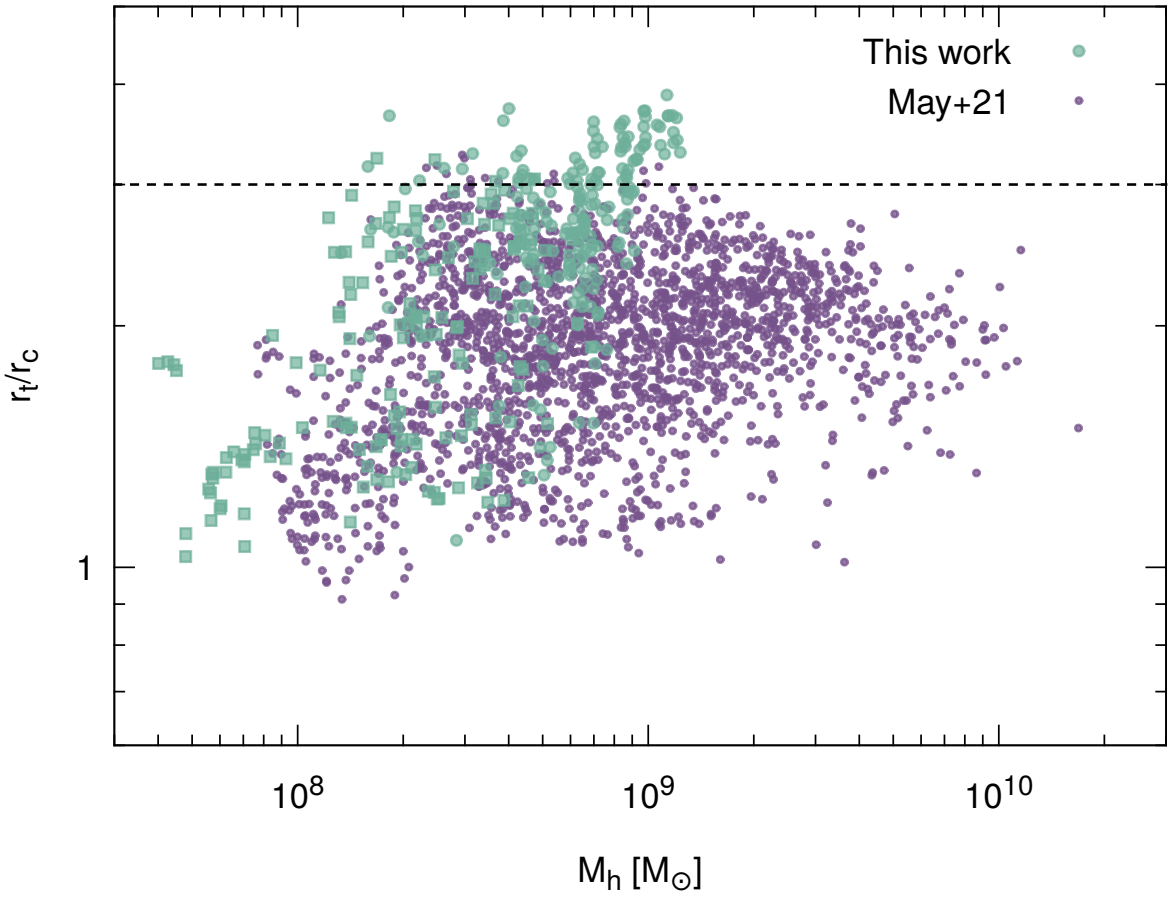

Fig. 5.4. Range of transition radius as a function of halo mass. The dashed line shows the typical transition $r_\mathrm{t} = 3r_\mathrm{c}$ obtained from Schive et al. (2014b).

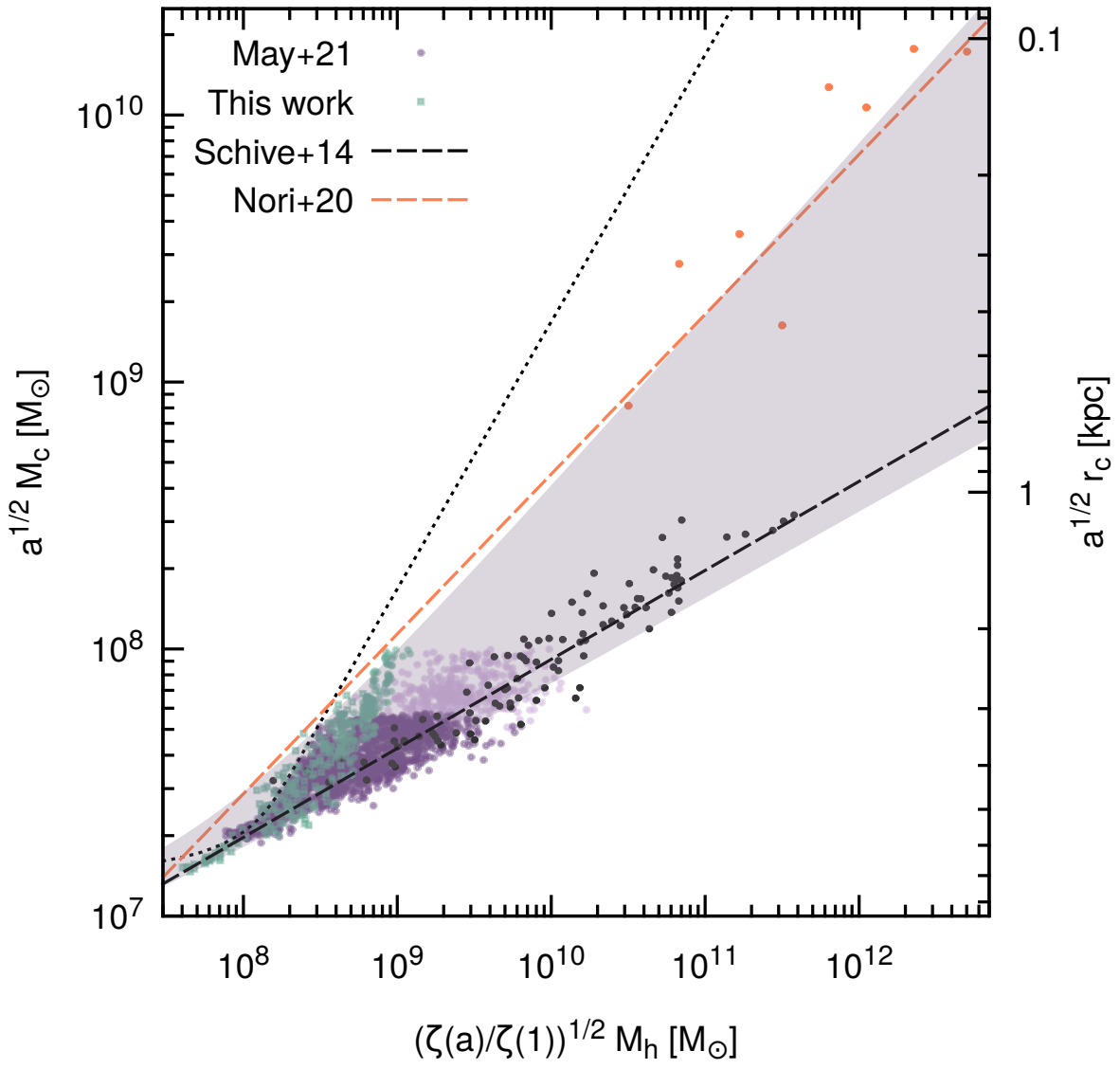

Fig. 5.5. Core–halo relation scaled to $mc^2 = 8 \times 10^{-23}$eV via Eq.2.18. Green dots are haloes simulated in this work with cores resolved by at least $3\Delta x$. Purple and faint purple dots are haloes from the large-box cosmological simulation (May & Springel, 2021) with cores resolved by at least $2\Delta x$ and Δx respectively. The pink shaded region is enclosed by the empirical fits to the purple and green dots, with the maximum and minimum values of the parameters in Eq.2.31. The solid dotted line corresponds to the soliton-only relation obtained from a pure core profile. The black and orange dashed lines are fitting relations corresponding to the black and orange dots obtained from Schive et al. (2014b) and Nori & Baldi (2021)[1]respectively.

haloes with similar core mass $M_c \sim 5\times10^7 M_\odot$, but different halo mass. The tight one-to-one core–halo relations found by different groups, with different slopes, therefore only describe a part, but not all populations of haloes in the FDM model.

We suggest an empirical equation that has the following form: $M_c = \beta + (M_h/\gamma)^\alpha$. The parameter β takes the limit of the relation for small halo masses into account, although low-mass haloes are rare in a FDM universe due to the suppression in the initial power spectrum. α is the slope that can be compared to previous works. After including the scaling symmetry in Eq.2.18 and the redshift dependence according to Schive et al. (2014b), we have

$$\begin{aligned} a^{1/2} M_c = \beta \left(\frac{mc^2}{8\times10^{-23}\mathrm{eV}}\right)^{-3/2} \\ + \left(\sqrt{\frac{\zeta(z)}{\zeta(0)}}\frac{M_h}{\gamma}\right)^{\alpha} \left(\frac{mc^2}{8\times10^{-23}\mathrm{eV}}\right)^{3(\alpha-1)/2} M_\odot\,. \end{aligned} \tag{5.2}$$

The best-fit parameters for the haloes from the large-box cosmological simulation give $\beta = 8.00^{+0.52}_{-6.00}\times10^6\,M_\odot, \log_{10}(\gamma/M_\odot) = -5.73^{+2.38}_{-8.38}$ and $\alpha = 0.515^{+0.130}_{-0.189}$, which is shown as a pink shaded region in Fig.5.5.

The effect of the large dispersion is encompassed in the uncertainty of the model parameters. This uncertainty is not the statistical uncertainty of the fit, but an "overestimation" of the uncertainty in the parameters that can reflect the large dispersion of the data. Indeed, the statistical uncertainty would be the incorrect quantity to consider in this case, since we do not assume that there is an underlying true set of values for the parameters with statistical fluctuations, but rather propose that different halo populations could *systematically* follow different relations depending on their histories and properties (see Chap.5.3.1). To obtain a more appropriate description of the core–halo diversity, we employed kernel density estimation (KDE), estimating the probability distribution function of the core masses with respect to the central value of the corresponding binned halo mass. Each of these distributions reveals the dispersion of core masses for each halo mass.[2] We then obtain the minimum and maximum curves $M_c(M_h)$ that fit all of these distributions, and extract the minimum and maximum values for the parameters b, γ and α from these curves. The difference in the global fit is our uncertainty in the parameters.

Nori & Baldi (2021); Mocz et al. (2017); Schive et al. (2014b) determined slopes α of 0.6, 0.556, and 0.333, respectively. Given the large dispersion seen in our data, all of these slopes are compatible when taking into account the uncertainty we assigned to the fitting parameters. So when considering the fitting function we propose, all of the other cases in the literature are covered as well. We emphasize that our results show that a general halo population is not well-described by any single one-to-one core–halo mass relation. Further investigation is required to determine which halo populations follow which relations (if any), and under what conditions – cf. Chap.5.3.1.

This large spread and uncertainty in the fitting function can affect the constraints on the FDM mass obtained from these relations. Here, we provide a rough estimate of the error. For the same halo mass $M_h = 10^9 M_\odot$ in Fig.5.5, we can have the least massive core mass as $M_c =$

[1] We adopted parameters resulting from the varying exponents analysis without sub-sampling restrictions.
[2] We can provide the distribution of core masses for each halo mass bin by request for those interested.

$3 \times 10^7 \mathrm{M}_\odot$ and the most massive as $M_\mathrm{c} = 10^8 \mathrm{M}_\odot$. Applying these values to the core density in Eq.2.28 gives a 50% difference in particle mass m. Therefore, any observational constraints made using the relation Eq.2.31 should include an additional uncertainty on the order of 50% in the results, unless the halo mass is smaller than $10^9 (8 \times 10^{-23} \mathrm{eV}/(mc^2))^{3/2}\,\mathrm{M}_\odot$. Therefore, when obtaining the FDM mass using the core–halo relation, one needs to take into account the dispersion of these values, shown in the uncertainty in the fitting parameters, which will translate to higher uncertainty in the FDM mass.

We now scrutinize whether the scatter of the core–halo relation has an influence on the FDM mass constraints through a dynamical analysis for dwarf galaxies, as has been performed in the literature when fitting the presence of a core in such galaxies. To this end, we apply the spherical Jeans analysis to the kinematic data of the Fornax dwarf spheroidal galaxy, which has the largest data set among the Galactic dwarf satellites. We perform the Jeans analysis[3] using two different core–halo relations, which are suggested by Schive et al. (2014b) and this work, and then we map the posterior probability distributions of the FDM mass through the Markov Chain Monte Carlo (MCMC) technique based on Bayesian statistics. Comparing the posteriors, there is no clear difference in the shape of those distributions, including that of FDM mass, but this is due to the fact that there exists a degeneracy between halo mass and FDM mass. Therefore, this degeneracy makes it hard to see the impact that the core–halo relation has in the Jeans analysis.

Due to limited spatial resolution, we could only observe the dispersion to increase with halo mass until $M_\mathrm{c} \sim 6 \times 10^7 \mathrm{M}_\odot$. It would be important for potential future higher-resolution simulations to examine if the dispersion keeps increasing along the soliton-only relation or not. Again, the increasing dispersion is of importance to observational studies since it will also lead to an increasing uncertainty in the core–halo relation.

5.3.1 The origin of the dispersion

Different core–halo structures have been found in different simulations:

- As mentioned before, Schive et al. (2014b) and Mocz et al. (2017) find different results for the slope α (1/3 vs. 5/9), even for similar simulation setups (soliton mergers).
- Mina et al. (2020) claim to confirm a slope of $\alpha = 5/9$, as found in the soliton merger simulations of Mocz et al. (2017), but using a *cosmological* simulation, contradicting the result of $\alpha = 1/3$ from Schive et al. (2014b). However, the number of haloes in their sample is very small.
- Schwabe et al. (2016) performed soliton merger simulations similar to Schive et al. (2014b) (and later Mocz et al., 2017)[4] and could not reproduce the previously-found value of the slope α, or indeed any universal relation.

[3]For the dynamical analysis we adopt in this work, the interested reader may find further details in Hayashi et al. (2021).

[4]Although Schwabe et al. (2016) made use of sponge boundary conditions instead of periodic boundary conditions.

- Nori & Baldi (2021) studied the dynamics of eight simulated haloes and concluded with a similar comment: Schive et al. (2014b) and Mocz et al. (2017) only captured a partial representation of the core–halo relation in a realistic cosmological sample.

- Yavetz et al. (2021) used the Schwarzschild method to construct self-consistent FDM halos and found that a stable core–halo structure can exist even when the adopted core–halo mass relation deviates from Schive et al. (2014b).

These examples illustrate that the diversity of the possible core–halo slopes found in different works seems to originate from the type of simulations performed, which results in halos and cores that have different properties. The diversity of core–halo structure found in these simulations is exhibited in our work, where we can clearly see the difference between the core–halo mass relation from halos formed in soliton merger simulations (green points in Fig.5.5) and in cosmological simulations (pink points in Fig.5.5).

We can think of a few possible explanations for this diversity of halos: merger history (Du et al., 2017; Yavetz et al., 2021), tidal effects, and the relaxation state of the halo (Nori & Baldi, 2021). Formation and merger history is an explanation that seems very plausible to be a relevant factor. Larger cosmological simulations, like the one from May & Springel (2021), present halos that could have very different merger histories, and a large dispersion is expected. This is different from the soliton merger simulations, where we do not expect a complicated merger history. We leave for future work to try to identify the different merger histories and try to clarify how this relates to the different incarnations of the core–halo mass relation.

Another possible factor that can also contribute to the dispersion found is a tidal effect. There are two different scales of tidal effects can come into play: the tidal stripping effect on the subhaloes, and the environmental tidal effect by the LSS. Here, we will attempt to provide an argument to support the former as one element responsible for the dispersion, based on the setups of various simulations. By comparing the box sizes and the resulting slopes α between the small-volume cosmological simulations of this work with Mocz et al. (2017) and Schive et al. (2014b), which are $335, 1765, \geq 2000$ kpc (box sizes) after re-scaling via Eq.2.18, and $\sim 0.9; 0.556; 0.333$ (slopes) respectively, we find that smaller simulation box sizes are correlated with a steeper slope in the core–halo relation. This can be explained by the stripping effect on the halo by its own gravity due to the periodic boundary conditions: the self-stripping effect becomes more effective at removing mass from the NFW region as the box size decreases. This skews the core–halo structure towards smaller halo masses, steepening the core–halo relation. A more rigorous test to prove the above argument requires simulations with increased spatial resolution and box sizes up to at least 2 Mpc, which current numerical schemes are unable to feasibly achieve.

The self-stripping effect is a numerical artifact, but there is no doubt that a stable core–halo structure can exist within such environments. In more realistic cosmological simulations, dwarf satellites also experience a similar effect from their host haloes in the form of tidal stripping. Therefore, we suggest that stripping effects by tidal forces are one of the contributing factors causing the dispersion obtained from the large-box simulation in May & Springel (2021). One subtlety is that the tidal effect is an interaction between host haloes and sub-haloes with at least two orders of magnitude difference in mass, but the halo finder

used in May & Springel (2021) does not identify sub-haloes. However, it is known that sub-haloes in cold dark matter (CDM) simulations can temporarily move outside of the virial radius of the host halo after the first pericentric passage (van den Bosch, 2017). We assume that ejected sub-haloes should also exist in a FDM cosmology, and therefore identified by the halo finder.

Despite the tidal stripping effect could be weak in the isolated simulations, the environmental effect from the LSS in principle can decrease the density of haloes in the cosmological simulations. For instance, the cosmological haloes (see Fig.5.3) are denser in the NFW region than the isolated haloes. Since the profiles are normalized by the core density, the difference between them could be explained by the tidal force that pulls the inner mass to the outer NFW region of the halo in the cosmological simulation.

An in-depth analysis of the tidal effect on the core–halo relation, or FDM sub-haloes in general, would require building merger trees, which is still not yet studied in any FDM cosmological simulations. We leave this investigation to future work.

5.4 Other relations: Core radius–halo mass relation

As suggested by Burkert (2020), the FDM model may fail to explain the observed trend of the core radius–halo mass relation measured from dwarf galaxies. We follow Mina et al. (2020) and present the core radius–halo mass relation measured from our FDM halo samples. As shown in Fig.5.6, the scatter is still observed, but the decreasing trend, which is a fundamental property of quantum pressure-induced cores, is in disagreement with the positive scaling predicted by low surface brightness (LSB) galaxies (Salucci et al., 2007; Di Paolo et al., 2019).

The disagreement is expected because the negative scaling, where less massive galaxies are cored, allows the FDM model to solve the core–cusp problem, but the relation from LSB galaxies has the opposite behavior, where massive galaxies have larger cores. In addition, LSB galaxies are predicted in CDM simulations to have experienced tidal heating and supernova feedback (Martin et al., 2019). Therefore, the relation between core radius and halo mass poses a challenge to the FDM model, but more importantly, it motivates future FDM simulations to include baryonic physics to verify if LSB-like galaxies can be formed or not.

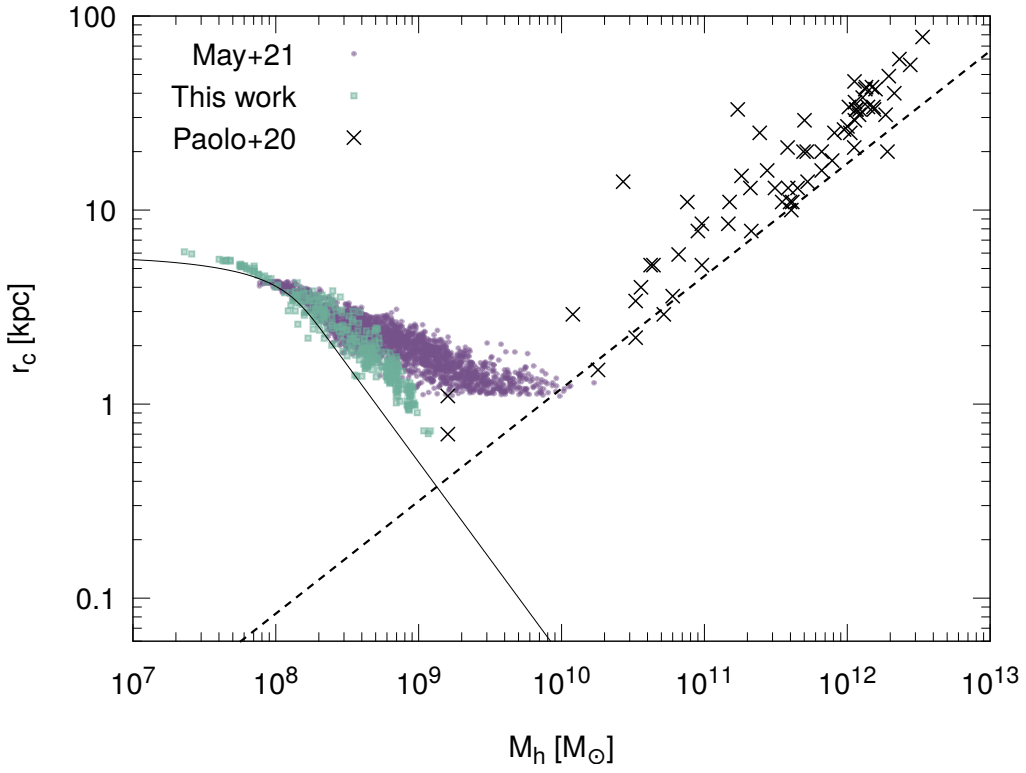

Fig. 5.6. Core radius vs. halo mass. Green and purple points are properties of haloes from simulations of this work and May & Springel (2021). The black line shows the relation predicted by a soliton-only density profile. The dashed line is an empirical function predicted by LSB galaxies (Salucci et al., 2007). Black crosses are from Di Paolo et al. (2019).

Chapter 6

Future Prospect

In this thesis, we discovered the diversity of halo in the FDM model through numerical simulations and it is now important to investigate the observational consequences of the diversity. As discussed, there indeed exists a diversity problem with dwarf galaxies, meaning the rotation curve and density profile are too diverse to be explained by the ΛCDM model, even including the consideration of baryonic component Oman et al. (2015); Hayashi et al. (2020). It will be interesting to test if the diversity in the core-halo structure helps solve the diversity problem in the dwarfs. However, Hayashi et al. (2020) adopted Jeans analysis and it is not well known how we include the scatter into the MCMC-based Jeans analysis. Moreover, Oman et al. (2015) included low surface brightness galaxies in their samples, which are known to be created through baryonic physics. Instead, we can look at the circular velocity of field dwarf galaxies, which have been studied by Robles et al. (2019), because field dwarfs are small enough to have inefficient baryonic feedback, but also far enough from the host to be unaffected by tidal effect. In fact, there also exists a scatter in the circular velocity that is not mentioned in the work of Robles et al. (2019). As one of our future works (see Fig.6.1), we model the core-halo structure at z=0 by including the scatter in the core-halo mass relation and directly compare it with the circular velocities of the observed field dwarf galaxies.

Observationally, we expect The Subaru Prime Focus Spectrograph (PFS), as an upcoming spectroscopic survey, to provide the sample sizes and velocity precisions required to determine whether the dwarf density profiles are more consistent with ΛCDM or FDM model in the future. The Galactic Archaeology Program of PFS has targeted six dwarf spheroidals: Boötes I, Draco, Ursa Minor, Sextans, Sculptor, and Fornax. Two different analysis techniques are proposed to independently determine the inner slope of the targeted dwarf galaxies, which will allow us to distinguish between core formation by baryonic feedback or dark matter physics, such as quantum pressure (PFS Collaboration, in prep.).

Our second future work is to improve the numerical solver for the Schrödinger-Poisson system. Since the time step is mostly limited by the Schrödinger solver $\partial_t \psi = \nabla^2 \psi$, the question is how we could overcome the CFL-like condition $\Delta t \propto \Delta x^2$. Since most Schrödinger-Poisson solvers, at least in the astrophysics community, adopted an explicit method, it is essential to test if the implicit method can allow larger time steps. We propose solving the 3D Schrödinger solver with the Crank-Nicolson method, which is implicit and norm preserving. However, we remind that implicit methods are computationally more expensive to solve at

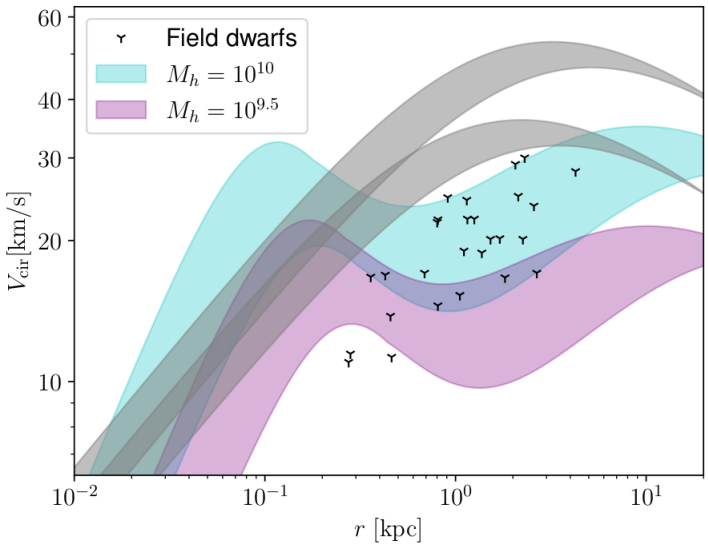

Fig. 6.1. Circular velocity of haloes. Purple and cyan shade are FDM halo model with $mc^2 = 10^{-21}$ eV based on Robles et al. (2019) but with an additional $\pm 25\%$ scatter in the core-halo mass relation Eq.2.31. Data points are circular velocity of field dwarf galaxies at the half-light radius. Grey shades are CDM haloes with an ± 0.1 scatter in the concentration-mass relation for NFW profile, which demonstrates the Too-Big-To-Fail problem.

each time step, so the main idea is to test if the implicit solver can outperform the explicit solver with a larger time step even if it suffered from higher computational cost. We remind that there exists a higher-order Crank-Nicolson method that can help improving the efficiency (van Dijk et al., 2011). Fig.6.2 shows the error of the Schrödinger solver based on the explicit method in the GAMER code (Schive et al., 2014a), the Crank-Niclson method, and higher order Crank-Nicolson method. Although the code development is still in progress, at this stage, we can already see the advantage of using Crank-Nicolson in Fig.6.2. The explicit method becomes unstable quickly for large time steps, but for the high order method, the time step could be an order of magnitude larger than the explicit method.

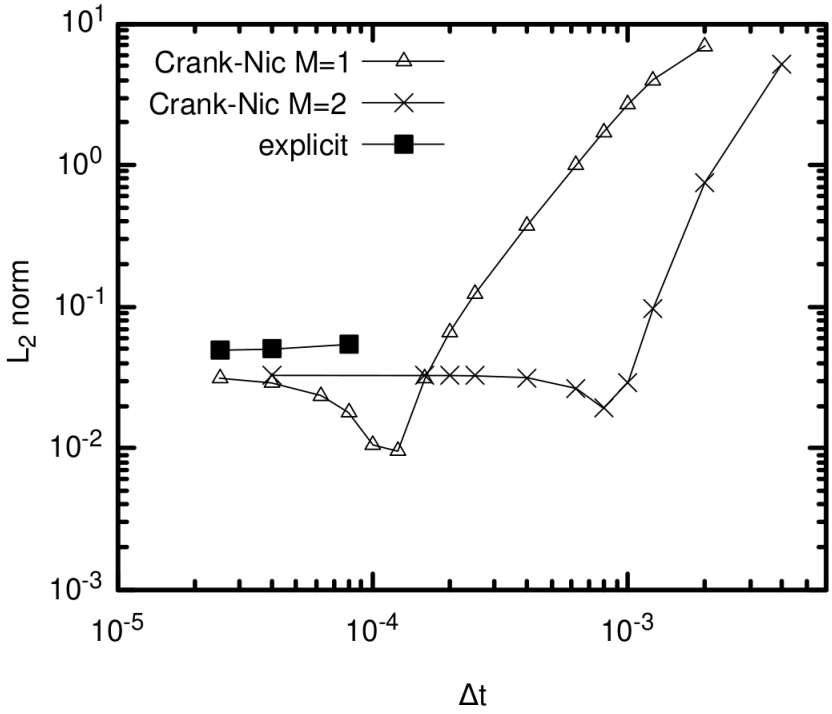

Fig. 6.2. Comparison of numerical error between explicit and Crank-Niclson methods. $M = 1$ corresponds to the standard, whereas $M = 2$ is the higher order version of Crank-Nicolson method. Error is obtained by comparing with the analytical solution of the 3D Gaussian wave packet in Chapter.4.1.

Chapter 7

Conclusion

Solitonic cores are found to be formed in simulations of the FDM model as a consequence of gravity and the uncertainty principle, but there is still no consensus on a single universal scaling relation that describes the relationship between a halo's mass and that of its core, or that one even exists. In this work, we performed new soliton merger simulations and used data from a large-scale cosmological FDM simulation. All simulations are evolved by solving the Schrödinger–Poisson equations through the pseudo-spectral method, which can capture wave phenomena completely. Here is a summary of our findings in this thesis.

We found an agreement between the measured density profiles and a cored NFW profile, but the transition radii of most of the haloes are located at $\leq 3r_c$. This is in disagreement with previous simulations (Schive et al., 2014b; Mocz et al., 2017), but more consistent with the analytical requirement where the transition between the inner core and the outer NFW profile must be continuous and smooth.

The resulting core–halo mass relation, obtained from both soliton merger and cosmological simulations, shows an increasing dispersion with halo mass. The spread extends all the way from the limit of a pure soliton profile to that of Schive et al. (2014b), signifying the diversity in core–halo structure. We suggest that, for small cosmological simulations, artificial stripping effects due to periodic boundary conditions could partially be responsible for the variety of slopes in the relation predicted by different simulations. However, "natural" tidal stripping effects of various severity also exist in larger simulations, which therefore exhibit a greater spread in the relation. Further, the exact impact of variations between individual haloes on the relation, such as merger history or relaxation state, remains to be uncovered.

We provided a new empirical equation that considers the non-linearity in the low-mass end, but we emphasise that any core–halo relation must suffer from an uncertainty produced by the diversity demonstrated in this work. Therefore, observational analyses that adopted a core–halo relation must take into account this uncertainty in the fitting parameters, including the particle mass of the FDM model.

Due to the limited spatial resolution imposed by the time step criteria, our samples still do not represent the full population of core–halo structure. To obtain this, simulations using a more flexible numerical scheme, such as adaptive mesh refinement (Schive et al., 2014a; Mina et al., 2020), and sub-halo catalogs from merger trees would be needed. Such future work would verify whether the dispersion keeps growing beyond halo masses of $10^9(8 \times 10^{-23}\ \mathrm{eV}/(mc^2))^{3/2}\,\mathrm{M}_\odot$, or whether the tidally stripped sub-haloes can explain the

observed diversity in the inner slope–halo mass relation. We also plan future to understand the merger history of the halos we have in the cosmological simulation, using the same techniques as for CDM, in order to try to understand how halos with different merger histories influence the core–halo mass relation.

Lastly, including baryonic physics will further complicate the core–halo structure because the core can now not only be induced by quantum pressure, but also by stellar feedback physics, not to mention the question of how these processes would interact. However, only baryonic physics has a chance of matching the core radius–halo mass relation of LSB galaxies with FDM.

Appendix A

Equation of motions

A.1 Homogeneous scalar field

The calculation starts by assuming the Lagrangian density of a scalar field dark matter to the following form

$$\mathcal{L} = \sqrt{-g}\left[\frac{1}{2}g^{\mu\nu}\partial_\mu\phi\partial_\nu\phi - V(\phi)\right]$$

where $g^{\mu\nu}$ is the metric, $\sqrt{-g}$ is the determinant, and ϕ is the scalar field. $V(\phi)$ is a potential that can be approximated by the Taylor expansion

$$V(\phi) = \frac{1}{2}m^2\phi^2 + \frac{g_{\rm int}}{4!}\phi^4 + \cdots,$$

where the first and second term are the mass term and interaction term respectively. For the FDM model, we consider only the mass term, which means a free field that only has one parameter, the particle mass m without interaction. We consider the homogeneous Friedman-Robertson-Walker metric

$$g^{\mu\nu} = \begin{bmatrix} -1 & 0 & 0 & 0 \\ 0 & a^{-2} & 0 & 0 \\ 0 & 0 & a^{-2} & 0 \\ 0 & 0 & 0 & a^{-2} \end{bmatrix},$$

so the Lagrangian density becomes

$$\mathcal{L} = a^3\left[-\frac{1}{2}\dot{\phi}^2 - \frac{1}{2}m^2\phi^2\right],$$

where terms with $\partial_i\phi$ vanish due the homogeneity of ϕ. To obtain the equation of motion from the Lagrangian density, we apply the Euler-Lagrange equation in field theory

$$0 = \partial_\mu\frac{\partial\mathcal{L}}{\partial(\partial_\mu\psi^*)} - \frac{\partial\mathcal{L}}{\partial\psi^*}$$

Since $\partial_t(a^3\dot{\phi}) = a^3(\ddot{\phi} + 3H\dot{\phi})$, we obtain the equation of motion for a homogeneous axion background

$$\ddot{\phi} + 3H\dot{\phi} + m^2\phi = 0$$

A.2 Non-relativistic scalar field

We adopt the same ALP Lagrangian density and potential in section A, but this time we will consider the perturbed Friedman-Robertson-Walker metric

$$g^{\mu\nu} = \begin{bmatrix} -(1+2\Phi) & 0 & 0 & 0 \\ 0 & a^{-2}(1-2\Phi) & 0 & 0 \\ 0 & 0 & a^{-2}(1-2\Phi) & 0 \\ 0 & 0 & 0 & a^{-2}(1-2\Phi) \end{bmatrix},$$

where Φ is the Newtonian gravitational potential. Note that the above is the inverse of the metric $g_{\mu\nu}$ in $ds^2 = g_{\mu\nu}dx^\mu dx^\nu$. The Lagrangian density becomes

$$\mathcal{L} = a^3 \left[-\frac{1}{2}(1+2\Phi)(\partial_t\phi)^2 + \frac{1}{2a^2}(1-2\Phi)(\partial_i\phi)^2 - \frac{1}{2}m^2\phi^2 \right]$$

In the non-relativistic regime, the scalar field varies slowly and we can factored out the fast oscillation terms. The field can be rewritten in terms of the complex field ψ

$$\phi = \frac{1}{\sqrt{2m}}(\psi \mathrm{e}^{-imt} + \psi^* \mathrm{e}^{imt}).$$

So the squared terms in the Lagrangian density are

$$\begin{aligned} (\partial_t\phi)^2 &= m\psi^*\psi + i(\psi^*\partial_t\psi - \psi\partial_t\psi^*) \\ (\partial_i\phi)^2 &= \frac{\partial_i\psi\partial_i\psi^*}{m} \\ \phi^2 &= \frac{\psi\psi^*}{m} \end{aligned}$$

Note that we work with the lowest order in $\partial\psi$ and ignore the fast oscillation terms with e^{2imt}. The Lagrangian density becomes

$$\begin{aligned} \mathcal{L} = a^3 \Big[& -\frac{1}{2}(1+2\Phi)(m\psi^*\psi + i(\psi^*\partial_t\psi - \psi\partial_t\psi^*)) \\ & + \frac{1}{2a^2}(1-2\Phi)\frac{\partial_i\psi\partial_i\psi^*}{m} \\ & + \frac{1}{2}m\psi\psi^* \Big] \end{aligned}$$

We neglect terms with $\Phi\partial\psi$, and finally we obtain the Schrödinger Lagrangian.

$$\mathcal{L} = a^3 \left[\frac{i}{2}(\psi^*\partial_t\psi - \psi\partial_t\psi^*) - m\Phi\psi^*\psi - \frac{\partial_i\psi\partial_i\psi^*}{2ma^2} \right]$$

A.3 Non-linear regime

Again, we apply the Euler-Lagrange equation in section A to obtain the equation of motion for the FDM model in the non-relativistic limit

$$\frac{i}{a^{3/2}}\partial_t(a^{3/2}\psi) = -\frac{1}{2ma^2}\nabla^2\psi + m\Phi\psi$$

where we know that $a^{-3/2}\partial_t(a^{3/2}\psi) = \partial_t\psi + \frac{3}{2}\frac{\dot{a}}{a}\psi$. The equation is rewritten in comoving quantities

$$\psi_{\rm c} = a^{3/2}\psi \qquad \nabla_{\rm c} = a\nabla \qquad \Phi_{\rm c} = a\Phi$$

and we obtain the Schrödinger equation

$$i\partial_t\psi_{\rm c} = -\frac{1}{2ma^2}\nabla_{\rm c}^2\psi_{\rm c} + \frac{m}{a}\Phi_{\rm c}\psi_{\rm c},$$

where the gravitational potential follows the Poisson equation

$$\nabla_{\rm c}^2\Phi_{\rm c} = 4\pi Gm(|\psi_{\rm c}| - <\psi_{\rm c}>)$$

A.4 Madelung equations - the quantum hydrodynamic equations

Instead of describing the dynamics of the FDM with the Schrödinger-Poisson equation, we can apply the Madelung transformation to obtain a set of quantum hydrodynamic equations which resemble the Euler equation and continuity equation. We start with defining the wave fucntion with fluid quantities

$$\psi = \sqrt{n}{\rm e}^{i\theta},$$

where n is number density and θ is the phase. We apply it to the Schrödinger equation while we recover the constant $\hbar$ and assume $a = 1$ in this derivation

$$i\hbar\partial_t(\sqrt{n}{\rm e}^{i\theta}) = -\frac{\hbar}{2m}\nabla^2(\sqrt{n}{\rm e}^{i\theta}) + m\Phi(\sqrt{n}{\rm e}^{i\theta}).$$

We remind that $\nabla^2(fg) = f\nabla^2 g + 2\nabla f\cdot\nabla g + g\nabla^2 f$ and $\nabla^2({\rm e}^{i\theta}) = {\rm e}^{i\theta}(i\nabla^2\theta - (\nabla\theta)^2)$. We expand the equation above and separate it into real and imaginary component

$$\partial_t\sqrt{n} = \frac{\hbar}{2m}(2\nabla\sqrt{n}\cdot\nabla\theta + \sqrt{n}\nabla^2\theta)$$
$$\partial_t\theta = \frac{\hbar}{2m}\left[\frac{\nabla^2\sqrt{n}}{\sqrt{n}} - (\nabla\theta)^2\right] - \frac{m}{\hbar}\Phi$$

Now the trick is to multiply $\sqrt{n}$ to the first equation on both sides, and apply ∇ to the second equation on both sides. After some calculation, we then obtain the the Madelung equations

$$\partial_t n + \frac{\hbar}{m}\nabla\cdot(n\boldsymbol{v}) = 0$$
$$\partial_t\boldsymbol{v} + (\boldsymbol{v}\cdot\boldsymbol{\nabla})\boldsymbol{v} = \frac{\hbar^2}{2m^2}\nabla\left(\frac{\nabla^2\sqrt{n}}{\sqrt{n}}\right) - \nabla\Phi.$$

A.5 The scaling symmetry

Based on Mocz et al. (2018), they claim that Schrödinger-Poisson system has the following scaling symmetry

$$\{x, t, \rho, m\} \to \{\alpha x, \beta t, \beta^{-2}\rho, \alpha^{-2}\beta m\}$$

Since the wave function $\psi \propto \sqrt{\rho/m}$, it also has a symmetry

$$\{\psi\} \to \{\alpha\beta^{-3/2}\psi\}$$

From the Poisson equation $\nabla^2\Phi \propto \rho$, we can obtain a symmetry for the gravitational potential

$$\{\Phi\} \to \{\alpha^2\beta^{-2}\Phi\}$$

Now if we plug in all the scaling symmetry into the Schrödinger equation, we obtain

$$\alpha\beta^{5/2}\frac{\partial\psi}{\partial t} = \alpha\beta^{5/2}\frac{\nabla^2\psi}{m} - \alpha\beta^{5/2}m\psi\Phi$$

where the constants cancel each other. We remind that there are typos regarding the scaling symmetry in Mocz et al. (2017) and Chan et al. (2022).

A.6 The virial theorem

We start with defining the moment of inertia $I = \frac{m}{2}\int d\mathbf{r}r^2|\psi|^2$, where density is $\rho = |\psi|^2$. Alternatively, we can also define it with inner product $\langle A, B\rangle = \int A^* B d\mathbf{r}$, where $*$ denotes as complex conjugate

$$I = \frac{m}{2}d\mathbf{r}\left\langle\psi, r^2\psi\right\rangle \tag{A.1}$$

The idea is to perform a second-time derivative on the moment of inertia $\ddot{I}$, and set it to zero due to equilibrium. We remind that the Schrödinger equation tells that $i\hbar\partial_t\psi = H\psi$, and the conjugate version is $i\hbar\partial_t\psi^* = -H\psi^*$, where H is the Hamiltonian $H = \hbar^2/2m\nabla^2 - m\Phi$ So the first derivative of the moment of inertia is as follow:

$$\begin{aligned}\dot{I} &= \frac{m}{2}\left(\left\langle\frac{\partial\psi}{\partial t}, r^2\psi\right\rangle + \left\langle\psi, r^2\frac{\partial\psi}{\partial t}\right\rangle\right)\\ &= -\frac{im}{2\hbar}\left(\left\langle\psi, r^2H\psi\right\rangle - \left\langle\psi, Hr^2\psi\right\rangle\right)\end{aligned}$$

We applied the Schrödinger equation and the self-adjointness of the Hamiltonian, meaning $\langle HA, B\rangle = \langle A, HB\rangle$. Now if we define commutator as $[A, B] = AB - BA$, we have

$$\dot{I} = -\frac{im}{2\hbar}\left\langle\psi, [r^2, H]\psi\right\rangle \tag{A.2}$$

same as Hui et al. (2017). Similarly, if we apply time derivative again, we have

$$\ddot{I} = -\frac{m}{2\hbar^2}\left\langle\psi, [[r^2, H], H]\psi\right\rangle \tag{A.3}$$

By calculating the commutator, and converting ψ into the fluid quantity $\psi = \sqrt{\rho/m}\ \mathrm{e}^{i\theta}$ and $v \equiv \hbar\boldsymbol{\nabla}\theta/m$, we have

$$\ddot{I} = -\int \rho\mathbf{r}\cdot\boldsymbol{\nabla}\Phi\ d\mathbf{r} + 2\int \frac{\rho v^2}{2} d\mathbf{r} + 2\int \frac{\hbar^2}{2m^2}|\boldsymbol{\nabla}\sqrt{\rho}|^2 d\mathbf{r}, \tag{A.4}$$

where the first, second and third integral term are the gravitational energy W, kinectic energy K and quantum energy Q respectively. At the state of equilibrium, we have $\ddot{I} = 0 = W + 2K + 2Q$, but note that since $K > 0$ we have the following virial theorem

$$\frac{Q}{|W|} \leq \frac{1}{2}$$

A virialized system in FDM model must satisfy the virial theorem.

Appendix B

Additional numerical details

B.1 Shooting a soliton

Here we solve for a numerical solution to the soliton profile. Assuming spherical symmetry, we can simply expand the derivatives in Eq.2.24 to obtain a 4^{th} order differential equation. Then, we adopt dimensionless quantities

$$X = r\frac{2GMm^2 n_o^{1/4}}{\hbar^2} \qquad f = \rho\frac{\pi\hbar^6}{2G^3M^4m^6n_o}$$

we will obtain the following 4^{th} order differential equation

$$f'''' = 2f^2 - \left(\frac{4}{X}f''' - \frac{10f'f''}{fX} + \frac{6f'^3}{f^2X} - \frac{3f'''f'}{f} - \frac{2f''^2}{f} + \frac{7f'^2f''}{f^2} - \frac{3f'^4}{f^3}\right),$$

where $'$ is $\partial/\partial X$ To numerically solve it, we apply the shooting method. We start with an initial condition and advance until X is large enough to see f goes to 0. We need 4 initial conditions to yield physical density profile, meaning density is finite at center, and 0 at infinity.

$$f(0) = 1, \qquad f'(0) = f'''(0) = 0, \qquad f''(0) = A$$

Based on Chavanis & Delfini (2011), we must adopt $A = -0.612386937160$. For simplicity, we discretize the spatial step with Euler methods. Then, we separate the 4^{th} order differential equation into a set of 4 first order equation

$$f_i' = \frac{f_{i+1} - f_i}{\Delta X}$$
$$f_i'' = \frac{f_{i+1}' - f_i'}{\Delta X}$$
$$f_i''' = \frac{f_{i+1}'' - f_i''}{\Delta X}$$

$$\frac{f''_{i+1} - f''_i}{\Delta X} = 2f_i^2 - \left[\frac{4}{X_i} f'''_i - \frac{10 f'_i f''_i}{f_i X_i} + \frac{6 f'^3_i}{f_i^2 X_i} - \frac{3 f'''_i f'_i}{f_i} - \frac{2 f''^2_i}{f_i} + \frac{7 f'^2_i f''_i}{f_i^2} - \frac{3 f'^4_i}{f_i^3}\right]$$

We start with $i = 0$ and advance to solve for $(f_{i+1}, f'_{i+1}, f''_{i+1}, f'''_{i+1})$ until the desired steps N. We have tested a few numbers of N (Figure below). Most profiles are the same in the inner part, but we observed that larger N will give a profile that extends to larger X before blowing up to infinite density. As it clearly shows, soliton has a cored profile. We made the above numerical algorithm publicly available, and in addition, we included a version with 4^{th} order Runge-Kutta method [1].

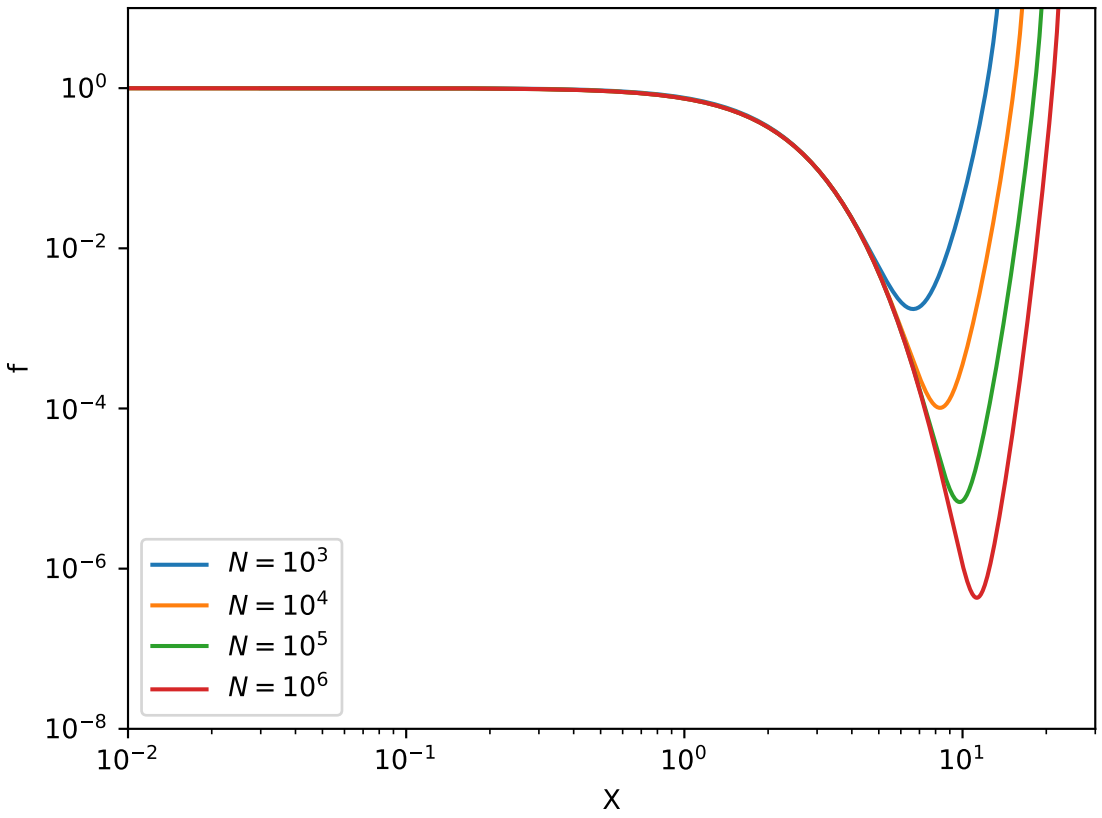

Fig. B.1. Numerical soliton solution in different spatial resolution N. f and X axis are normalized density and radius defined in text. As the resolution increases, we can resolve to larger radius.

B.2 Alternative Schrödinger solver

There exists a huge amount of literature discussing the numerical method for solving the linear Schödinger equation. Here we describe three of them, and why there are not suitable

[1] https://github.com/jchan192/ShootingSoliton

for our numerical simulation. Let's define here the equation without constants

$$\frac{\partial \psi}{\partial t} = \nabla^2 \psi - \Phi \psi$$

The simplest case is to apply the Euler method for the time derivative

$$\frac{\psi_i^{n+1} - \psi_i^n}{\Delta t} = D^2 \psi^n - \Phi_i^n \psi_i^n,$$

where D^2 is the any prefered spatial discretization. For example, a 2^{nd} order center difference would mean $D^2\psi = (\psi_{i+1}^n - 2\psi_i^n + \psi_{i-1}^n)/\Delta x$. Unfortunately, the method is only 1^{st} order accurate both in time, and more importantly, it does not conserve the norm $|\psi|$. We can improve the temporal accuracy by using a higher order method. For example, Schwabe et al. (2016) adopted the 4^{th} order Runge-Kutta method to evolve the Schrödinger step. However, we must remind that the method is explicit, so the timestep is heavily limited by the CFL condition, and Runge-Kutta does not converse with the norm in principle.

A mass and energy conserving Schrödinger solver is the **Crank-Nicolson method**. It is also an implicit method, thus, it is less constrained by the CFL method.

$$\frac{\psi_i^{n+1} - \psi_i^n}{\Delta t} = \frac{D^2\psi^{n+1} + D^2\psi^n}{2} - \frac{\Phi_i^{n+1}\psi_i^{n+1} + \Phi_i^n \psi_i^n}{2}$$

One well-known disadvantage of any implicit method is its expensive computational cost: each time step requires more time to solve than explicit methods. For instance, if we adopt the Crank-Nicolson method to solve the Schrödinger equation, we are solving a system of linear equations expressed in matrix form $A\mathbf{x} = \mathbf{b}$, where A is a matrix depending on the spatial discretization, $\mathbf{b}$ is obtained from ψ^n and we solve the linear system for $\mathbf{x}$, which is ψ^{n+1}. In 1D, A is a tridiagonal matrix so the linear system can be solved by the **Thomas algorithm**. However, the situation becomes complicated in 2D and 3D, so in general, we will solve the linear system with the relaxation method.

The last method we discuss is the split-step method with exponential integrator, which is the adopted method in this work. The Schrödinger equation can be expressed as $\partial_t \psi = H\psi$, where $H = -\nabla^2 + \Phi$ is the Hamiltonian operator. We can solve it exactly by exponential integrator

$$\psi^{n+1} = e^{H\Delta t}\psi^{n+1}.$$

Solving the above will give exact solution, which is not possible if we have both the laplace operator and potential. Thus, the main question is what $\mathrm{e}^{H\Delta t}$ means numerically. A naive approach is to approximate it as

$$\psi^{n+1} \approx e^{-\nabla^2 \Delta t} e^{\Phi \Delta t} \psi^{n+1}$$

This is called the **Lie-Trotter splitting**, which is only first order accurate. The second order method is called **Strang splitting**

$$\psi^{n+1} \approx e^{\Phi \Delta t/2} e^{-\nabla^2 \Delta} e^{\Phi \Delta t/2} \psi^{n+1}$$

Besides the advantage of the second order temporal accuracy, the method is also 1) symplectic, similar to the leap-frog method adopted in N-body simulation, 2) unitary so it preserves

norm, and 3) also can be combined with the spectral method for spatial discretization. This method is explicit, so the timestep must be constrained by CFL-like condition $\Delta t \propto \Delta x^2$. If the spatial discretization is uniform, the spectral method is superior to all other described methods because of its spectral accuracy in spatial resolution. We remind that the Strang splitting spectral method, or in short, the pseudo-spectral method, is the adopted numerical scheme of this work.

B.3 Cosmological initial condition: from particle to wave

From *MUSIC*, we obtain an initial phase space (x, y, z, v_x, v_y, v_z) of the particles, and we will need to convert them into an initial wave function ψ for the FDM solver. We remind that the fluid quantity $(\rho, \mathbf{v})$ is related to the amplitude and phase of the wave function through Eq.2.16 and 2.17. The amplitude can be obtained cloud-in-cloud algorithm, which is the standard practice to assign particles to grid density. The phase is slightly more different. We need to first apply the divergence on the velocity relation in Eq.2.17 to obtain

$$\frac{am}{\hbar}(\boldsymbol{\nabla} \cdot \mathbf{v}) = \nabla^2 \theta$$

Note that this is simply a Poisson equation. We apply the cloud-in-cloud algorithm as well to the velocity (v_x, v_y, v_z) at each grid. So the left hand side is known, and we can finally obtain the phase at each grid by performing Fourier transform and its inverse, which is the spectral solver for the Poisson equation. We now have an initial wave function $\psi = \sqrt{\rho/m}e^{i\theta}$ We note that different code may have different units. For example, the velocity in Gadget format .

Above describes the mathematical method of converting the information from particle to wave. Numerically, we are discretizing the wave function into uniform grids, so we need to apply the cloud-in-cell interpolation to assign each particle quantity to their corresponding neighbouring cells. In 3D, each particle should have eight neighbouring cells. Assuming each N-body particle has a mass of $m_{\rm p}$, the equations of the cloud-in-cell interpolation for all eight cells are

$$\begin{aligned}
\rho_{i,j,k} &= \rho_{i,j,k} + m_{\rm p} t_x t_y t_z & \rho_{i+1,j,k} &= \rho_{i+1,j,k} + m_{\rm p} d_x t_y t_z \\
\rho_{i,j+1,k} &= \rho_{i,j+1,k} + m_{\rm p} t_x d_y t_z & \rho_{i+1,j+1,k} &= \rho_{i+1,j+1,k} + m_{\rm p} d_x d_y t_z \\
\rho_{i,j,k+1} &= \rho_{i,j,k+1} + m_{\rm p} t_x t_y d_z & \rho_{i+1,j,k+1} &= \rho_{i+1,j,k+1} + m_{\rm p} d_x t_y d_z \\
\rho_{i,j+1,k+1} &= \rho_{i,j+1,k+1} + m_{\rm p} t_x d_y d_z & \rho_{i+1,j+1,k+1} &= \rho_{i+1,j+1,k+1} + m_{\rm p} d_x d_y d_z
\end{aligned}$$

where we define

$$d_a = x_a - c_a \qquad t_a = 1 - d_a.$$

a is a subscript for $\{x, y, z\}$, c_a is the center of the box, and x_a is the position of the particle. Although this only shows the case for density, similar method is also applied for the velocity in x, y and z directions.

B.4 FFT based Poisson Solver

In this work, we faced the Laplace operator at least three times: the Schrödinger equation $\partial_t \psi = \nabla^2 \psi$, the velocity-phase relation in Appendix B.3, and finally the Poisson equation $\nabla^2 \Phi = 4\pi G \rho$. Here we demonstrate how we can use Fourier transform to handle the Laplace operator, and, for example, solve the Poisson equation. We remind that, however, Fourier transform requires the grid to be uniformly spaced, so the method does not apply to adaptive meshes. After applying Fourier transform to the Poisson equation, we obtain

$$\mathcal{F}[\Phi] = -\frac{4\pi G \mathcal{F}[\rho]}{k^2},$$

where $\mathcal{F}$ refers to Fourier transform. In 3D, the wavenumber is $k^2 = k_{\rm x}^2 + k_{\rm y}^2 + k_{\rm z}^2$. The gravitational potential Φ can be obtained by performing a backward Fourier transform on both sides. In short, the solver can be expressed as

$$\Phi = \mathcal{F}^{-1}\left[-\frac{4\pi G \mathcal{F}[\rho]}{k^2}\right]$$

In practice, the Fourier transform can be easily performed by the publicly available Fast Fourier Transform (FFT) library[2]. The wavevector in each dimension follows the Nyquist frequency. We note that the algorithm will fail when $k = 0$, so we need to force the algorithm to assign $\Phi = 0$ when $k = 0$. In fact, this procedure means the gravitational potential has a zero mean. To test the Poisson solver, we suggest the following test equation

$$\rho(x, y, z) = -\sin(x)\sin(y)\sin(z)$$

In periodic boundary condition, we will expect $\Phi = \rho$ for dimensionless form.

[2] fftw.org

Bibliography

Bernal T., Fernández-Hernández L. M., Matos T., Rodríguez-Meza M. A., 2018, MNRAS, 475, 1447

Boldrini P., 2021, Galaxies, 10, 5

Borukhovetskaya A., Navarro J. F., Errani R., Fattahi A., 2022, MNRAS, 512, 5247

Bovy J., Tremaine S., 2012, ApJ, 756, 89

Boylan-Kolchin M., Bullock J. S., Kaplinghat M., 2012, MNRAS, 422, 1203

Brandt S., Dahmen H. D., Taylor E. F., 1986, American Journal of Physics, 54, 1153

Bryan G. L., Norman M. L., 1998, ApJ, 495, 80

Bullock J. S., Boylan-Kolchin M., 2017, Annu. Rev. Astron. Astrophys., 55, 343

Burkert A., 2020, ApJ, 904, 161

Calabrese E., Spergel D. N., 2016, MNRAS, 460, 4397

Carr B., Kühnel F., 2020, Annual Review of Nuclear and Particle Science, 70, 355

Chambers K. C., et al., 2016, arXiv e-prints, p. arXiv:1612.05560

Chan H. Y. J., Ferreira E. G. M., May S., Hayashi K., Chiba M., 2022, MNRAS, 511, 943

Chavanis P.-H., 2019, Physics Review D, 100, 083022

Chavanis P.-H., Delfini L., 2011, Physics Review D, 84, 043532

Chen S.-R., Schive H.-Y., Chiueh T., 2017, Mon. Not. Roy. Astron. Soc., 468, 1338

Chiang B. T., Schive H.-Y., Chiueh T., 2021, Physics Review D, 103, 103019

Clowe D., Bradač M., Gonzalez A. H., Markevitch M., Randall S. W., Jones C., Zaritsky D., 2006, ApJL, 648, L109

Dalal N., Kravtsov A., 2022, arXiv e-prints, p. arXiv:2203.05750

Dalal N., Bovy J., Hui L., Li X., 2021, , 2021, 076

Dark Energy Survey Collaboration et al., 2016, MNRAS, 460, 1270

Di Luzio L., Giannotti M., Nardi E., Visinelli L., 2020, , 870, 1

Di Paolo C., Salucci P., Erkurt A., 2019, MNRAS, 490, 5451

Du X., Behrens C., Niemeyer J. C., Schwabe B., 2017, Phys. Rev. D, 95, 043519

Eisenstein D. J., Hu W., 1998, ApJ, 496, 605

Eisenstein D. J., Hu W., 1999, ApJ, 511, 5

Errani R., Navarro J. F., Ibata R., Peñarrubia J., 2022, MNRAS, 511, 6001

Ferreira E. G. M., 2020, Ultra-Light Dark Matter (arXiv:2005.03254)

González-Morales A. X., Marsh D. J. E., Peñarrubia J., Ureña López L. A., 2017, Mon. Not. Roy. Astron. Soc., 472, 1346

Guzmán F. S., Ureña-López L. A., 2006, ApJ, 645, 814

Hahn O., Abel T., 2011, MNRAS, 415, 2101

Hayashi K., Chiba M., Ishiyama T., 2020, ApJ, 904, 45

Hayashi K., Ferreira E. G. M., Chan H. Y. J., 2021, ApJL, 912, L3

Hlozek R., Grin D., Marsh D. J. E., Ferreira P. G., 2015, Physics Review D, 91, 103512

Homma D., et al., 2019, , 71, 94

Hopkins P. F., 2019, MNRAS, 489, 2367

Hui L., 2021, Wave Dark Matter (arXiv:2101.11735)

Hui L., Ostriker J. P., Tremaine S., Witten E., 2017, Phys. Rev. D, 95, 043541

Hwang J.-C., Noh H., 2009, Physics Letters B, 680, 1

Iršič V., Viel M., Haehnelt M. G., Bolton J. S., Becker G. D., 2017, , 119, 031302

Ishiyama T., et al., 2021, MNRAS, 506, 4210

Jowett Chan H. Y., Chiba M., Ishiyama T., 2019, arXiv e-prints, p. arXiv:1910.02197

Kawai H., Oguri M., Amruth A., Broadhurst T., Lim J., 2022, ApJ, 925, 61

Kelley T., Bullock J. S., Garrison-Kimmel S., Boylan-Kolchin M., Pawlowski M. S., Graus A. S., 2019, MNRAS, 487, 4409

Kirby E. N., Bullock J. S., Boylan-Kolchin M., Kaplinghat M., Cohen J. G., 2014, MNRAS, 439, 1015

Klypin A., Kravtsov A. V., Valenzuela O., Prada F., 1999, ApJ, 522, 82

Kulkarni M., Ostriker J. P., 2022, MNRAS, 510, 1425

Levkov D. G., Panin A. G., Tkachev I. I., 2018, , 121, 151301

Marsh D. J. E., Niemeyer J. C., 2019, , 123, 051103

Martin G., et al., 2019, MNRAS, 485, 796

May S., Springel V., 2021, MNRAS, 506, 2603

Mina M., Mota D. F., Winther H. A., 2020, Solitons in the dark: non-linear structure formation with fuzzy dark matter (`arXiv:2007.04119`)

Mocz P., Vogelsberger M., Robles V. H., Zavala J., Boylan-Kolchin M., Fialkov A., Hernquist L., 2017, MNRAS, 471, 4559

Mocz P., Lancaster L., Fialkov A., Becerra F., Chavanis P.-H., 2018, Physics Review D, 97, 083519

Moore B., Ghigna S., Governato F., Lake G., Quinn T., Stadel J., Tozzi P., 1999, ApJL, 524, L19

Nadler E. O., et al., 2021, , 126, 091101

Navarro J. F., Frenk C. S., White S. D. M., 1996, ApJ, 462, 563

Newton O., Cautun M., Jenkins A., Frenk C. S., Helly J. C., 2018, MNRAS, 479, 2853

Nori M., Baldi M., 2021, MNRAS, 501, 1539

Nori M., Murgia R., Iršič V., Baldi M., Viel M., 2019, MNRAS, 482, 3227

Oh S.-H., et al., 2015, Astron. J., 149, 180

Oman K. A., et al., 2015, MNRAS, 452, 3650

Paduroiu S., 2022, Universe, 8, 76

Persic M., Salucci P., Stel F., 1996, MNRAS, 281, 27

Planck Collaboration et al., 2020, , 641, A6

Robles V. H., Bullock J. S., Boylan-Kolchin M., 2019, MNRAS, 483, 289

Rogers K. K., Peiris H. V., 2021, Phys. Rev. Lett., 126, 071302

Roszkowski L., Sessolo E. M., Trojanowski S., 2018, Reports on Progress in Physics, 81, 066201

Safarzadeh M., Spergel D. N., 2020, ApJ, 893, 21

Salucci P., Lapi A., Tonini C., Gentile G., Yegorova I., Klein U., 2007, MNRAS, 378, 41

Sawala T., et al., 2016, MNRAS, 457, 1931

Schive H.-Y., Chiueh T., Broadhurst T., 2014a, Nature Phys., 10, 496

Schive H.-Y., Liao M.-H., Woo T.-P., Wong S.-K., Chiueh T., Broadhurst T., Hwang W. Y. P., 2014b, , 113, 261302

Schive H.-Y., Chiueh T., Broadhurst T., Huang K.-W., 2016, ApJ, 818, 89

Schwabe B., Niemeyer J. C., 2022, , 128, 181301

Schwabe B., Niemeyer J. C., Engels J. F., 2016, Physics Review D, 94, 043513

Schwarzschild M., 1979, ApJ, 232, 236

Tegmark M., et al., 2004, Physics Review D, 69

Tollerud E. J., Bullock J. S., Strigari L. E., Willman B., 2008, ApJ, 688, 277

Tollet E., et al., 2016, MNRAS, 456, 3542

Villanueva-Domingo P., Mena O., Palomares-Ruiz S., 2021, Frontiers in Astronomy and Space Sciences, 8, 87

Vogelsberger M., Marinacci F., Torrey P., Puchwein E., 2020, Nature Reviews Physics, 2, 42

Walker M. G., Peñarrubia J., 2011, ApJ, 742, 20

Yavetz T. D., Li X., Hui L., 2021, Construction of Wave Dark Matter Halos: Numerical Algorithm and Analytical Constraints (`arXiv:2109.06125`)

York D. G., et al., 2000, , 120, 1579

van Dijk W., Brown J., Spyksma K., 2011, , 84, 056703

van den Bosch F. C., 2017, MNRAS, 468, 885